FEDERAL UNIVERSITY OF ESPÍRITO SANTO
TECHNOLOGICAL CENTER
POSTGRADUATE PROGRAM IN ELECTRICAL ENGINEERING

HIGOR ARAÚJO FIM CAMPOREZ

DOCTORAL THESIS

AI-BASED STRATEGIES FOR HANDOVER ENHANCEMENT IN VISIBLE LIGHT COMMUNICATION SYSTEMS

VITÓRIA
MARCH 2025

FEDERAL UNIVERSITY OF ESPÍRITO SANTO
TECHNOLOGICAL CENTER
POSTGRADUATE PROGRAM IN ELECTRICAL ENGINEERING

Author:
HIGOR ARAÚJO FIM CAMPOREZ

Advisors:
PROF. DR. HELDER R. O. ROCHA
PROF. DR. JAIR A. LIMA SILVA
PROF. DR. HEINRICH WÖRTCHE

AI-BASED STRATEGIES FOR HANDOVER ENHANCEMENT IN VISIBLE LIGHT COMMUNICATION SYSTEMS

Doctoral Thesis submitted to the Graduate Program in Electrical Engineering from the Technological Center of the Federal University of Espírito Santo, as a requirement for the degree of Doctor in Electrical Engineering.

VITÓRIA
MARCH 2025

Ficha catalográfica disponibilizada pelo Sistema Integrado de Bibliotecas - SIBI/UFES e elaborada pelo autor

---

Camporez, Higor Araújo Fim, 1993-
C198a AI-based strategies for handover enhancement in visible light communication systems / Higor Araújo Fim Camporez. - 2025.
139 p. : il.

Orientador: Helder Roberto de Oliveira Rocha.
Coorientadores: Jair Adriano Lima Silva, Heinrich Wortche.
Tese (Doutorado em Engenharia Elétrica) - Universidade Federal do Espírito Santo, Centro Tecnológico.

1. Artificial intelligence. 2. Meta-heuristics. 3. Handover optimization. 4. Visible light communication. I. Rocha, Helder Roberto de Oliveira. II. Silva, Jair Adriano Lima. III. Wortche, Heinrich. IV. Universidade Federal do Espírito Santo. Centro Tecnológico. V. Título.

CDU: 621.3

Approval Sheet

March 21, 2025.

This doctoral thesis entitled "*AI-Based Strategies for Handover Enhancement in Visible Light Communication Systems*", prepared and submitted by Higor Araújo Fim Camporez in partial fulfillment of the requirements for the degree of Doctor in Electrical Engineering at the Federal University of Espírito Santo (UFES), has been examined and is recommended for acceptance and approval for Oral Defense.

gov.br Documento assinado digitalmente
HELDER ROBERTO DE OLIVEIRA ROCHA
Data: 11/06/2025 18:31:56-0300
Verifique em https://validar.iti.gov.br

Prof. Dr. Helder Roberto de Oliveira Rocha (Advisor)
Federal University of Espírito Santo - UFES

gov.br Documento assinado digitalmente
JAIR ADRIANO LIMA SILVA
Data: 18/06/2025 19:31:08-0300
Verifique em https://validar.iti.gov.br

Prof. Dr. Jair Adriano Lima Silva (Co-advisor)
Federal University of Espírito Santo - UFES

Dr. -Ing. Heinrich Wörtche (Co-advisor)
Hanze University of Applied Sciences

Approved by the following Committee on Oral Examination.

gov.br Documento assinado digitalmente
ALEXANDRE DE ALMEIDA PRADO POHL
Data: 16/06/2025 15:02:35-0300
Verifique em https://validar.iti.gov.br

Prof. Dr. Alexandre de Almeida Prado Pohl (External Researcher)
Federal University of Technology – Paraná - UTFPR

gov.br Documento assinado digitalmente
TIAGO ZANOTELLI
Data: 16/06/2025 19:40:04-0300
Verifique em https://validar.iti.gov.br

Prof. Dr. Tiago Zanotelli (External Researcher)
Federal Institute of Espírito Santo - IFES

Documento assinado digitalmente
gov.br
MARIA JOSE PONTES
Data: 17/06/2025 21:37:51-0300
Verifique em https://validar.iti.gov.br

Prof. Dr. Maria José Pontes (Internal Researcher)
Federal University of Espírito Santo - UFES

Documento assinado digitalmente
gov.br
PATRICK MARQUES CIARELLI
Data: 16/06/2025 15:45:26-0300
Verifique em https://validar.iti.gov.br

Prof. Dr. Patrick Marques Ciarelli (Internal Researcher)
Federal University of Espírito Santo - UFES

Abstract

The Internet of Things (IoT) growth, particularly applications involving wireless devices, has significantly increased the demand for signal bandwidth. However, Radio Frequency (RF) wireless systems presented a limited spectrum to support massive device connections and susceptibility to electromagnetic interference. These challenges have increased the interest in exploring alternative solutions to face RF issues while maintaining high data rates, low latency, reliability, and cost efficiency. Advancements in Light Emitting Diode (LED) technology have introduced highly energy-efficient lighting capable of high-speed modulation of light intensity. Thus, these characteristics have driven research into Visible Light Communication (VLC), which can utilize existing lighting infrastructures for data transmission using a broad and unregulated optical spectrum (≈ 400 THz). Additionally, VLC can also provide physical layer security, low power consumption, high transmission speeds, and immunity to RF electromagnetic interference.

Spectral efficiency and high data rates are critical for VLC systems, with Orthogonal Frequency Division Multiplexing (OFDM) emerging as a robust and spectrally efficient modulation technique for indoor applications. However, nonlinearities introduced by multicarrier signals in LED-based systems can degrade performance. To address these issues, techniques such as Constant-Envelope OFDM (CE-OFDM) have been developed to mitigate Peak-to-Average Power Ratio (PAPR), improving power efficiency and reducing distortions, particularly in high-power transmission scenarios. Additionally, VLC faces several challenges, including signal blockage by opaque objects, confinement of signals, and limited Access Point (AP) coverage. Addressing these limitations often requires deploying ultra-dense networks to ensure reliable connectivity across large areas. However, such dense deployments can lead to frequent handovers, increasing infrastructure costs and complexity.

This thesis evaluates the application of larger signal amplitudes despite the LED-nonlinearities to enable data transmission over long distances, evaluating the conventional and constant-envelope OFDM performances. Furthermore, it proposes a Modified Genetic Algorithm (MGA) optimization procedure combined with time series Machine Learning (ML) classifiers to minimize handovers in both a digital twin-based simulation system and experimental VLC setups. The proposed handover scheme considers receiver trajectory information to reduce handover frequency while maintaining system performance within the forward error correction limit.

Results demonstrate that a 9.51 Mb/s CE-OFDM system with 16-QAM subcarrier mapping in a 5MHz bandwidth outperformed a conventional OFDM system in terms of efficiency. The application of the CE-OFDM scheme in a 6m VLC link reduced the EVM from 17.5%

to 10%, an improvement of approximately 43%. Additionally, the CE-OFDM-based VLC system demonstrated satisfactory performance in an 8 m link when using 4-QAM subcarrier mapping. The proposed handover scheme outperforms a power-based approach, achieving handover reductions of 42.47% in a MISO simulation environment and up to 48.61% in a MIMO environment. In experimental scenarios with three and four transmitters, the scheme achieved reductions of 46.43% and 45.45%, respectively. These results confirm that the integration of MGA with ML models effectively minimizes handovers and improves overall VLC system performance.

***Keywords*:** Artificial intelligence, Meta-heuristics, Handover optimization, and Visible light communication.

Resumo

O crescimento da Internet das Coisas (IoT), particularmente em aplicações envolvendo conexões sem fio, aumentou significativamente a demanda por largura de banda. No entanto, os sistemas sem fio baseados em radiofrequência (RF) apresentam um espectro limitado para suportar conexões massivas de dispositivos, além de serem suscetíveis a interferências eletromagnéticas. Esses desafios têm aumentado o interesse em explorar soluções alternativas para lidar com as limitações da RF, ao mesmo tempo em que mantêm-se altas taxas de dados, baixa latência, confiabilidade e eficiência de custos. Os avanços tecnológicos dos diodos emissores de luz (LED) introduziram sistemas de iluminação altamente eficientes em termos de energia e com capacidade de modular a intensidade luminosa em alta velocidade. Assim sendo, essas características têm impulsionado a pesquisa em comunicação via luz visível (VLC), que pode aproveitar infraestruturas de iluminação existentes para transmissão de dados, utilizando um espectro óptico amplo e não regulamentado ($\approx$ 400 THz). Além disso, o VLC também pode oferecer segurança na camada física, baixo consumo de energia, altas taxas de transmissão e imunidade a interferências eletromagnéticas de RF.

A eficiência espectral e altas taxas de dados são aspectos críticos para sistemas de VLC. Assim, o OFDM tem se mostrado como uma técnica de modulação robusta e espectralmente eficiente para aplicações em ambientes internos. No entanto, as não linearidades introduzidas por sinais multiportadoras em sistemas baseados em LED podem degradar o desempenho. Para enfrentar tais problemas, técnicas como o CE-OFDM foram desenvolvidas para mitigar o PAPR, melhorando a eficiência energética e reduzindo distorções, especialmente em cenários de transmissão com alta potência. Além disso, o VLC enfrenta diversos desafios, incluindo o bloqueio de sinais por objetos opacos, o confinamento dos sinais e a cobertura limitada dos pontos de acesso (AP). Para contornar essas limitações geralmente exige-se a implantação de redes ultradensas para garantir conectividade confiável em grandes áreas. No entanto, essas implantações densas podem resultar em transferências frequentes, aumentando os custos de infraestrutura e a complexidade do sistema.

Esta tese avalia a aplicação de sinais com alta potência, visando avaliar as não linearidades dos LEDs, para viabilizar a transmissão de dados em longas distâncias, analisando o desempenho do OFDM convencional e de envoltória constante. Além disso, propõe-se um procedimento de otimização baseado em um algoritmo genético modificado (MGA) combinado com classificadores de séries temporais baseados em aprendizado de máquina (ML) para minimizar o número total de transferências, tanto em um sistema de simulação baseado em gêmeos digitais quanto em configurações experimentais de VLC. O esquema de transferência proposto consid-

era informações da trajetória do receptor para reduzir o número de transferências, mantendo o desempenho do sistema dentro do limite de correção de erros (FEC).

Os resultados demonstram que um sistema de CE-OFDM operando a $9,51$ Mb/s com mapeamento de subportadoras em 16-QAM e largura de banda de 5 MHz superou um sistema convencional de OFDM em termos de eficiência. A aplicação do CE-OFDM em um enlace de VLC de 6 m reduziu o EVM de $17,5\%$ para 10%, uma melhoria de aproximadamente 43%. Além disso, o sistema de VLC baseado em CE-OFDM demonstrou um desempenho satisfatório em um enlace de 8 m ao utilizar mapeamento de subportadoras em 4-QAM. O esquema de transferência proposto superou a abordagem padrão baseada em potência, alcançando reduções de $42,47\%$ em um ambiente de simulação MISO e de até $48,61\%$ em um ambiente MIMO. Em cenários experimentais com três e quatro transmissores, o esquema alcançou reduções de $46,43\%$ e $45,45\%$, respectivamente. Esses resultados confirmam que a integração de MGA com modelos de ML minimiza efetivamente as transferências e, por conseguinte, o desempenho geral do sistema de VLC.

***Palavras-Chave*:** Inteligência Artificial, Metaheuristicas, Otimização, handover, Comunicação via luz visível.

Acknowledgments

This thesis became a reality thanks to the invaluable assistance and generous support of many individuals. As the saying goes, ”None of us is as strong as all of us together,” and I am deeply grateful to each and every one of you for your contributions to this collective achievement.

First and foremost, I thank God for guiding my efforts and not allowing me to give up along this arduous journey, granting me the strength to face and overcome many challenges. I am deeply grateful to my parents, Iramaia Inês Araújo and José Reinaldo Fim Camporez, for their dedication to my education and their unwavering support throughout this journey. Especially, I extend my heartfelt thanks to my girlfriend, Yasmim Sagrillo Pimassoni, for all her help, support, patience, understanding, shared moments, and so much more.

I would like to express my appreciation and deepest thanks to my advisors, Prof. Dr. Helder Rocha, Prof. Dr. Jair Silva, and Prof. Dr. Heinrich Wörtche, for allowing me to pursue this PhD degree. I am thankful for their guidance, both within and beyond the realm of research, their direction, patience, and all the valuable lessons learned. I would also like to express my heartfelt gratitude to Prof. Dr. Leandro Costalonga for his invaluable teachings and for introducing me to the world of research and development, which have profoundly shaped my journey.

I am grateful to all my colleagues from the Telecommunications Laboratory (LabTel) for their help in times of need, for the moments of relaxation, for the joyful coffee breaks and lunches, and for everything else.

This study was financed in part by the Coordenação de Aperfeiçoamento de Pessoal de Nível Superior – Brasil (CAPES) – Finance Code 001 and the project CAPES-PRINT-88881.311735/2018-01. Also, this thesis was financed by the Foundation for Support to Research and Innovation of Espírito Santo (FAPES) with FAPES-2022-BWBR2, FAPES-2023-LMK95, FAPES-84343540, and FAPES 891/2023-P:2023-BDKK7 projects. Additionally, this work was supported by the National Council for Scientific and Technological Development (CNPq) with the project CNPq 309490/2021-9 and by the Research Centre Biobased Economy from the Hanze University of Applied Sciences.

"happiness, only real when shared"

CHRISTOPHER MCCANDLESS

Contents

List of Figures

List of Tables

List of Algorithms

List of Abbreviations and Acronyms

M-**QAM**	M-ary quadrature amplitude modulation
TTT	Time to Trigger
2D	2-dimensional
ACO	Asymmetrically Clipped Optical
ACO-OFDM	Asymmetrically Clipped Optical OFDM
ADC	Analog-to-Digital Converter
AFG	Arbitrary Function Generator
AI	Artificial Intelligence
ANN	Artificial Neural Network
AP	Access Points
ARC	Arc-tangent
AWGN	Additive White Gaussian Noise
B2B	Back-to-back
BER	Bit Error Rate
CCE	Categorical Cross-Entropy
CDF	Cumulative Distribution Function
CE-OFDM	Constant-Envelope OFDM
CNN	Convolutional Neural Networks
CoB	Chip-on-board
CP	Cyclic Prefix
DAB	Digital Audio Broadcasting
dB	Decibel
DCO-OFDM	Direct Current Optical OFDM
DFT	Discrete Fourier Transform
DFT-S	Discrete Fourier Transform Spread
DLS	Digital Subscriber Lines
DT	Digital Twin
DVB	Digital Video Broadcasting
EVM	Error Vector Magnitude
FBS	Filter Bank Spread
FDM	Frequency Division Multiplexing

FEC	Forward Error Correction
FFT	Fast Fourier Transform
Flip-OFDM	Flipped OFDM
FOV	Field of View
GA	Genetic Algorithm
GaN	Gallium Nitride
HetNet	Heterogeneous Network
HHO	Horizontal Handover
HS	Hermitian Symmetry
ICI	Interchannel Interference
IDFT	Inverse Discrete Fourier Transform
IFFT	Inverse Fast Fourier Transform
IIoT	Industrial Internet of Things
IM/DD	Intensity Modulation and Direct Detection
IoT	Internet of Things
ISI	Intersymbol Interference
LACO-OFDM	Layered ACO-OFDM
LD	Laser Diode
LED	Light Emitting Diode
LiFi	Light Fidelity
LOS	Line-of-sight
LSTM	Long Short-Term Memory
LTE	Long-Term Evolution
MDO	Mixed Domain Oscilloscope
MGA	Modified Genetic Algorithm
MGAD	MGA data
MIMO	Multiple Input Multiple Output
MISO	Multiple Input Single Output
ML	Machine Learning
NR	New Radio
NSGA	Non-Sorting Genetic Algorithm
OFDM	Orthogonal Frequency Division Multiplexing
OTS	Off-the-shelf
OWC	Optical Wireless Communications
P95	95th Percentile
PAPR	Peak-to-Average Power Ratio
PD	Photodiode

PLC	Power Line Communication
QPSK	Quadrature Phase-Shift Keying
RAM	Random Access Memory
RF	Radio Frequency
RL	Reinforcement Learning
RMS	Root Mean Square
RMSE	Root Mean Squared Error
RNN	Recurrent Neural Networks
SE	Spectral Efficiency
SISO	Single Input Single Output
SNR	Signal-to-noise Ratio
STD	Standard Handover Scheme
TCN	Temporal Convolutional Networks
TIA	Transimpedance Amplifier
VHO	Vertical Handover
VLC	Visible Light Communication
WiFi	Wireless Fidelity
WS	Workstations

List of Symbols and Notations

Signal

Δf	OFDM subcarrier spacing
$\hat{s(t)}$	Received signal after FFT block
$\hat{s}_i$	Received signal after FFT block for the i-th subcarrier
A	Unitary signal amplitude
B_{N}	Bandwidth of a subcarrier
B_{w}	Bandwidth of the OFDM modulating signal
F_{s}	Sampling rate
f_c	Carrier central frequency
f_i	Carrier frequency of the i-th subcarrier
g_{rx}	Filter at the receiver
g_{tx}	Filter at the transmitter
h	Phase modulation index
$h(t)$	Channel impulsive response
L	Hermitian symmetry output size
N	Number of samples in a symbol
N_{symb}	Number of symbols to evaluate the EVM metric
N_{FTT}	FFT size
N_{s}	Number of subcarriers
P_s	Average power
$r(t)$	Received signal in continuous time domain
$r[n]$	Received signal in discrete time domain
R_{b}	Bitstream rate
R_{N}	Bitstream rate of a OFDM subchannel
$s(t)$	Signal in continuous time domain
$s[n]$	Signal in discrete time domain
s_i	Complex output after the mapper block for the i-th subcarrier
T_{g}	Guard interval
T_{N}	OFDM symbol duration
$x(t)$	Modulating signal

Machine Learning

α_{p}	Penalty factor

δ_{HOM}	Handover power margin
μ	Mutation rate
φ	Activation function
b_k	Bias
FF	Fitness function
N_{HO}	Total number of handovers
P_{host}	Power of the host AP
P_{target}	Power of the target AP
TTT	Time to trigger
w_k	Neuron weight
x_m	Neuron input
y_k	Neuron output

Visible Light Communications

α	Linear amplification factor
η	LED luminous efficiency
OMI	Optical modulation index
ϕ	Angle of irradiance
$\Phi_{1/2}$	Transmitter semi-power angle
ψ	Angle of incidence
Ψ_{c}	receiver's field of view
ζ	Adjustment constant
A_{p}	Photodetection area of the luxmeter
A_r	Area of the receiver photodetector
d	Distance between a receiver and a transmitter
$g(\psi)$	Optical gain of an ideal non-imaging concentrator
H_{los}	Line-of-sight channel gain
I_{bias}	LED bias current
I_{in}	LED input current
I_{max}	LED maximum bias current
k	Saturation intensity factor
L_{max}	LED maximum output illuminance
L_{out}	LED output illuminance
n	Refractive index
P_{opt}	Transmitter optical power
$P_{\mathrm{r-los}}$	received optical power

R	Photodetector responsivity
R	Photodiode responsivity
$T_{\mathrm{s}}(\psi)$	Gain of the optical filter
w	Photodetection noise

CHAPTER 1.
Introduction

1.1. Introduction and Motivation

The adoption of Light Emitting Diode (LED) technology for illumination has revolutionized the lighting industry, offering significant advantages over traditional lighting solutions by reducing overall energy consumption and operating costs. Furthermore, LEDs have a longer lifespan compared to incandescent and fluorescent lamps. The U.S. Department of Energy reported that approximately 48% of all installed lighting units were LED-based in 2020 [3]. The global LED lighting market was valued at $\$81.64$ billion in 2023 and is projected to reach $\$191.80$ billion by 2032 [4].

The Industrial Internet of Things (IIoT) growth has led to a shift from wired to wireless connectivity, specifically in applications using mobile machines and robots [5, 6]. However, the large number of devices and the need for wide bandwidths pose a challenge to traditional Radio Frequency (RF) systems due to the limited RF spectrum and susceptibility to electromagnetic interference in industrial scenarios [7]. Optical Wireless Communications (OWC) such as Visible Light Communication (VLC) has emerged as a potential solution offering a large unlicensed spectrum and resistance to electromagnetic interference [8–10]. VLC can reuse LEDs from the lighting structure for data transmission with wavelengths around 400-700 nm [11, 12]. Additionally, industries require highly secure connections as cyber-attacks can disrupt production and cause accidents [13]. Therefore, VLC can also contribute to security as the light stays confined, and intentional outside interferences can easily be blocked by physical separators [14].

Spectral efficiency and, for certain applications, high data rates are extremely important for VLC systems [15]. Promising results for indoor VLC systems have been demonstrated with Orthogonal Frequency Division Multiplexing (OFDM), a spectrally efficient modulation scheme that is robust to channel frequency selectivity [16–19]. However, an important issue to be considered in LED-based VLC systems is the nonlinearities introduced by the large fluctuation of such multicarrier signals [20, 21]. These nonlinearities distort the output optical signal and limit the transmitted optical power, degrading the system's performance. To address these issues, different techniques were developed to reduce the Peak-to-Average Power Ratio (PAPR) [22–24]. One promising approach to mitigate PAPR in OFDM-based systems is the use of Constant-Envelope OFDM (CE-OFDM). This technique reduces the amplitude variations of the transmitted signal, ensuring a more constant optical output and decreasing the nonlinear distortions.

By maintaining a constant envelope, CE-OFDM enhances the power efficiency and overall performance of VLC systems, particularly in high-power transmission scenarios [25–27].

Although VLC signals are confined to specific areas, which enhances network security, they can be obstructed by opaque objects, leading to performance degradation or complete signal loss. Furthermore, the limited coverage of Access Points (AP) requires the development of ultra-dense networks to cover large areas [28]. Deploying such dense networks can result in frequent handovers, during which a receiver may experience a temporary loss of connection during a hard handover, as it disconnects from one AP before establishing a connection with another. In contrast, soft handover allows the receiver to maintain a continuous connection by establishing the new connection before disconnecting from the current AP [29]. Although soft handover prevents connection loss, it incurs higher costs for the network infrastructure. Consequently, the use of optimization algorithms to minimize handovers in such networks has become an area of significant interest.

The current deployment of VLC systems focuses on mobility, particularly in the context of handover management. In [30], a power-based handover scheme is presented to skip unnecessary handovers. A handover strategy considering frequency diversity and link aggregation was proposed in [31] for indoor vehicular VLC systems. Additionally, the authors of [32] introduced a soft handover-aware scheduling approach, where time slots are scheduled based on users' location. In [33], a power-based soft handover technique was demonstrated in a simulator with two APs. Using received signal strength to choose the signal source, the strategy achieved satisfactory performance across the evaluated trajectories.

When the handover occurs between VLC cells, it is referred to as Horizontal Handover (HHO). The handover concept extends to hybrid networks such as VLC combined with Wireless Fidelity (WiFi) [34, 35], which is denominated as Vertical Handover (VHO). In [34], a VHO scheme applied to an VLC-WiFi network was investigated where the problem was modeled as a Markov decision process, adopting a dynamic approach to obtain a trade-off between the switching cost and the delay requirements. This VHO scheme improved the signaling cost by 50%. Additionally, [36] presents an upper-layer hybrid VLC-WiFi handover approach, where experiments show that outage durations were minimized to 0.03 and 0.06 seconds for HHO and VHO, respectively.

Artificial Intelligence (AI) techniques, including meta-heuristic optimizations and Machine Learning (ML), have demonstrated considerable potential for enhancing communication, VLC, and IIoT systems [37–39]. The authors of [40] applied Non-Sorting Genetic Algorithm (NSGA)-II to optimize guard band and signal bandwidth, aiming to enhance the spectral efficiency of an OFDM-based fiber communication system. A similar optimization approach was explored in [26], focusing on CE-OFDM signals. In [41], a multi-objective optimization using NSGA-II was presented to maximize transmitted power and spectral efficiency for both CE-OFDM and OFDM VLC systems. As ML and deep learning can contribute to VLC systems, [42]

demonstrated an application of Convolutional Neural Networks (CNN) as a demodulator for non-orthogonal multiple access in a VLC system, which compensates for both linear and non-linear distortions. In [43], CNN was also applied for channel estimation and equalization in an OFDM-based VLC system. Furthermore, [44] and [45] proposed a hybrid multi-objective optimization approach, combining the grey wolf optimizer and NSGA-III to optimize VLC system parameters, with the goal of maximizing both power and spectral efficiency. The authors also trained a Long Short-Term Memory (LSTM) network using the optimized parameters to predict the optimal parameters for future positions, based on the receiver's previous and current positions.

1.2. Research Questions, Hypotheses, and Objectives

As VLC continues to evolve, new modulation schemes and system optimization play a crucial role in extending link distance and enhancing performance. Additionally, the increasing deployment of VLC leads to dense networks designed to improve redundancy and coverage, which can cause frequent handovers. AI models can mitigate this issue by optimizing handover management and reducing the overall number of handovers while maintaining seamless connectivity.

1.2.1. Research Questions

This thesis seeks to answer the following research questions (RQs).

RQ.1 - How can CE-OFDM increase the reach of VLC Links compared with conventional OFDM?

RQ.2 - How can communication signal amplitude and bias current impact the performance of VLC systems?

RQ.3 - How can AI minimize handovers in Multiple Input Single Output (MISO) VLC systems based on the receiver's trajectory and positioning?

RQ.4 - How can AI minimize handovers in Multiple Input Multiple Output (MIMO) VLC systems based on the receivers' trajectory and positioning?

1.2.2. Hypotheses

To respond to the above-itemized questions, the following hypotheses (Hs) were investigated.

H.1 - By setting CE-OFDM as the modulation scheme of a VLC system, it is possible to increase the reach of the communication link compared with conventional OFDM.

H.2 - The bias current does not impact system performance if it is set at a level that prevents the communication signal from driving the LED into a non-linear or cutoff region.

H.3 - Considering a MISO VLC system, AI models can predict the following endpoint of a receiver based on its trajectory and positioning to minimize handovers while maintaining Error Vector Magnitude (EVM) performance under the Forward Error Correction (FEC) limit.

H.4 - AI models can simultaneously predict the following endpoint of multiple receivers based on their trajectory and positioning, optimizing handover efficiency and ensuring EVM performances within the FEC threshold.

1.2.3. Research Objectives

This thesis aims to investigate handover minimization in VLC systems. Furthermore, this thesis also explores how to increase the reach of VLC link lengths by applying constant-envelope OFDM. To address these challenges, this work introduces artificial intelligence techniques, specifically meta-heuristics and neural networks. Achieving the main objective required the following specific goals:

- perform conventional OFDM and constant-envelope OFDM modulation techniques to compare their performance over extended VLC links;
- analyze the impact of communication signal level and bias current in VLC systems;
- develop MISO and Single Input Single Output (SISO) VLC models according to real experimental setups;
- employ meta-heuristic optimization algorithms to minimize the total number of handovers across a given trajectory;
- apply neural networks, such as long short-term memory, to predict the receiver's following endpoint.

1.3. Contributions

This thesis's developments rely on the improvements of VLC systems through the application of artificial intelligence algorithms and modulation schemes parametrization. The main contributions include the application of Genetic Algorithm (GA) and ML algorithms to minimize the number of handovers in MIMO and MISO VLC simulation systems, showing experimental results for MISO scenarios. Furthermore, this thesis investigates the enhancement of traditional VLC communication link range using CE-OFDM when compared to OFDM. Additionally, this thesis examines the influence of bias current and the modulating signal amplitude on the performance of both SISO and MISO VLC systems.

1.4. Publications

Two articles addressing the research questions were published to academic journals throughout this doctoral research period, while two additional papers were published in conference proceedings. The journal articles are listed below.

J.1 - **Camporez, H.**, Costa, W., Pontes, M., Segatto, M., Rocha, H., Silva, J., Hinrichs, M., Paraskevopoulos, A., Jungnickel, V., and Freund, R. "Increasing the reach of visible light communication links through constant-envelope OFDM signals". *Optics Communications*, v. 530, p. 129179, 2023.

J.2 - **Camporez, H.**, Costa, W., Segatto, M., Silva, J., Deters, J. K., Wörtche, H., and Rocha, H. "Ai-driven enhancements for handover in visible light communication systems". *Journal of Lightwave Technology*, v. 42, pp. 8191-8202, 2024

The published conference papers are the following.

C.1 - **H. Camporez**, W. Costa, J. Silva, H. Rocha, and M. Segatto. "Performance Evaluation of a Soft Handover Framework Applied to VLC Systems." In *2021 SBMO/IEEE MTT-S International Microwave and Optoelectronics Conference* (IMOC), pp. 1-3. IEEE, 2021.

C.2 - **H. Camporez**, Y. Pimassoni, W. Costa, M. Segatto, J. Silva and H. Rocha, "Remote Control in Smartphone-based Visible Light Communications," *2021 Third South American Colloquium on Visible Light Communications (SACVLC)*, Toledo, Brazil, 2021, pp. 1-6.

The following publications were produced concurrently during the doctoral program and related to the research field.

1 - Silva, J., Pizzaia, J., Costa, W., **Camporez, H.**, Pontes, M., Rocha, H., and Segatto, M. "Performance evaluation of a simplified power-domain NOMA for visible light communications". *JOSA A*, v. 40, p. C46-C52, 2023.

2 - Costa, W., **Camporez, H.**, Pontes, M., Segatto, M., Rocha, Silva J., Hinrichs, M., Paraskevopoulos, A., Jungnickel, V., and Freund, R. "Increasing the Power and Spectral Efficiencies of OFDM-based VLC System through Multi-objective Optimization," *Journal of the Optical Society of America. A, Optics, Image Science, And Vision*, v. 40, p. 1268-1275, 2023.

3 - Peterle, A., Costa, W., **Camporez, H.**, Segatto, M., Rocha, H., and Silva, J. A. "Comparing the Performance of OFDM and OCDM-based Visible Light Communications: Numerical and Experimental Analysis". *Journal of Microwaves, Optoelectronics, and Electromagnetic Applications*, v. 22, p. 196-207, 2023.

4 - W. Costa, W. Santos, **H. Camporez**, M. Faber, J. Silva, M. Segatto, H. Rocha. "Planning and Resources Allocation of a Hybrid IoT Network using Artificial Intelligence," *Internet of Things*. v. 26, pp. 101225, 2024.

5 - W. Costa, **H. Camporez**, M. Segatto, H. Rocha, and J. Silva. "Towards AI-enhanced VLC

Systems." In *Optical Fiber Communication Conference*, pp. W3I-7. Optica Publishing Group, 2022.

6 - W. Costa, **H. Camporez**, M. Pontes, M. Segatto, H. Rocha, J. Silva, M. Hinrichs, A. Paraskevopoulos, V. Jungnickel, and R. Freund. "Increasing the LED Bias Point of an OFDM-based VLC System through Multi-objective Optimization." In *2021 SBMO/IEEE MTT-S International Microwave and Optoelectronics Conference (IMOC)*, pp. 1-3. IEEE, 2021.

7 - Costa, W., **Camporez, H.**, Hinrichs, M., Rocha, H., Pontes, M., Segatto, M., Rocha H., Silva J., Hinrichs, M., Paraskevopoulos, A., Jungnickel, V., and Freund, R. Toward AI-enhanced VLC Systems for Industrial Applications. *Journal of Lightwave Technology. (Invited Paper).*, v. 41, p. 1064 - 1076, 2022.

1.5. Thesis Outline

This thesis is divided into seven chapters. Chapter 1 introduces the essential aspects of the research, including motivations, objectives, and an outline of the thesis. Chapter 2 provides a theoretical background on topics relevant to this study, such as VLC, OFDM modulation schemes, artificial intelligence, and metaheuristics algorithms. Chapter 3 describes the application of CE-OFDM in a SISO VLC system to increase the reach of communication links. Chapter 4 investigates the influence of bias current and the modulating signal amplitude on VLC systems, as well as the accuracy of the numerical models. Chapter 5 discusses the application of ML models and GA to minimize handovers based on receiver data in a MISO experimental and simulation environment. Chapter 6 explores the use of ML models and GA to minimize handovers based on receivers' information in a MIMO VLC simulation environment. Finally, the conclusions and future directions are presented and discussed in Chapter 7. Figure 1.1 illustrates the relationship between the research questions and the chapters of this thesis.

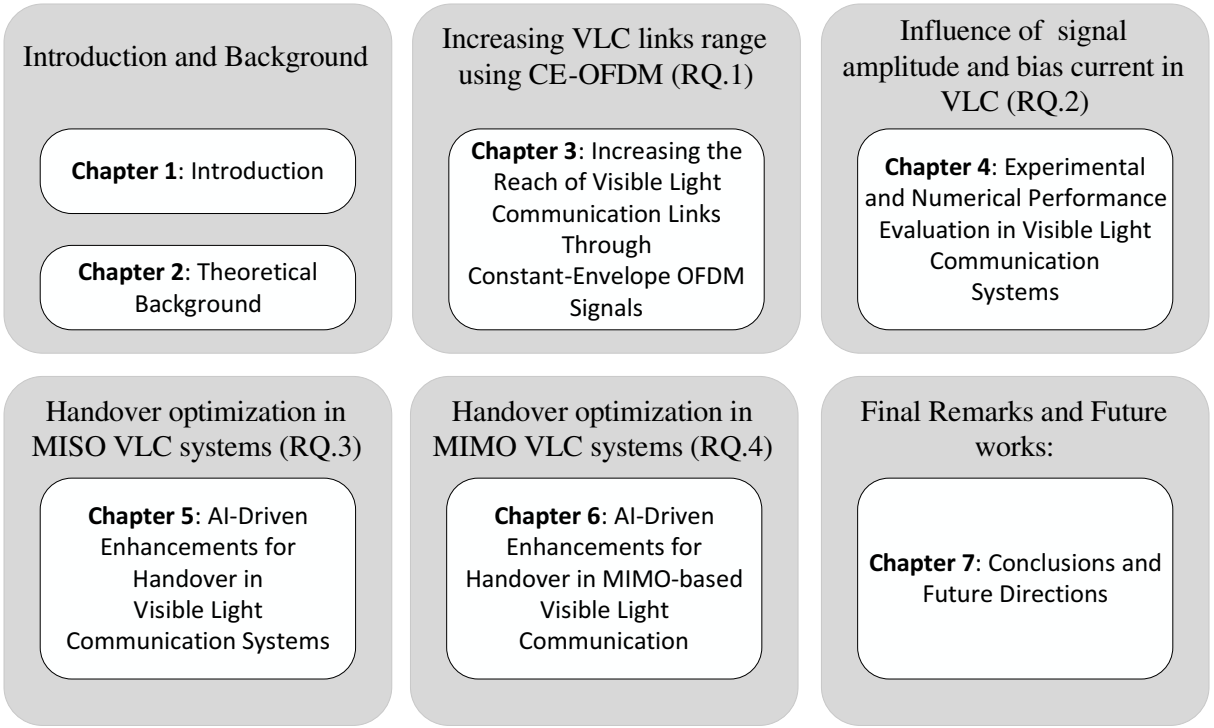

Figure 1.1. Diagram illustrating the relationship between the thesis's organization and the research questions.

CHAPTER 2.
Theoretical Background

This Chapter outlines the foundational concepts that support this research, including the modeling of VLC systems, the application of OFDM modulation in VLC, optimization through metaheuristic techniques, and machine learning approaches.

2.1. Visible Light Communications Systems

VLC stands as one of the oldest methods of human communication. Since ancient times, light has played a crucial role in communication. Early examples include fire signals used for communication between tribes and reflected sunlight for signaling between ships, a technique employed by the ancient Greeks. For long-distance communication, fire beacons were often positioned on elevated points and lit sequentially to transmit messages across vast distances [46]. VLC was proposed in a more advanced technological way in the 1880s by Alexander Graham Bell when he developed the photophone, which modulated sunlight with vibration caused by speech and transmitted the modulated light to a receiver [47]. However, significant progress in VLC began in 1927, when Russian scientist Oleg Losev discovered electroluminescence and developed the LED [46].

Following the early innovations, VLC technology has continued to progress due to its inherent resistance to electromagnetic interference. In addition, modern LEDs now support fast-switching capabilities, enabling higher data rates for communication. Recent experimental demonstrations have achieved data rates up to 46.4 Gbps [48, 49]. As interest in VLC grows, new applications are emerging, including use cases in education [50], vehicular communication [51, 52], medical environments [53, 54], industrial settings [45, 55], Internet of Things (IoT) [56,57], highly secure (military) applications [58,59], underwater communication [60,61], and others. Furthermore, in high-security applications, the confined nature of light provides an extra layer of security, as VLC signals cannot penetrate walls as in WiFi.

Figure 2.1 illustrates the electromagnetic spectrum. The visible light portion of the spectrum offers an extensive unlicensed bandwidth of approximately 400 THz, which is about $10,000$ times the bandwidth available for RF. The wavelength range that is visible to the human eye is between 380 nm and 780 nm.

VLC systems commonly use the Intensity Modulation and Direct Detection (IM/DD) method, in which analog signals are modulated directly onto the visible light intensity emitted by the

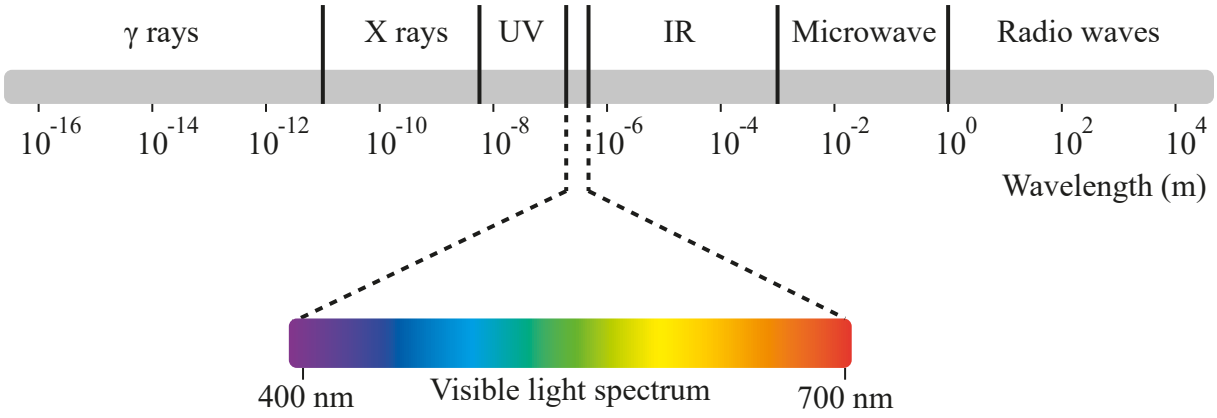

Figure 2.1. Wavelength of the electromagnetic spectrum.

source [62]. Within this IM/DD structure, an analog modulator converts the data bit stream into an analog waveform. This modulated signal is then superimposed into a driver circuit that powers the light source, such as a LED emitting photons based on the electrical input. At the receiving part, a photodetector captures the photons and reconverts them into an electrical signal, which is subsequently amplified and filtered by a Transimpedance Amplifier (TIA) [63]. Finally, the data bit stream is retrieved by the demodulation stage. This VLC IM/DD system architecture is illustrated in Figure 2.2.

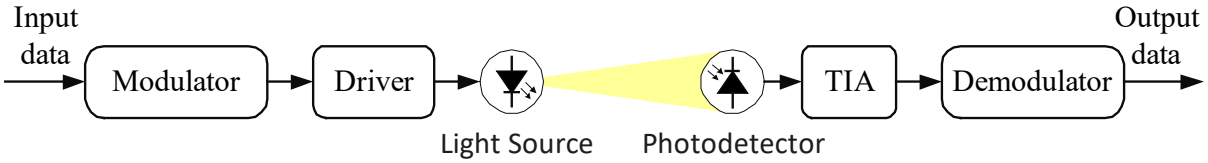

Figure 2.2. VLC intensity modulation and direct detection.

2.1.1. Analytical Modeling

In VLC systems, data signals are transmitted by modulating the intensity of LEDs. However, when the magnitude of the modulating signal drives the LED into its non-linear operating region, significant signal degradation can occur, particularly in systems using OFDM [64]. The electrical-optical conversion of an LED can be represented mathematically as follows

$$L_{\text{out}}(t) = \frac{I_{\text{in}}(t)}{\left[\zeta + \left(\frac{I_{\text{in}}(t)}{L_{\max}}\right)^{2k}\right]^{\frac{1}{2k}}}, \tag{2.1}$$

where L_{out} is the LED output illuminance, $L_{\max}$ is the maximum illuminance of the LED, ζ is an adjustment constant, k is a knee factor that adjusts the saturation intensity, and $I_{\text{in}}(t)$ is LED input current [65]. The $I_{\text{in}}(t)$ is the modulating signal ($s(t)$) superimposed onto a bias current (I_{bias}) in order to create a non-negative driving current. Thus, the LED input current is expressed

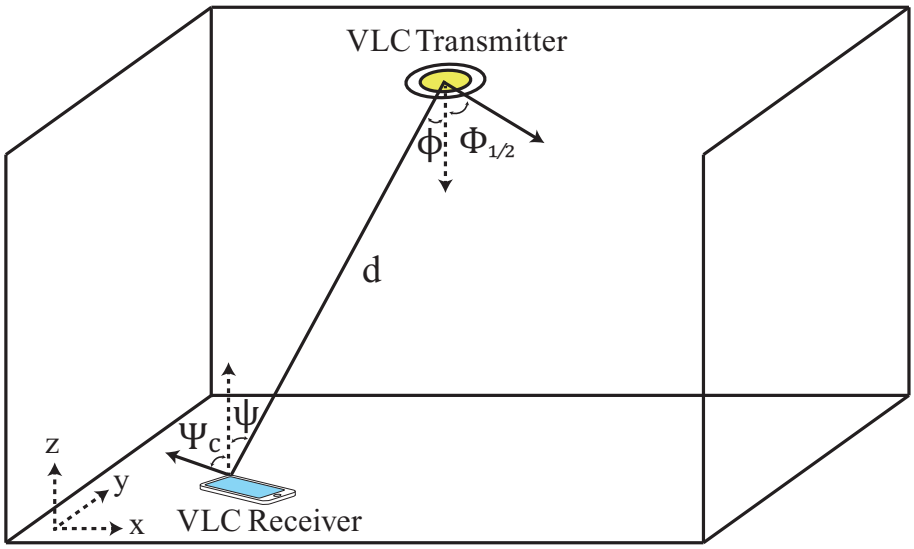

Figure 2.3. Geometry of the VLC LOS channel model.

by $I_{\text{in}}(t) = I_{\text{bias}} + \alpha \times s(t)$, where α is the amplification factor. The relationship between the maximum LED current (I_{max}) and the I_{bias}, that leads to the LED operational region, is known as the optical modulation index (OMI). The OMI is commonly defined as

$$\text{OMI} = \frac{I_{\text{max}} - I_{\text{bias}}}{I_{\text{bias}}} = \frac{\alpha \cdot \max(|s(t)|)}{I_{\text{bias}}}. \tag{2.2}$$

The transmitter optical power can be calculated as $P_{\text{opt}}(t) = [L_{\text{out}}(t) \times A_{\text{p}}]/\eta$, where η is the LED luminous efficiency and A_{p} is the photodetection area of the sensor used to measure the photometric unit [66]. For the purpose of this thesis, we have adopted the Line-of-sight (LOS) channel model described in [67]. According to this model, the DC gain of a VLC link (see Figure 2.3) can be expressed as:

$$H_{\text{los}} = \begin{cases} \frac{(m+1)A_{\text{r}}}{2\pi d^2} \cos^m(\phi) T_{\text{s}}(\psi) g(\psi) \cos(\psi), & 0 \leq \psi \leq \Psi_{\text{c}} \\ 0, & \text{elsewhere} \end{cases} \tag{2.3}$$

where d represents the distance between the transmitter and the receiver, ϕ is the angle of irradiance, ψ is the angle of incidence, Ψ_{c} is the receiver's Field of View (FOV), $T_{\text{s}}(\psi)$ is the gain of the optical filter, A_r is the area of the photodetector, $m = -\ln(2)/\ln(\cos(\Phi_{1/2}))$ where $\Phi_{1/2}$ is the transmitter semi-power angle, and $g(\psi)$ is the optical gain of an ideal non-imaging concentrator having an internal refractive index (n), which is defined as

$$g(\psi) = \begin{cases} \frac{n^2}{\sin^2(\Psi_{\text{c}})}, & 0 \leq \psi \leq \Psi_{\text{c}} \\ 0, & \psi > \Psi_{\text{c}} \end{cases} \tag{2.4}$$

The received optical power ($P_{\text{r-los}}$) is calculated as $P_{\text{r-los}}(t) = H_{\text{los}} \times P_{\text{opt}}(t)$ and the Pho-

todiode (PD) optical-electrical conversion is modeled as

$$I_{\mathrm{PD}}(t) = RP_{\mathrm{r-los}}(t) + w(t), \tag{2.5}$$

where R is the photodiode responsivity and $w(t)$ is the overall photodetection noise [68, 69]. The noise is independent of the wavelength and is modeled as an Additive White Gaussian Noise (AWGN) [62].

2.2. Orthogonal Frequency Division Multiplexing

Research on multicarrier systems dates back to the 1950s with the introduction of Frequency Division Multiplexing (FDM) in 1957 [70]. However, the complexity of synchronizing carriers limited its widespread adoption. In 1966, Chang patented the principles of OFDM, outlining the use of orthogonal spectral overlap for multichannel data communication [71]. Following Chang's work, Saltzberg proposed an offset-QAM modulation method in 1967, which reduced signal envelope fluctuation and simplified filter design for both transmission and reception [72].

A significant advancement in OFDM technology came from Weinstein and Ebert in 1971, who suggested using the Discrete Fourier Transform (DFT) for generating and receiving OFDM signals. This approach greatly simplified transceiver design by eliminating the need for numerous analog oscillators [73]. They also introduced guard intervals and raised-cosine windowing to address Intersymbol Interference (ISI) and Interchannel Interference (ICI). In 1980, Peled and Ruiz further improved OFDM by adding a Cyclic Prefix (CP), which enhanced carrier orthogonality and reduced ICI without requiring empty guard intervals [74]. Following this, Hirosaki advanced the field by implementing an OFDM system with DFT, QAM on subcarriers, and an equalization algorithm to mitigate interferences [75, 76].

By the 1990s, OFDM had become a standard in several communication systems, including Digital Audio Broadcasting (DAB), Digital Video Broadcasting (DVB), and Wireless Local Area Networks (WLAN, IEEE 802.11a/g). It also became the standard for Digital Subscriber Lines (DLS) and, more recently, for Power Line Communication (PLC) [77], Long-Term Evolution (LTE) [78], and 5G New Radio [79]. OFDM has proven its applicability to VLC systems due to its resilience to multipath interference, which is essential in indoor environments with high reflectivity [80]. Moreover, by distributing data across multiple subcarriers, OFDM presents spectral efficiency, enhancing data rates [81]. This section will detail the principles of OFDM, the Direct Current Optical OFDM (DCO-OFDM) technique used in this study, and the performance metrics associated with OFDM.

2.2.1. Transmission and Reception

Figure 2.4 (a) illustrates the process of a simplified baseband multicarrier system. In the transmission, the bitstream (R_b bps) is first converted from serial to parallel form into N_s sub-streams (R_N bps), each carrying m bits. Each bit is then mapped to a symbol ($s_i = a_i + jb_i$) according to the modulation index ($M = 2^m$). After the discrete-to-continuous time conversion by $g_\mathrm{tx}(t)$, the generated signal $s_\mathrm{i}(t)$ modulates the subcarrier with frequency f_i. The output signal is given by the following equation:

$$s(t) = \sum_{i=0}^{N_\mathrm{s}-1} s_i(t) \cdot g_\mathrm{tx}(t) e^{j2\pi f_i t}, \tag{2.6}$$

where s_i is the symbol associated to a subcarrier i with central frequency equal to $f_i = f_0 + i(B_\mathrm{N})$ and B_N is the bandwidth of each subcarrier [82].

At the reception depicted in Figure 2.4 (b), the received signal ($r(t)$) is demodulated by $e^{-j2\pi f_i t}$ and filtered by $g_\mathrm{rx}(t)$. After demapping the symbols, a parallel to serial conversion is applied to give the output bitstream. Considering the symbol duration (T_N) and assuming an ideal rectangular filter within the interval $[0, T_\mathrm{N}]$, each symbol at the input of the demapper block is estimated as described by the following equation [83]:

$$\begin{aligned}
\hat{s}_i &= \frac{1}{T_N} \int_0^{T_N} e^{-j2\pi f_i t} \times s_j(t)\,\mathrm{d}t \\
&= \frac{1}{T_N} \int_0^{T_N} e^{-j2\pi f_i t} \times \left(\sum_{j=0}^{N_s-1} s_j \cdot e^{j2\pi f_j t} \right) \mathrm{d}t \\
&= \frac{1}{T_N} \sum_{j=0}^{N_s-1} s_j \int_0^{T_N} e^{-j2\pi f_i t} \times e^{j2\pi f_j t}\,\mathrm{d}t \\
&= \frac{1}{T_N} \sum_{j=0}^{N_s-1} s_j \int_0^{T_N} e^{-j2\pi (f_i - f_j) t}\,\mathrm{d}t \\
&= \frac{1}{T_N} \cdot s_i \int_0^{T_N} 1 \cdot \mathrm{d}t \\
&= \frac{1}{T_N} \cdot s_i \cdot T_N \\
&= s_i
\end{aligned} \tag{2.7}$$

Although robust and efficient, the transmission and reception models require N_s modulators and demodulators, respectively. These requirements make the implementation of a multi-carrier system unfeasible in terms of cost, size, and power consumption. However, these drawbacks can be addressed by applying DFT and Inverse Discrete Fourier Transform (IDFT). To achieve

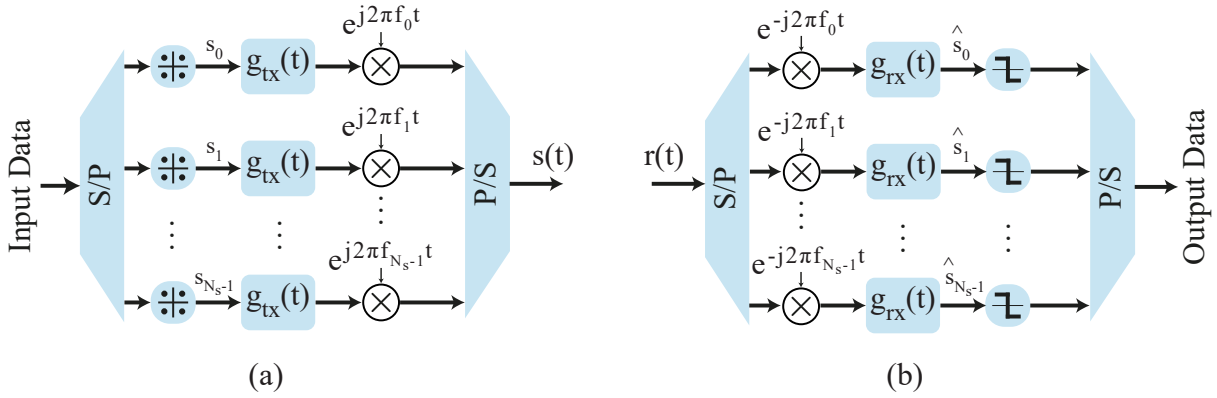

Figure 2.4. Transmission (a) and reception (b) block diagram of a multicarrier system.

this, g_{tx} is applied as a rectangular filter in Equation 2.6 which results in following equation:

$$s(t) = \sum_{i=0}^{N_\text{s}-1} s_i(t) \cdot \text{rect}\left(\frac{t}{T_\text{N}}\right) \cdot e^{j2\pi f_i t}. \tag{2.8}$$

Considering that during the symbol period (T_N), the signal is sampled N times, $t = \frac{nT_N}{N}$ where $(0 < t < T_N)$. Additionally, a subcarrier central frequency can be defined as $f_i = i \cdot \Delta f = \frac{i}{T_N}$, and $\text{rect}\left(\frac{t}{T_N}\right) = 1$ for the ideal case. Therefore, the discrete-time symbol at the transmitter output is given by:

$$s[n] = \sum_{i=0}^{N_\text{s}-1} s_i \cdot e^{j2\pi \frac{i}{T_\text{N}} \frac{nT_\text{N}}{N_\text{s}}} = \sum_{i=0}^{N_\text{s}-1} s_i \cdot e^{j2\pi \frac{n \cdot i}{N_\text{s}}}, \tag{2.9}$$

for $0 \leq n \leq T_N$. It can be observed that Equation 2.9 is the IDFT. Thus, considering the Inverse Fast Fourier Transform (IFFT) that requires less computational resource, it can be written as:

$$s[n] = \text{IFFT}\{s_i\}. \tag{2.10}$$

Some communication systems, such as baseband systems, require real-valued signals at the output of the IDFT. This output type can be achieved by applying Hermitian Symmetry (HS) to the input sequence of the same block [84]. Thus, considering an even N_s and the size of the HS block as $L = 2N_\text{s} + 2$, the input of the HS block is:

$$s_i = \left[0, s_0, s_1, \ldots, s_{N_s-1}, 0, s^*_{N_s}, s^*_{N_s-1}, s^*_{N_s-2}, \ldots, s^*_0\right] \tag{2.11}$$

where s_j* is the complex conjugate of s_j. Therefore, the output of the HS block is given as:

$$s_i = \left[s_0, s_1, \ldots, s_{\frac{L}{2}}, \ldots, s_{L-1}\right] \tag{2.12}$$

where $0 \leq i \leq L-1$ and the subcarriers corresponding to s_0 and $s_{\frac{L}{2}}$ zeroed for convenience.

The new OFDM transmitter diagram, including the HS and IDFT, is illustrated in Figure 2.5 (a). As expected, the IDFT block will produce only real-valued outputs in this configuration. Furthermore, the IDFT output can be expressed as:

$$s[n] = \sum_{i=0}^{N_s-1} \left(a_i^2 + b_i^2\right)^{\frac{1}{2}} \cdot \cos\left[\frac{2\pi ni}{L} + \tan^{-1}\left(\frac{b_i}{a_i}\right)\right] \tag{2.13}$$

where a_i^2 and b_i^2 represent the real and imaginary part of the complex symbol $s_i = a_i^2 + jb_i^2$, respectively.

Analyzing the reception model depicted in Figure 2.4, a signal of a subcarrier can be calculated by:

$$\hat{s}_i(t) = \left[r(t) \cdot e^{-j2\pi f_i t}\right] * g_{rx}(t). \tag{2.14}$$

Considering $f_i = i \cdot \Delta f = \frac{i}{T_N}$ and $g_{rx}(t) = \text{rect}\left(\frac{t}{T_N}\right)$, $\hat{s}_i(t)$ can be expressed as follow

$$\hat{s}_i(t) = \left[r(t) \cdot e^{-j2\pi i \frac{t}{T_N}}\right] * \text{rect}\left(\frac{t}{T_N}\right). \tag{2.15}$$

By applying the integral definition of convolution $g(t) * h(t) = \int_{-\infty}^{+\infty} g(\tau)h(t-\tau)\,d\tau$, we obtain

$$\hat{s}_i(t) = \frac{1}{T_\text{N}} \int_{-\infty}^{+\infty} \left[r(\tau) \cdot e^{-j2\pi i \frac{\tau}{T_\text{N}}}\right] \cdot \text{rect}\left(\frac{t-\tau}{T_\text{N}}\right) d\tau. \tag{2.16}$$

Additionally, considering $t = 0$, the equation is

$$\hat{s}_i(t)|_{t=0} = \frac{1}{T_\text{N}} \int_0^{T_\text{N}} \left[r(\tau) \cdot e^{-j2\pi i \frac{\tau}{T_\text{N}}}\right] d\tau. \tag{2.17}$$

This equation represents a Fourier series as $r(t)$ is sampled at frequencies $f_n = \frac{n}{T_a}$. Equation 2.17 can be rewritten by applying a summation approximation and considering $\tau = nT_a$, and $d\tau = dn \cdot T_a$ [82]. Thus, the equation can be expressed as

$$\hat{s}_i(t)\big|_{t=0} \approx \frac{1}{T_\text{N}} \sum_{n=0}^{N_s-1} r[nT_a] \cdot e^{-j2\pi i \frac{nT_a}{T_\text{N}}}. \tag{2.18}$$

As the sampling period T_a is calculated by $T_a = \frac{T_N}{N_s}$, the received signal $r(t)$ is sampled as $r[i] = r(iT_a)$. This indicates that the received signal is periodic with a period T_N, and each period is sampled at intervals of T_a. Therefore, the Equation 2.18 can rewritten as:

$$\hat{s}[i] = \frac{1}{N_s} \sum_{n=0}^{N_s-1} r[n] \cdot e^{-j2\pi i \frac{n}{N_s}}. \tag{2.19}$$

Finally, the Equation 2.19 is a DFT for $0 \leq i \leq (N_\text{s} - 1)$. Thus, analogous to the transmission

and considering the Fast Fourier Transform (FFT),

$$\hat{s}[n] = \mathrm{FFT}\{r[n]\}. \tag{2.20}$$

The block diagram of this reception model is demonstrated in Figure 2.5 (b). This approach eliminates the need for the N_s oscillators and demodulators, which reduces implementation complexity.

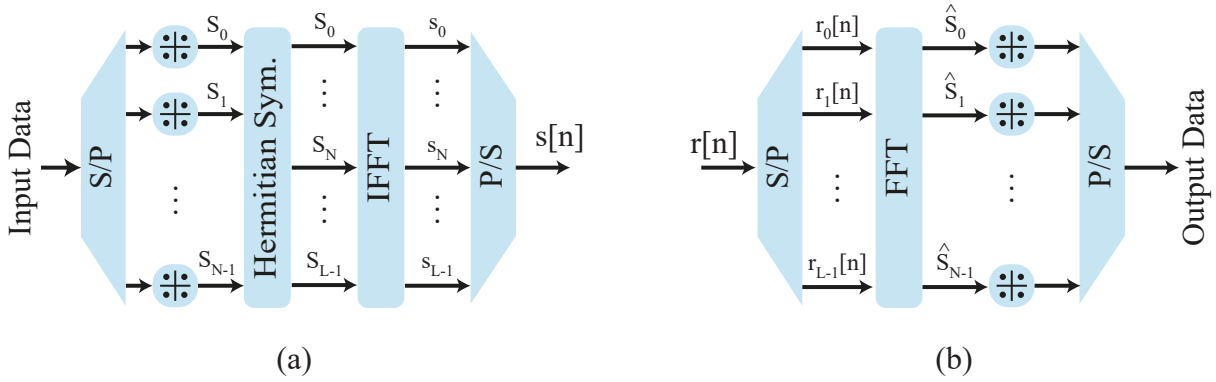

Figure 2.5. Transmission (a) and reception (b) block diagram of an OFDM system.

2.2.2. Multipath Fading and Cyclic Prefix

Channels are characterized by an impulse response $h(t)$ that exhibits a decaying profile. Moreover, channels can be dispersive, where multiple signals reach the receiver through multiple routes due to propagation obstacles. Such channels are known for being frequency-selective and often introduce issues like ISI, as illustrated in Figure 2.6 (a). The overlap between responses of consecutive symbols can disrupt the orthogonality of OFDM signals.

An approach to mitigate this issue is introducing a guard interval T_g, which separates symbols in time, as shown in Figure 2.6 (b). This adjustment increases the total symbol duration to $T = T_\mathrm{N} + T_\mathrm{g}$. OFDM systems are inherently resilient to ISI through the use of a CP. The CP involves copying a time interval T_g from the end of the OFDM symbol and appending it to the beginning of the symbol (see the arrows in Figure 2.6 (b)). This process converts the linear convolution between the channel response and the OFDM symbol into a circular convolution. To ensure proper functioning, the CP duration must exceed the length of the channel's dispersive impulse response [85]. Figure 2.6 (b) also shows that the channel dispersion affects only the CP part of the OFDM symbols.

2.2.3. Direct Current Offset OFDM in VLC Systems

VLC systems require OFDM-modulated signals with real values and non-negative amplitudes to ensure the LED operates outside the cutoff region, which causes clipping. To address

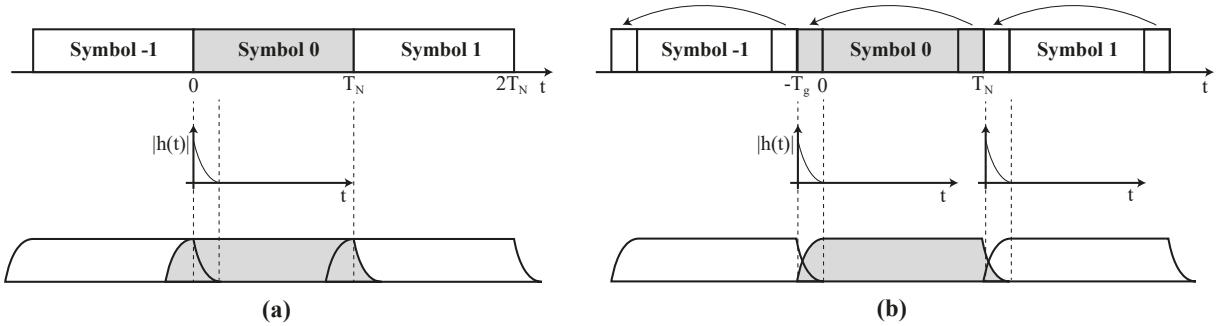

Figure 2.6. Channel effects in OFDM symbol transmission without (a) and with a cyclic prefix.

these constraints, various OFDM schemes have been developed for VLC IM/DD systems, such as DCO-OFDM [86, 87], Asymmetrically Clipped Optical OFDM (ACO-OFDM) [88], Flipped OFDM (Flip-OFDM) [89], and Layered ACO-OFDM (LACO-OFDM) [90], among others. As the focus of this study relies on the DCO-OFDM technique, Figure 2.7 illustrates a block diagram of a typical DCO-OFDM physical layer applied to VLC. In this system, the passband OFDM signal $s(t)$ is amplified by a factor α and biased with a direct current I_{bias} to prevent signal clipping in the cutoff region.

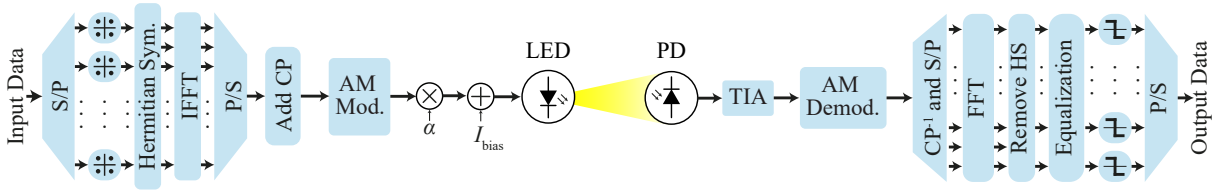

Figure 2.7. DCO-OFDM block diagram applied to a VLC physical layer.

2.2.4. Constant-Envelope OFDM

The CE-OFDM signals of this work are generated by phase modulating an electrical carrier with OFDM waveforms, which results in constant-envelope signals with low PAPR [91]. Thus, beyond the advantages provided by conventional OFDM, this type of constant-envelope signal allows efficient use of transmission powers. In VLC systems, this transformation technique enables high values of LEDs' bias polarization aiming at higher optical output powers and, therefore, higher link distances, without disregarding possible nonlinearities introduced by signal saturation [92, 93]. Thereby, the constant-envelope bandpass signals can be expressed as

$$c\left(t\right) = A\cos\left[2\pi f_c t + 2\pi h \cdot x\left(t\right)\right], \tag{2.21}$$

for A, f_c and $0 < h \leq 1$ being its unitary signal amplitude, carrier frequency and phase modulation index, respectively [91, 94]. It is important to emphasize that the modulating signal $x(t)$ should be normalized (amplitude between -1 and 1) to evaluate the impact of the phase modulation index.

The root-mean-square bandwidth of the CE-OFDM signals is expressed as $B = \max(2\pi h, 1)B_{\mathrm{w}}$, for B_{w} the bandwidth of the OFDM modulating signal

$$x(t) = \sum_{k=1}^{N_{\mathrm{s}}} \Re[X(k)] \cos\left(\frac{2\pi kt}{T}\right) - \Im[X(k)] \sin\left(\frac{2\pi kt}{T}\right), \tag{2.22}$$

with $\{X(k)\}_{k=1}^{N_{\mathrm{s}}}$ the Quadrature Phase-Shift Keying (QPSK) or M-ary quadrature amplitude modulation (M-QAM) symbols, $\Re[\cdot]$ and $\Im[\cdot]$ the real and imaginary parts of $X(k)$, $T_{\mathrm{N}} = \frac{N_{\mathrm{s}}}{F_{\mathrm{s}}}$ the symbol duration and F_{s} the sampling rate [25]. Note that Hermitian symmetry needs to be established on the subcarriers in order to produce real-valued OFDM signals. Thus, a fast-Fourier transform length of $N_{FFT} = 2N_{\mathrm{s}} + 2$ is used to multiplex the subcarriers.

2.2.5. Performance Metrics

2.2.5.1. Bit Error Rate

Bit Error Rate (BER) is a metric in digital communication systems, representing the ratio of erroneous bits to the total transmitted bits over a communication channel [95]. It is a quantitative measure of data transmission performance, which is affected by noise, signal distortion, and interference. A lower BER indicates superior transmission quality, whereas a higher BER implies low-quality performance.

2.2.5.2. Error Vector Magnitude

Error Vector Magnitude (EVM) is a metric to evaluate the performance and quality of digital communication systems. It quantifies the average deviation between the transmitted (expected) and the received complex symbols by calculating Root Mean Square (RMS) of the sum of squared errors [96, 97]. Mathematically, EVM is defined as:

$$\mathrm{EVM}_{\mathrm{RMS}} = \sqrt{\frac{1}{N_{\mathrm{symb}}} \sum_{t=1}^{N_f} \frac{\sum_{k=0}^{N-1} \left|X[k] - \hat{X}[k]\right|^2}{\sum_{k=0}^{N-1} |X[k]|^2}} \tag{2.23}$$

where N_{symb} is the number of transmitted symbols, $X[k]$ represents the $k-\mathrm{th}$ transmitted symbol and $\hat{X}[k]$ is the corresponding received symbol. This metric is often presented in Decibel (dB) by converting it as follows:

$$\mathrm{EVM}_{\mathrm{dB}} = 10 \times \log_{10}(\mathrm{EVM}_{\mathrm{RMS}}). \tag{2.24}$$

2.2.5.3. Peak-to-Average Power Ratio

The OFDM Signals exhibit a high peak-to-average ratio. This occurs due to the aggregation of various narrowband subsymbols in the time domain, which occasionally results in significantly large peaks that amplify the difference between the peak and average power of the OFDM signals [98]. This phenomenon, referred to as PAPR, has a critical impact on system performance, especially in the presence of nonlinear distortions caused by components such as Analog-to-Digital Converter (ADC) and power amplifier. These components are often operated near their saturation point to maximize efficiency. A high PAPR can cause the signal to exceed the dynamic range of devices like LEDs, leading to signal saturation and introducing nonlinearities that degrade communication performance. The PAPR is mathematically expressed as:

$$\mathrm{PAPR} = \frac{\max\limits_{0 \leq t < L \cdot T} |s(t)|^2}{P_s}, \tag{2.25}$$

where L is the number of observed modulated signal blocks and $P_s = \frac{1}{T}\int_0^{LT} |s(t)|^2 \, dt$ is its average power [99]. In contrast to conventional OFDM formats that generate modulated signals with high PAPR (typically above 10 dB), the CE-OFDM signals described in Section 2.2.4 provide multicarrier signals with PAPR of only 3 dB for unitary CE-OFDM signals ($A = 1$) [91, 100].

2.3. Artificial Intelligence and Metaheuristic Optimization

2.3.1. Genetic Algorithm

A GA is a population-based metaheuristic inspired by the process of natural selection and genetic inheritance of living organisms [101]. Based on Darwin's theory of evolution, GAs mimic the biological evolutionary processes to find high-quality solutions for complex problems by combining mechanisms such as selection, crossover (recombination), and mutation [102, 103]. Therefore, GAs are classified as evolutionary algorithms and are widely used to solve optimization and search problems.

The algorithm begins by generating an initial population of candidate solutions to a given problem. Each candidate solution is represented as a set of variables or parameters known as the individual's chromosome. The algorithm evaluates each individual's fitness in the population based on a fitness function that quantifies how well an individual solves the problem. Individuals with higher fitness values are more likely to survive and pass their genetic material to the subsequent generation.

The selection operation involves choosing individuals from the current population to serve as parents for reproduction, based on their fitness values. Typically, individuals with higher fitness scores are more likely to be selected, as they are expected to produce better offspring

during the subsequent crossover phase. There are many selection operators, such as roulette wheel selection, tournament selection, ranking selection, and random selection, among others. In roulette wheel selection, which is applied in this thesis, the individuals are chosen based on their fitness. Each individual is associated with a segment of a "roulette wheel" proportional to its fitness. The wheel is spun, and the individual corresponding to the selected segment is chosen for reproduction. This method favors fitter individuals while maintaining genetic diversity.

The crossover is one of the most important operations in GA, as it combines the genetic material of two parent individuals to create new offspring. The goal of crossover is to explore new areas of the solution space by mixing the strengths of parent solutions, potentially producing offspring with enhanced performance. Common crossover techniques include single-point, multi-point, and uniform crossover, among others. This process provides diversity in the population, which is essential for promoting the search for optimal or near-optimal solutions.

The Mutation is responsible for maintaining genetic diversity by introducing random changes to the genes of an individual solution, simulating the natural process of genetic mutation. This helps prevent premature convergence by exploring new areas of the solution space and escaping local optima. The mutation is typically applied considering a low probability to avoid excessive disruption to the population.

The genetic operations of selection, crossover, and mutation are applied to the population to produce the next generation of individuals. The GA loop can be described as follows:

1. selection from the current population for reproduction based on their fitness values;
2. offspring generation by applying the crossover and mutation operators on the selected individuals;
3. offspring fitness evaluation;
4. selection of the survivals from the current population and offspring to compose the next generation.

This process is repeated over multiple generations. Eventually, the algorithm converges towards an optimal solution, which is a candidate solution with the highest fitness value.

2.3.2. Decision Tree

Decision trees are a widely used ML algorithm for classification and regression tasks due to their interpretability, simplicity, and effectiveness [104, 105]. They represent decisions in a hierarchical, tree-like structure, where each internal node corresponds to a feature or attribute, each branch represents a decision rule, and each leaf node represents an outcome or class label.

A decision tree starts at a root node and branches out based on decision rules derived from the features of the dataset. These rules are created to divide the data into subsets that are as homogeneous as possible. The process can be divided into the following components:

- Root Node: this is the starting point of the tree that serves as the input to the dataset. The algorithm determines the most important feature to split the data at this level;
- Internal Nodes: these are intermediate decision points where the dataset is further divided based on selected feature thresholds or categorical values;
- Leaf Nodes: these terminal nodes represent the final output, which can either be a class label (for classification) or a predicted value (for regression).

Figure 2.8 presents a simple decision tree example that illustrates the choice between "go to the beach" or "stay at home". The decision tree first examines if it is a sunny day or not. If it is not sunny, then the tree predicts to stay at home. Otherwise, the tree proceeds to evaluate if it is windy. If the day is windy, the prediction remains to stay at home. If not, the tree predicts to go to the beach.

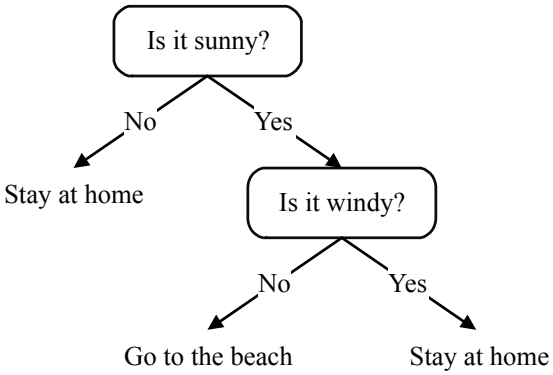

Figure 2.8. Decision tree example for choosing between "go to the beach" or "stay at home".

2.3.3. Artificial Neural Network

According to [106], an Artificial Neural Network (ANN) can be defined as a computational model inspired by the structure and function of biological neural networks. It consists of a collection of interconnected processing units, known as neurons, organized in layers. These neurons operate in parallel and can adapt through experiential learning, where the network adjusts its parameters based on the data it processes, enabling it to perform tasks such as pattern recognition, classification, and prediction.

A neuron is an essential information-processing unit for the operation of a neural network [106]. The schematic representation in Figure 2.9 illustrates the model of a neuron, which is the basis for ANNs. This model can be divided into three primary components: a set of synapses, which weigh the input signals; an adder that is responsible for summing the weighted signals and the bias; and an activation function for limiting the output amplitude of a neuron.

The model depicted in Figure 2.9 includes a bias (b_k) which can increase or decrease the net input of the activation function (φ). Mathematically, a neuron k can be expressed by the

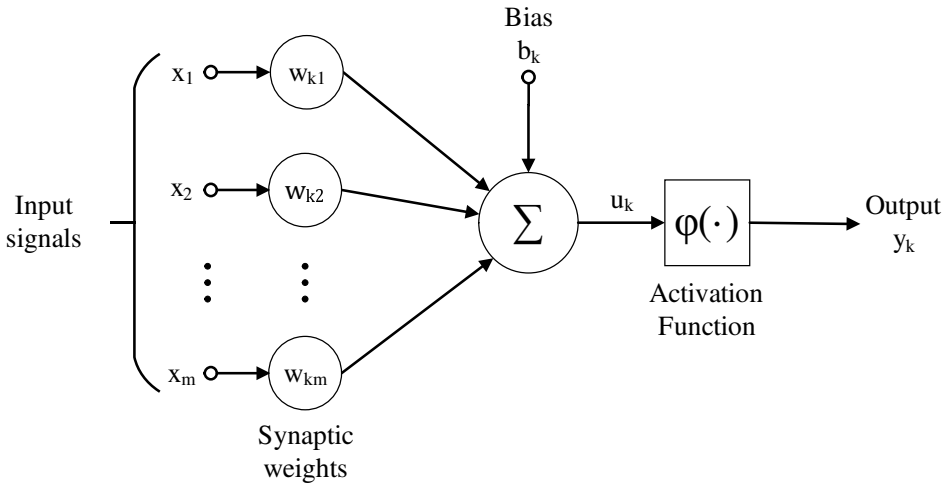

Figure 2.9. Model of a neuron.

following equations:

$$u_k = \left[\sum_{j=1}^{m} w_{kj} x_j\right] + b_k \tag{2.26}$$

and

$$y_k = \varphi\left(u_k\right), \tag{2.27}$$

where x_j is the j-th signal input, w_{kj} represents the j-th weight of neuron k, b_k is the bias, $\varphi\left(\cdot\right)$ denotes the activation function, and y_k is the output of the neuron.

The activation functions play an important role in ANN as they can introduce nonlinearity to the model. Additionally, there are a lot of activation functions in the literature [107]. In this thesis, we applied the activation functions sigmoid and tanh, where their equations are described as:

$$\text{sigmoid}\left(x\right) = \frac{1}{1+e^{-x}}; \tag{2.28}$$

and

$$\tanh\left(x\right) = \frac{e^{x}-e^{-x}}{e^{x}+e^{-x}}. \tag{2.29}$$

Figure 2.10 illustrates the curve for sigmoid and tanh. Therefore, as this thesis considers classification problems, we applied the softmax activation function as it converts a vector of K numbers into another vector of K numbers, where the sum of the values is equal to 1. This property makes the output interpretable as probabilities. It is a generalized version of logistic regression, specifically suited for classification tasks where the classes are mutually exclusive. Consequently, it is commonly applied in multi-class classification problems [108]. The mathematical representation of the softmax function is as follows:

$$\text{softmax}(\mathbf{z})_i = \frac{e^{z_i}}{\sum_{j=1}^{K} e^{z_j}}. \tag{2.30}$$

where $\mathbf{z}$ is the input vector, z_i represents the i-th element of the input vector, and K is the number of classes.

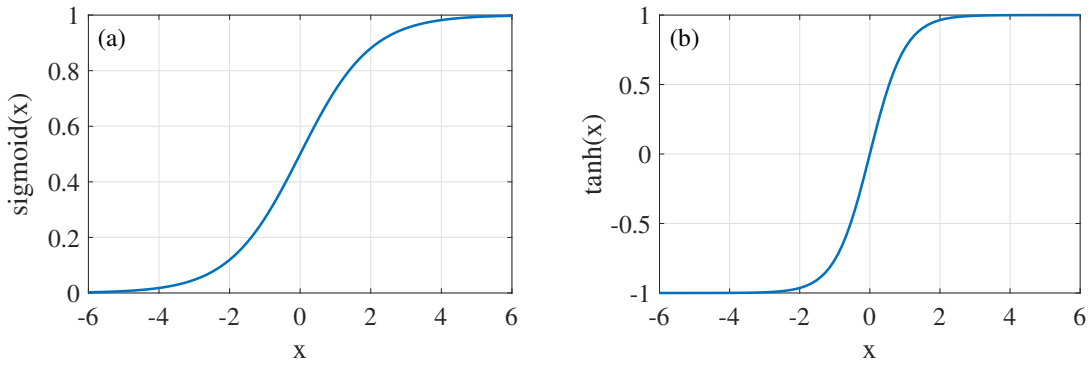

Figure 2.10. Activation functions.

An architecture of a neural network can be single-layered, consisting only of input nodes (which do not process signals) and an output layer of neurons, or multi-layered, where the output signals from a layer serve as input for the subsequent layer, continuing until the output layer [106, 109]. The layers between the input nodes and the output layer are known as hidden layers, which add robustness to the network by enabling the extraction of higher-order statistical features. For example, Figure 2.11 illustrates a fully connected 4-5-2 structure, representing 4 input nodes, 5 hidden neurons, and 2 output neurons. Additionally, in some cases, a neural network that is not fully connected increases robustness and prevents overfitting. Therefore, dropout is often applied to randomly deactivate a fraction of neurons during the training [110].

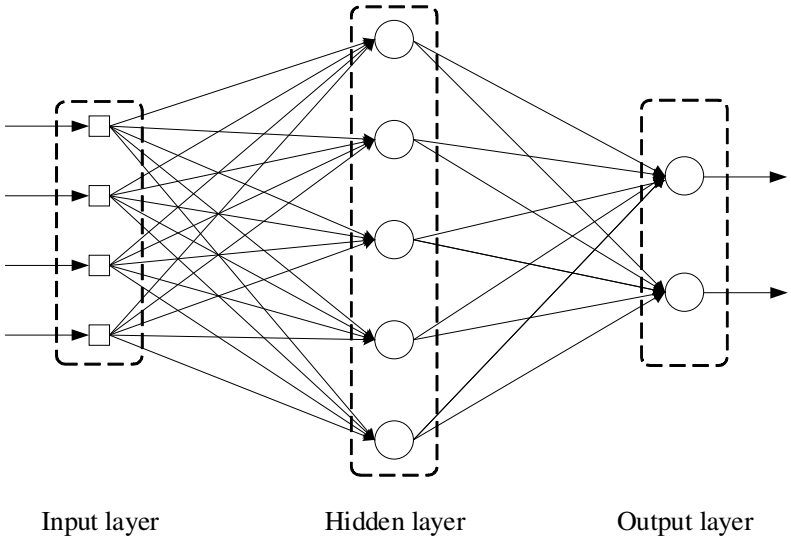

Figure 2.11. Fully connected feedforward neural network.

2.3.4. Categorical Cross-entropy

Categorical Cross-Entropy (CCE) is a widely used loss function in machine learning, particularly for classification tasks where the model predicts probabilities for multiple classes [111]. It measures the dissimilarity between the expected distribution and the predicted probability distribution generated by the model. For a dataset with N samples and C classes, the equation for CCE is:

$$\mathrm{CCE} = -\frac{1}{N}\sum_{i=1}^{N}\sum_{j=1}^{C} y_{ij}\log(p_{ij}), \tag{2.31}$$

where y_{ij} is a binary indicator (1 if class j is the correct class for sample i, 0 otherwise), and p_{ij} is the predicted probability for class j of sample i. It is particularly effective in scenarios with mutually exclusive class labels and is commonly used with softmax activation in the output layer of neural networks.

2.3.5. Long Short-Term Memory

Recurrent Neural Networks (RNN) are a type of artificial neural network designed to process sequential data by maintaining a memory of previous inputs through hidden states. Unlike traditional feedforward networks, RNNs have recurrent connections that allow them to persist information across time steps. These capabilities make RNN effective for time series analysis, language modeling, and speech recognition [112]. However, LSTM, a variant of RNN, addresses the vanishing gradient problem more effectively and presents a better performance at learning long-term dependencies in sequential data [113]. In literature, LSTM has been widely adopted for temporal series problems, demonstrating adequate results [114].

An LSTM cell, illustrated in Figure 2.12, contains four main components: forget gate, input gate, output gate, and cell state. The forget gate determines how much information from the previous cell state (h_{t-1}) is retained as the output of the activation function (φ), sigmoid is between 0 and 1. The input gate controls the incorporation of new data x_t and recurrent information (h_{t-1}) into the cell state by concatenating their vectors and applying the tanh activation function, which generates a candidate cell state ($\tilde{C}_t$). The updated cell state (C_t) is then computed by combining the outputs of the forget and input gates. Finally, the output gate determines which information is passed to the next instant of a LSTM cell. Using both a tanh and a sigmoid activation function, the LSTM cell produces the hidden state, h_t, which represents the recurrent output.

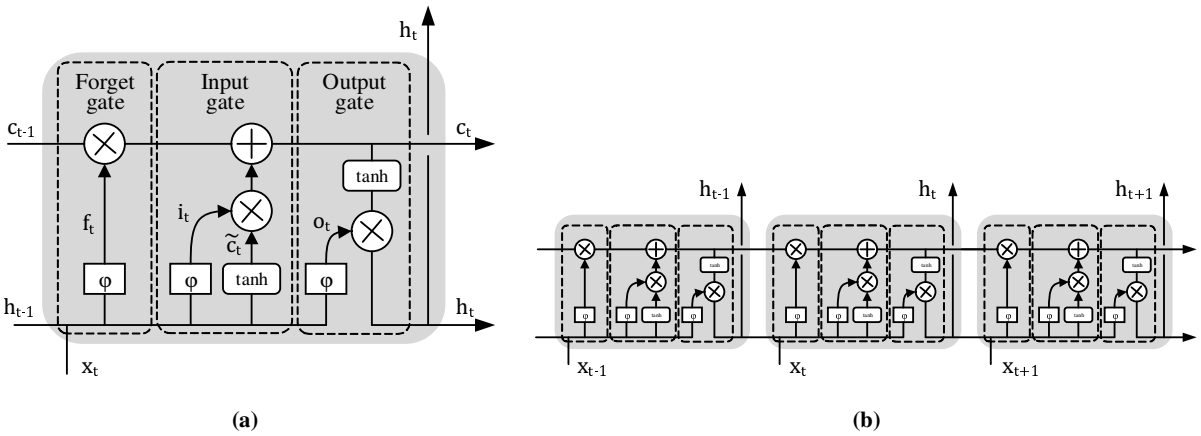

Figure 2.12. LSTM architecture. (a) LSTM cell structure (b) Chain structure of LSTM network.

The LSTM cell is defined by the following equations:

$$f_t = \sigma(W_f \cdot [h_{t-1}, x_t] + b_f) \quad \text{(Forget Gate)}, \tag{2.32}$$

$$i_t = \sigma(W_i \cdot [h_{t-1}, x_t] + b_i) \quad \text{(Input Gate)}, \tag{2.33}$$

$$\tilde{c}_t = \tanh(W_c \cdot [h_{t-1}, x_t] + b_c) \quad \text{(Candidate Cell State)}, \tag{2.34}$$

$$c_t = f_t \cdot c_{t-1} + i_t \cdot \tilde{c}_t \quad \text{(Updated Cell State)}, \tag{2.35}$$

$$o_t = \sigma(W_o \cdot [h_{t-1}, x_t] + b_o) \quad \text{(Output Gate), and} \tag{2.36}$$

$$h_t = o_t \cdot \tanh(c_t) \quad \text{(Hidden State Output)}, \tag{2.37}$$

where φ and tanh are sigmoid and hyperbolic tangent activation functions, respectively. x_t represents the input vector at time t, while h_t is the hidden state. c_t is the cell state that acts as the memory of the network. The weight matrices W_f, W_i, W_c, W_o and biases b_f, b_i, b_c, b_o are trainable parameters that correspond to the forget gate, input gate, candidate cell state, and output gate.

2.3.6. Temporal Convolutional Network

Like RNNs, CNN have been widely applied, showing impressive results for problems involving sentence classification and time-series [115]. Temporal Convolutional Networks (TCN) is recently powerful architecture proposed in 2016 that combines RNNs and CNNs [116]. TCN involves two main steps: first, extracting low-level features, often using a CNN, to encode spatiotemporal information, and second, passing these features into a classifier, commonly an RNN, to capture higher-level temporal patterns. This approach is robust against vanishing gradients because it processes sequences with parallel convolutional layers instead of recurrent connections, eliminating sequential backpropagation issues. The architecture of a TCN is based on several distinct design principles that enable it to excel in temporal modeling [117]. The key components are:

- causal convolutions, ensuring that the output at a given time step depends only on past inputs and not future ones. This property is crucial for many time series forecasting and prediction tasks;
- dilated convolutions, which allow TCNs to capture long-range dependencies in the input sequence without significantly increasing the number of parameters. By increasing the dilation factor, the receptive field of the network can be expanded exponentially; and
- residual connections, which often incorporate residual connections to facilitate the training of deep networks and mitigate the vanishing gradient problem.

2.3.7. Optuna Framework

Manually hyperparameter searching in machine learning can be, in general, a time-consuming and inefficient process that often leads to suboptimal model performance. Therefore, Optuna is an open-source hyperparameter optimization framework designed for machine learning and deep learning models [118]. It provides a flexible and efficient approach to automate the search for optimal hyperparameters by using advanced techniques like Bayesian optimization, Tree-Structured Parzen Estimator, and parallel processing. Optuna's key features are dynamic search spaces, and integration with popular machine learning libraries, making it a powerful tool for improving model performance.

CHAPTER 3.

Increasing the Reach of Visible Light Communication Links Through Constant-Envelope OFDM Signals

3.1. Introduction

As PAPR is an important characteristic to be considered in VLC systems due to the nonlinearities, different techniques were developed to reduce the PAPR and, accordingly, mitigate nonlinearity and increase the average transmitted power [22–24]. However, the PAPR reduction achieved in [22] and [23] are relatively small, and the complexity required by the transceiver suggested in [24] is high compared to OFDM-based VLC systems. As proposed in [25] and demonstrated in [119], the CE-OFDM scheme can help to mitigate fiber nonlinearities and increase the tolerance to intermodulation effects introduced by optical Mach-Zehnder modulators. Reducing the PAPR to only 3 dB, the CE-OFDM based system outperforms classical IM/DD optical OFDM systems [27]. The Spectral Efficiency (SE) reduction, that characterizes such phase modulation arrangements in IM/DD systems, was addressed in [26] via an optimization algorithm. The optimization proposed in [26] provided a bandwidth reduction of 66% in the inherent spectral broadening of CE-OFDM based optical IM/DD systems at the cost of a 2 dB power penalty.

It is accordingly expected that the adoption of CE-OFDM in VLC systems can improve the tolerance to noise and the nonlinearities introduced by LEDs. In this Chapter, to our knowledge for the first time, we experimentally demonstrate that a CE-OFDM VLC system can provide power efficiency and, in consequence, enhance the transmission distances. Therefore, the main contribution of this Chapter relies on the fact that we take advantage of low PAPR multicarrier signals to increase the reach of VLC systems. The impact of the phase modulation index and the LED bias current on performance was investigated to demonstrate the performance enhancement achieved with the CE-OFDM based SISO VLC system, as compared to a conventional OFDM VLC system. EVM improvements around 43% were achieved in a 9.51 Mb/s (16-QAM mapping) VLC link of 6 m. At 14.26 Mb/s (64-QAM subcarrier mapping), both systems achieved almost the same performance under link distances below 5 m. Nevertheless, only the CE-OFDM based system with 4-QAM as subcarrier mapping achieved good performance (EVM below the FEC limit) in VLC links of 8 m. We chose the EVM metric to evaluate the

performance in order to avoid the extremely long time required for a reliable computation of a BER in high-quality received signals, i.e., with low bit error rates [1].

The remainder of this Chapter is organized as follows. Related works are presented in Section 3.2. Section 3.3 described CE-OFDM applied in this Chapter. The experiments and results are presented in Section 3.4 and 3.5, respectively. Finally, the conclusion remarks are provided in Section 3.6.

3.2. Related work

Related works that consider link distances and PAPR reduction techniques are briefly described in this Section. VLC systems with link lengths above or equal to 12 m are reported in [120], [121], and [122]. The authors of these works employed optical sources that allow VLC at very high optical transmitted powers. Gallium Nitride (GaN) LEDs were used in [120] and [121], while a 680-nm Laser Diode (LD) was used in [122]. However, it should be stressed that in this work, we implemented VLC systems using an Off-the-shelf (OTS) and low-cost LED.

OTS LEDs are widely applied in VLC systems, despite the limitation related to optical power [44, 123–125]. The relative low distances achieved in [123–125] and [44] are due to the high PAPR of the utilized modulating signals. In this Chapter, we doubled the link length we achieved [44], by applying constant-envelope OFDM signals (low PAPR) as modulating signals to improve the tolerance to noise and the nonlinearity introduced by LEDs and, in consequence, increase VLC reach. Table 3.1 (a) shows details about these works.

In Table 3.1 (b), we list related works in which different PAPR reduction techniques were applied to VLC systems. In the theoretical works presented in [126] and [22], the authors suggested the Gaussian blur algorithm and an interactive clipping process to reduce the PAPR of Asymmetrically Clipped Optical (ACO) and conventional OFDM signals, respectively. Evaluations in terms of link distance were not assessed in these works. The efficiencies of a Filter Bank Spread (FBS) and an interleaved Discrete Fourier Transform Spread (DFT-S) scheme in PAPR reduction were experimentally demonstrated in [127] and [128], respectively. Aiming at side information cancellation and PAPR reduction, the authors of [129] proposed a clustered DC-biased optical OFDM scheme. Lu et al. [130] proposed the exponential companding, logarithmic companding, and selective mapping techniques to reduce PAPR and, therefore, improve the performance of conventional OFDM-based VLC systems. As shown in Table 3.1 (b), the lowest PAPR (5 dB) was achieved by the interleaved DFT-S method and the highest link distance (2.8 m) reached by a method based on the FBS. However, in this Chapter, we experimentally demonstrated the reach of VLC links up to 8 m, employing modulating signals with PAPR $= 3$ dB.

Table 3.1. Works considering: (a) link length, (b) PAPR reduction

Ref.	Modulation	PAPR	Dist.	Optical source
[120]	OFDM	High	20 m	GaN LEDs
[121]	OOK	Low	16 m	GaN LED
[122]	OOK	Low	12 m	680-nm LD
[123]	OFDM	High	1.6 m	OTS LED
[124]	CAP	Med.	4.5 m	OTS LEDs
[125]	OFDM	High	2.0 m	OTS LEDs
[44]	OFDM	High	4.0 m	OTS LED

CAP: carrier-less amplitude and phase.

(a)

Ref.	Reduction Method	Resulting PAPR	Dist.
[126]⋆	ACO-OFDM	$>$ 7.5 dB	NA
[22]⋆	Clipping	$>$ 6.0 dB	NA
[127]*	FBS-OFDM	$>$ 7.5 dB	2.8 m
[128]*	Inter. DFT-S	$>$ 5.0 dB	1.05 m
[129]*	Clust. DCO-OFDM	$>$ 7.6 dB	1.0 m
[130]*	Exp. companding	$>$ 7.5 dB	1.0 m
[130]*	Log. companding	$>$ 7.0 dB	1.0 m
[130]*	Selective mapping	$>$ 7.0 dB	1.0 m

⋆ Paper with simulation results; NA: not assessed;
* paper with experimental demonstration.

(b)

3.3. Constant-Envelope OFDM

As described in Section 2.2.4, the modulation scheme CE-OFDM achieves a lower PAPR, making it more robust against nonlinear distortion. Moreover, the discrete phase demodulator, implemented by an Arc-tangent (ARC) processor, as suggested in [91], is used in the receiver to recover the baseband OFDM signals. After the argument extraction, a phase unwrapper is used to minimize the effect of phase ambiguities caused by phase offsets introduced by the communication channel [25]. Compared to conventional OFDM systems, the ARC and the unwrapper are additional operations that increase the system complexity [91]. The added complexity can be reduced by the Taylor expansion based receiver structures developed in [131], that eliminate the need for the ARC processing and result in immunity from phase cycle slips.

The parameter $2\pi h$ plays an important role in the tradeoff between spectral efficiency and system performance [91], [26]. Low values of this phase index lead to noise sensibility, whereas higher values of $2\pi h$ enhance the system performance at the expense of an increased bandwidth and, accordingly, reduced SE. Taking this into account and based on the design provided in [132], we prepared an experimental setup to demonstrate the suitability of CE-OFDM based VLC systems at bit rates of approximately 4.75, 9.51 and 14.26 Mb/s with 4, 16 and 64-QAM as subcarrier modulation schemes, respectively, in a fixed bandwidth $B = 5$ MHz. In [132], the authors discuss the robustness against the flicker of CE-OFDM based systems when compared to VLC systems based on conventional OFDM. The experimental tests were conducted with a fixed link length without considering 64-QAM as subcarrier mapping. In this Chapter, we conducted experimental demonstrations considering link length up to 8 m with 4, 16, and 64-QAM as subcarrier modulation formats. The focus is to compare CE-OFDM and conventional OFDM performance against LED nonlinearity.

3.4. Experimental Setup

Figure 3.1 (a) depicts a block diagram of the experimental setup implemented to study the performance of the CE-OFDM based VLC system. In parallel, a conventional OFDM system with HS was equally set up in order to obtain a direct performance comparison. Using Matlab, pseudorandom binary sequences PRBS $= 4 \times (2^9)$ bits were mapped in $N_s = 16$ data symbols before the HS procedure used to generate real coefficient symbols, by adopting 4, 16 and 64-QAM as subcarrier modulation formats. The Hermitian symmetry was imposed in both types of multicarrier signals aiming at a fair comparison of both systems at the same throughput. It is important to note that, due to HS, a total of $N_z = 31$ subcarriers were zeroed to avoid aliasing. Thus, an IFFT of $N_{FFT} = 2 \times N_s + N_z + 1 = 64$ points was used to multiplex the subcarriers.

A CP of $T_g = 10 \times \tau = 150$ ns was added to eliminate the inter-symbol interference induced by channel delay spread [46]. As delay spread, we used the same ($\tau = 15$ ns) considered in our previous work (see Section 2.3.2 of [132]). With useful signal duration of $T = 50 \times T_g = 7.5$ μs,

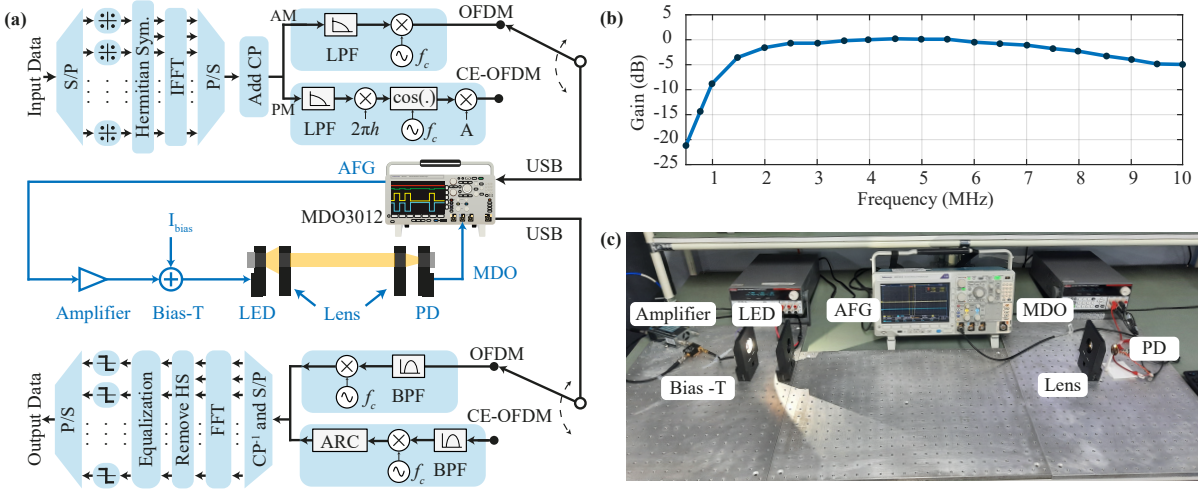

Figure 3.1. (a) Schematic view of the experimental CE-OFDM and OFDM-based VLC system setups. AM: Amplitude Modulation; PM: Phase Modulation. (b) Measured frequency response of the VLC channel in B2B (measured with a spectrum analyzer at a transmission distance of ≈ 0 m). (c) A picture of the components involved.

the total duration of the multicarrier signals was $T_s = T + T_g = 7.65\ \mu$s. Hence, the subcarriers spacing is $\Delta_f = T^{-1} = 133.3$ kHz and the minimum bandwidth demanded by both systems is $B = \Delta_f \times (2 \times N_s + 1) = 4.4$ MHz.

Then, the OFDM and CE-OFDM signals were loaded into a 250 MSamples/s Arbitrary Function Generator (AFG). The central frequency chosen for the analog carrier was $f_c = 7.5$ MHz to avoid the attenuation observed in the frequency range below 2 MHz shown in Figure 3.1 (b). Also, due to this reason, and for the sake of simplicity, we adopted 5 MHz as the system bandwidth. The raw bit rate of the systems can be calculated as [133]:

$$R = \frac{B}{(N_{FFT} - N_z)} \times \frac{N_s \times \log_2(M)}{(1+G)}, \tag{3.1}$$

in which M is the subcarrier modulation order and $G = \frac{T_g}{T}$ is an overhead factor related to CP. Thus, for $G = 1/50$, the bit rates of both systems are 4.75, 9.51 and 14.26 Mb/s when 4, 16 and 64-QAM are used as subcarrier mapping, respectively. A summary of the signals parameterization is presented in Table 3.2.

The analog signals available at the AFG output were amplified and superimposed onto a bias current, aiming to provide non-negative waveforms. The output of the Picosecond Pulse Labs (Model 5575A, bandwidth 12 GHz, $I_{DC} \leq 500$ mA) Bias-Tee was directly supplied to a commercial LumiLED LXML-PWC2 white LED. Figure 3.2 shows the measured V-I and P-I characteristics of this specific LED, for P the illuminance obtained by a luximeter located at 0.5 m away from the LED. It can be observed from the P-I diagram depicted in Figure 3.2 that $I_{bias} \geq 1000$ mA leads to a significant nonlinearity between the illuminance and the bias current.

Table 3.2. Summary of experimental settings.

Parameter	Variable	OFDM
Bandwidth	B	5 MHz
(I)FFT size	N_{FFT}	64
Data subcarriers	N_s	16
Zeroed subcarriers	N_z	31
Subcarrier mapping	M	4, 16, 64-QAM
Cyclic prefix	CP	2%
Oversamp. factor	K	4
Central frequency	f_c	7.5 MHz

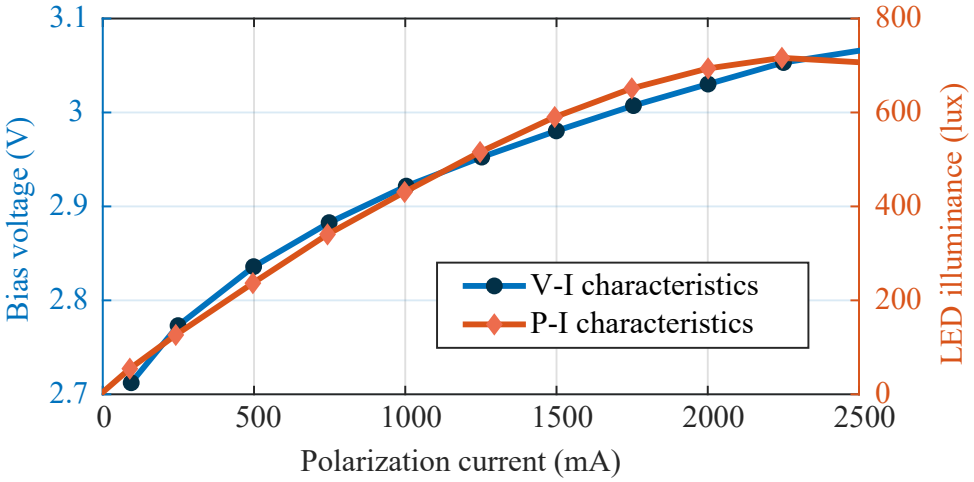

Figure 3.2. Measured V-I and P-I curves of the commercial LumiLED white-light LED.

After propagation through the LOS channel, supported by bi-convex lenses (optical concentrators), the VLC signals were detected by a HAMAMATSU S10784 photodiode before analog-to-digital conversion by a 2.5 GSamples/s Mixed Domain Oscilloscope (MDO) and offline signal processing. Figure 3.1 (c) depicts a photo of the setup.

3.5. Results and Discussions

The experimental results obtained with the previously described CE-OFDM modulation scheme in VLC systems are discussed in this section, which mainly focuses on the impact of the optical modulation index and the LED bias current, as well as on the system performance with varying link lengths.

3.5.1. Impact of Phase Modulation Index

In order to identify noise limited and nonlinearity performance regions, we evaluated the EVM performance varying the electrical phase modulation index $2\pi h$ in optical Back-to-back

(B2B), with a bias current equal to $I_{bias} = 1000$ mA and a distance of 1 meter. Figure 3.3 shows the variation of EVM with the parameter $2\pi h$ of the proposed CE-OFDM based system, considering 4, 16, and 64-QAM as modulation schemes. It is possible to conclude from the results depicted in Figure 3.3 that the optimum values of the phase modulation index for 4-QAM are in the region $4.5 \leq 2\pi h \leq 6$. Below this range, the system is affected by noise, whereas above it, the system performance is impacted by nonlinearities [27].

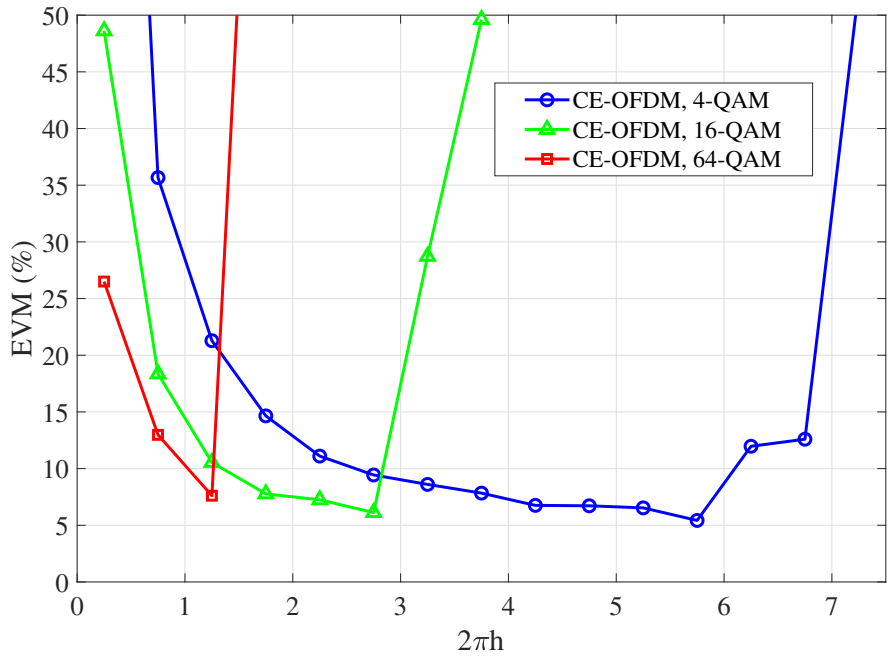

Figure 3.3. EVM as a function of the phase modulation index $2\pi h$, measured in B2B with 4, 16 and 64-QAM modulation schemes.

Figure 3.3 also shows that, for 16-QAM and 64-QAM, the optimun values are in the regions $1.5 \leq 2\pi h \leq 2.5$ and $0.7 \leq 2\pi h \leq 1.3$, respectively. Therefore, in the case of 4-QAM subcarrier mapping, we chose $2\pi h = 5.8$ as the optimum value, whereas for 16-QAM and 64-QAM the chosen optimum values were $2\pi h = 2$ and $2\pi h = 1$, respectively. For the last two subcarrier mappings, we choose modulation indexes immediately lower than the ones that provided the best performance in order to take into account the spectral broadening that increases with $2\pi h$ [26, 91].

3.5.2. Influence of LED Bias Current on the Performance

In Figure 3.4, the variation of the EVM values with the LED bias current is depicted for both the CE-OFDM and the conventional OFDM system, for the VLC links of 1 m and 4 m. The results depicted in Figure 3.4 (a) show that, excepting the performances obtained with 64-QAM, the CE-OFDM VLC based system outperforms the OFDM-based system for bias currents between approximately 700 mA and 1250 mA. For currents above 1250 mA, particularly at 1500 mA, receiver saturation occurs due to the short link distance, leading to an increase

in EVM. In contrast, at 4 m (Figure 3.4 (b)), the same issue did not occur due to the signal attenuation over the longer link. Additionally, for 1 m and bias currents lower than 1250 mA, the performance of both systems was almost the same when using 64-QAM subcarrier mapping. At a 4 m link distance, the CE-OFDM outperforms conventional OFDM across all evaluated currents, especially at high currents where LED-nonlinearities are more pronounced.

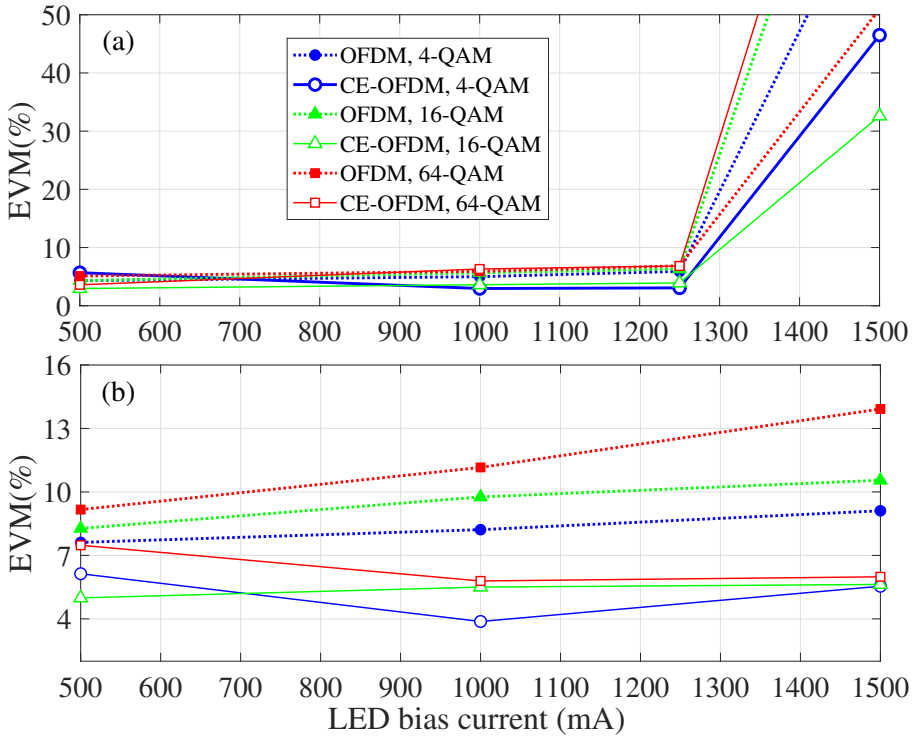

Figure 3.4. (a) Variation of EVM over the LED bias current I_{bias} across a VLC link of 1 m, for both OFDM and CE-OFDM VLC systems. (b) The variation for a VLC link of 4 m.

The results shown in Figure 3.4 (a) suggest that for all addressed modulation schemes, the bias currents between $1000 \leq I_{bias} \leq 1250$ mA can be employed for performance enhancement purposes. However, according to the measurement shown in Figure 3.4 (b), obtained with a VLC link of 4 m, we choose $I_{bias} = 1000$ mA, even knowing that this value represents the current limit ($I_{bias} = 1000$ mA) suggested by the manufacturer [134].

3.5.3. System Performance at Different Link Lengths

Based on the assessed optimum values of $2\pi h$ and I_{bias}, we performed a further comparison between the two multicarrier modulation schemes by varying the transmission distance. Corresponding results, shown in Figure 3.5, demonstrate that in almost all considered distances and subcarrier modulations, the proposed modulation scheme outperforms the OFDM-based system, due to the low PAPR provided by its CE-OFDM signals. In VLC links below 1 m, the performances of both multicarrier systems are impacted by signal saturation registered in the optical reception [19], [93]. This effect is overcome only with the CE-OFDM based system when 4-QAM is employed as subcarrier mapping.

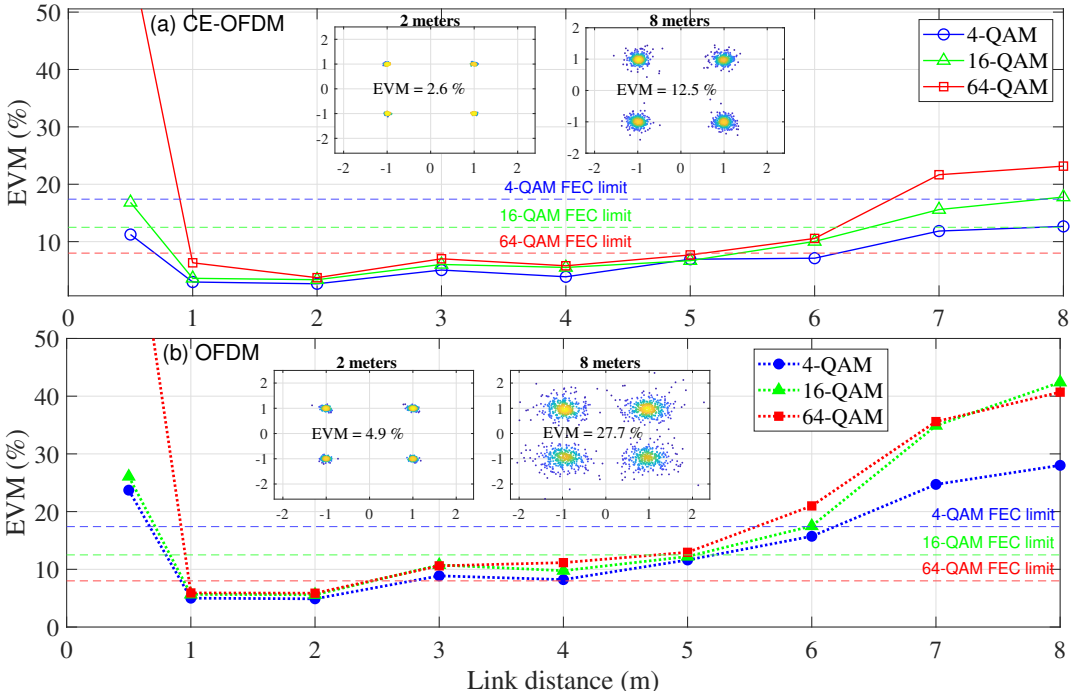

Figure 3.5. EVM versus link lengths, considering $I_{bias} = 1000$ mA, for (a) CE-OFDM and (b) OFDM signals. The insets show 4-QAM constellations measured at VLC links of 2 m and 8 m.

The results presented in Figure 3.5 show that at 2 m both systems have good performances with all considered modulation formats. When 4-QAM is used as subcarrier mapping, the OFDM-based VLC system achieved an EVM around 4.9%, whereas the system with constant-envelope signals reaches 2.6%. This slight performance enhancement is illustrated by the inset constellation diagrams.

Figure 3.5 also shows that at 6 m, an EVM improvement around 43% was achieved when the performance of the systems with and without CE-OFDM signals were compared, considering 16-QAM as the modulation scheme. With this subcarrier mapping, the VLC system based on conventional OFDM achieved poor performances (EVM above the FEC limit) at link distances greater than 5 m. At VLC links of 8 m, only the CE-OFDM based system with 4-QAM achieved a good performance, as verified by the EVM values below the correspondent FEC limit shown in Figure 3.5. The constellation diagrams shown in the insets of Figure 3.5 clearly illustrate that the CE-OFDM system outperforms the VLC system with conventional OFDM signals at the link length of 8 m. This is explained by the tolerance of the CE-OFDM based system to the nonlinearity introduced by the employed LED (see $P - I$ curve depicted in Figure 3.2). It is straightforward to notice that when the LED is biased with $I_{bias} \geq 1000$ mA, the modulating signals with higher values of PAPR are more impacted by clipping. Therefore, it can be concluded that, due to the low PAPR signals, the CE-OFDM based system outperforms the VLC system based on conventional OFDM at the higher link distances. When 64-QAM is used as the modulation scheme, the system with constant-envelope signals achieved 5 m, against the 2 m reached by the OFDM based system.

Considering the FEC limits, Figure 3.6 and Table 3.3 show the maximum throughput achieved in each link distance. At the distances of 0.5, 7, and 8 m, only the CE-OFDM based system performed below the FEC limit. In these scenarios, throughputs around 4.75 Mb/s were achieved with 4-QAM as subcarrier mapping. At 1 and 2 m, both systems achieved a maximum data rate of 14.26 Mb/s using 64 as QAM modulation order. From 3 to 5 m, the CE-OFDM reached 14.26 Mb/s against the 9.51 Mb/s (with 16-QAM) of the OFDM-based system. At the link length of 6 m, 9.51 Mb/s and 4.75 Mb/s were reached by CE-OFDM and OFDM, respectively.

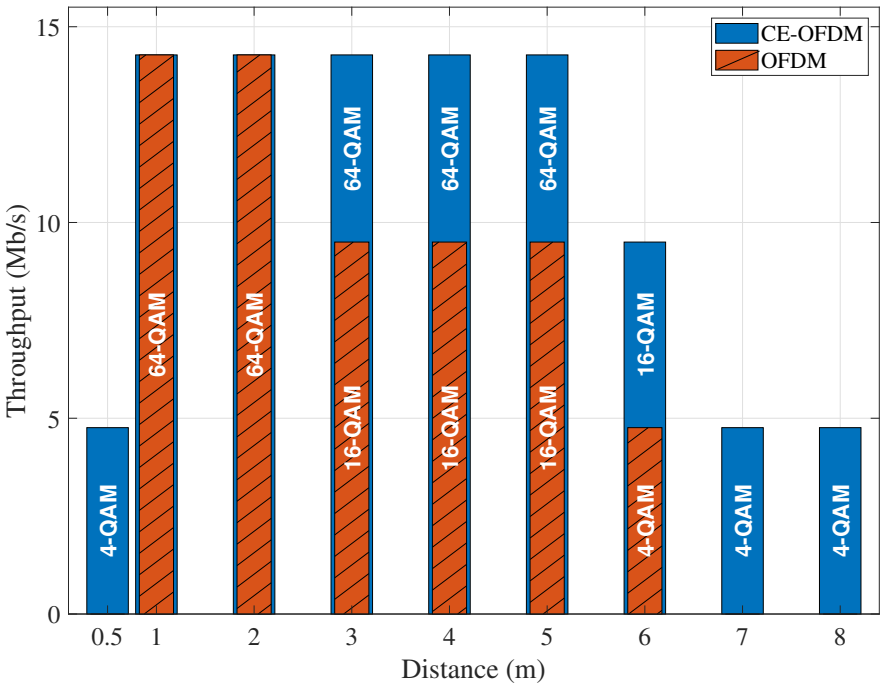

Figure 3.6. Throughput versus link length.

The above-described results show that VLC systems with CE-OFDM signals outperform the systems without such a phase modulation scheme, especially in relatively long links. This is attributed to the provided low PAPR signals that enhance the tolerance against system nonlinearities, as well as the signal-to-noise ratio reductions registered at long distances.

3.6. Conclusions

A PAPR reduction technique based on electrical constant-envelope OFDM signals was implemented in a VLC system. CE-OFDM modulation improves the tolerance to noises and nonlinearities introduced by LEDs and, as a consequence, provides power efficiency and transmission distance enlargements. The impact of the phase modulation index was investigated, and the experimental results showed its dependence on subcarrier modulation levels. A performance comparison between VLC systems with and without constant-envelope signals was conducted based on measured variations of the error vector magnitude. Experimental results show that

Table 3.3. Maximum throughput for OFDM and CE-OFDM at different distances.

Distance	CE-OFDM Throughput	OFDM Throughput
0.5 m	4.75 Mb/s	-
1 m	14.26 Mb/s	14.26 Mb/s
2 m	14.26 Mb/s	14.26 Mb/s
3 m	14.26 Mb/s	9.51 Mb/s
4 m	14.26 Mb/s	9.51 Mb/s
5 m	14.26 Mb/s	9.51 Mb/s
6 m	9.51 Mb/s	4.75 Mb/s
7 m	4.75 Mb/s	-
8 m	4.75 Mb/s	-

the system with CE-OFDM signals outperforms the OFDM-based system, notably at the high values of the bias current (nonlinear region of the LED).

The power efficiency provided by the signals with a PAPR of 3 dB contributed to a constant EVM improvement for almost all link lengths considered. At short link lengths, where signal saturation is predominant at the receiver, EVM improved by 52.6% when applying CE-OFDM with 4-QAM as the modulation scheme. At longer distances, EVM improvements of about 54% and 43% were still observed with 4-QAM at 8 m and 16-QAM at 6 m, respectively, mainly due to the tolerance to nonlinearity assured by constant-envelope signals.

Optimization of parameters such as optical and phase modulation indexes, LED bias current, and amplitude of the modulating signals using optimization algorithms are part of our future work, aiming at power and spectral efficiency enhancements. Before the application of the evaluated solution in practical industrial scenarios, we should conduct performance evaluations of CE-OFDM based VLC systems in non-line-of-sight channels, as well as in multiple transmitter environments, in order to analyze the impact of handover.

CHAPTER 4.

Experimental and Numerical Performance Evaluations of the VLC Systems

4.1. Introduction

The VLC mathematical models described in Section 2.1.1 are widely applied in the literature for evaluation of modulation schemes [135], handover strategies [33], vehicular applications [136], parameters optimization [44], as well as assessments of power and spectral efficiencies [137]. In [44] we proposed a "timid" digital twin in which the mathematical models are closely aligned with an actual experimental setup. This digital twin approach facilitates the use of metaheuristics to optimize parameters such as bias current, signal amplitude, and guard band within the simulation environment. Hence, this Chapter examines the effects of bias current and communication signal amplitude on the performance of a SISO VLC system across lateral and horizontal displacements [138]. Analyzing these parameters is crucial to optimizing system efficiency and performance. This Chapter also evaluates the effectiveness of the numerical models in replicating the SISO and MISO experimental scenarios. At a height of 150 cm, the SISO models achieved an EVM Root Mean Squared Error (RMSE) of 0.36%, while the MISO configuration presented EVM RMSEs of 1.37% and 1.65% for transmitters Tx1 and Tx2, respectively.

Despite the advantages of CE-OFDM for long links and robustness to noise, as discussed in Chapter 3, OFDM was chosen as the standard modulation scheme for 5G networks [139]. Therefore, we adopt OFDM as the modulation scheme in this and in the following Chapters. The remainder of this Chapter is structured as follows. Section 4.2 describes the LED assembly in our transmitter and its characteristics. The evaluations of a SISO setup are presented in Section 4.3. In Section 4.4, the evaluations of the simulation model replicating the real SISO and MISO experimental setups are presented. Finally, Section 4.5 summarizes the conclusions.

4.2. LED Characterization

Since this work considers both environmental illuminance and connectivity, we selected the low-cost commercial Chip-on-board (CoB) CREE CXA1507 5000K LED, which can reach 13.5 W. Figure 4.1 shows the mounted LED in a heat sink for thermal management. The transmitter setup also includes an SMA connector to receive the signal input, which is directly

connected to the LED, a ball head for fine adjustments, a bubble level for precise alignment feedback, and support for lenses.

Figure 4.1. Mounted LED.

The optical spectrum reveals the radiant intensity of the LED across various wavelengths. Figure 4.2 (a) shows the optical spectrum of the selected LED, highlighting two distinct peaks in radiant intensity. The first peak occurs in the blue light range, between 450 and 470 nm, while the second peak appears between 495 and 570 nm. Figure 4.2 (b) illustrates the measured voltage-current (V-I) curve of the CREE CXA1507 LED. The measurement includes the effect of the cable running from the power supply to the LED's SMA connection, as shown in Figure 4.1. The current was controlled by the power supply, varying between 50 and 450 mA. Figure 4.2 (c) shows the illuminance curves measured as a function of the LED bias current. The measurements were taken at various distances using a portable luxmeter (THDL-400 model), aligned with the LED. The curves reveal a slight non-linearity as the current increases.

4.3. Experimental Setup of the SISO VLC System

Figure 4.3 presents the block diagram of the SISO experimental setup, designed to evaluate the performance of the VLC system and its components. The signals are generated in Matlab and loaded into a Tektronix MDO3012 oscilloscope, used as an AFG and digital-to-analog converter. These analog signals are then amplified by a Juntek DPA-2698 amplifier, providing a gain of 6 dB. To ensure non-negative amplitudes for the CXA1507 LED, the amplified signals are combined with the bias current using a Bias-Tee Picosecond Pulse Labs model 5575A. The analog signals, received by the commercial Hyperion VLC receiver [140] illustrated in Figure 4.4 (a), are converted back to digital form by the MDO3012, after which the signals are processed offline using Matlab. Figure 4.4 (b) illustrates the system's link frequency response.

To evaluate communication performance, we transmitted 5G New Radio (NR) signals with a bandwidth of 1 MHz using the above-mentioned SISO VLC system. The central frequency of the signals was set to 0.75 MHz, as it lies within a flat region of the link's frequency response

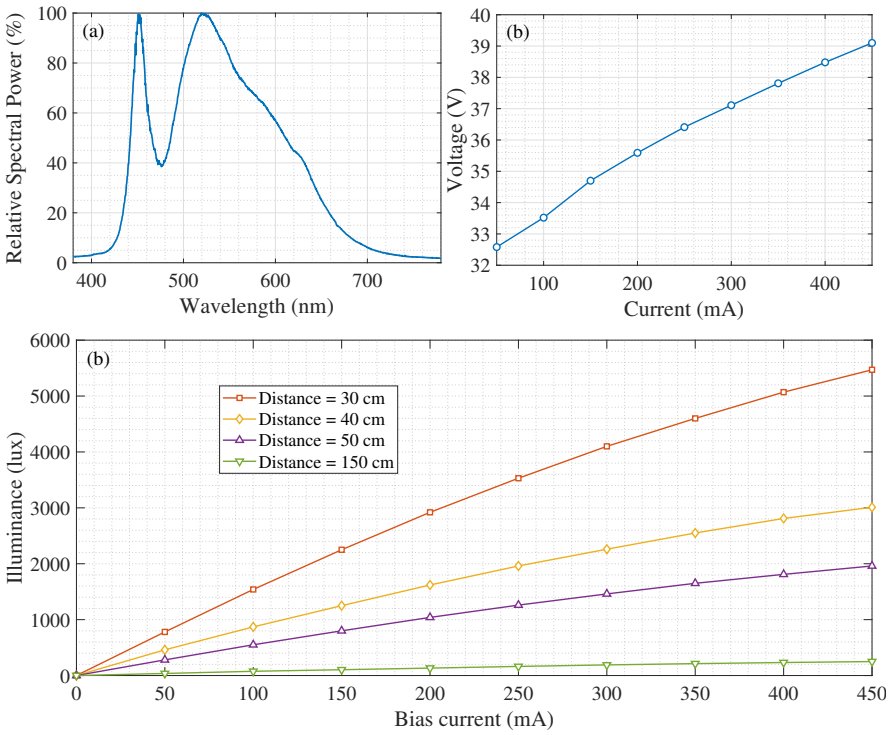

Figure 4.2. Results of the CREE CXA1507 LED characterization. (a) Measured relative power spectral distribution. (b) Measured current-voltage curve. (c) Measured current-lux curve.

(see Figure 4.4 (b)). The NR signals consist of 42 data subcarriers, multiplexed using a 128-point FFT, with 4-QAM applied for subcarrier mapping. Given a subcarrier spacing of 15 kHz, the total bandwidth is approximately 1 MHz. A cyclic prefix of 16 samples was added at the beginning of each NR signal to mitigate intersymbol interference.

Aiming at the evaluation of the impact of bias current, signal amplitude, and link distance on the VLC system, we perform tests varying the bias current (I_{bias}) from 100 mA to 300 mA, the AFG output (V_{pp}) from 500 mV to 4000 mV, and the height from 50 cm to 250 cm. The test scenario considers the SISO system with the transmitter centered in a 2-meter straight trajectory (from A to B) followed by the receiver considering steps of 25 cm (see the 2D representation depicted in Figure 4.5).

Figure 4.6 shows the results for an AFG output of 500 mV and bias currents of 100, 200 and 300 mA. Considering $I_{\text{bias}} = 100$ mA and a link height of 50 cm, the results demonstrated high EVM at distances before 0.5 and beyond 1.5 m, due to the edges around the LED of the transmitter (see Figure 4.1), which limited the FOV. In Figure 4.6 (b), at 50 cm, the system presented saturation at all intermediate points, except for 0.5 and 1.5 m, due to the bias current of 200 mA, which provided higher light intensity at the receiver. In Figure 4.6 (c), where the bias current is even higher (300 mA), saturation is observed across all midpoint distances. At other link heights, saturation was not observed; however, only the links between 0.25 and 1.75 m, and from 0.75 to 1.25 m presented EVM values below the 4-QAM FEC limit (17.4%) for link heights of 100 cm and 150 cm, respectively. Additionally, performance remained stable as the

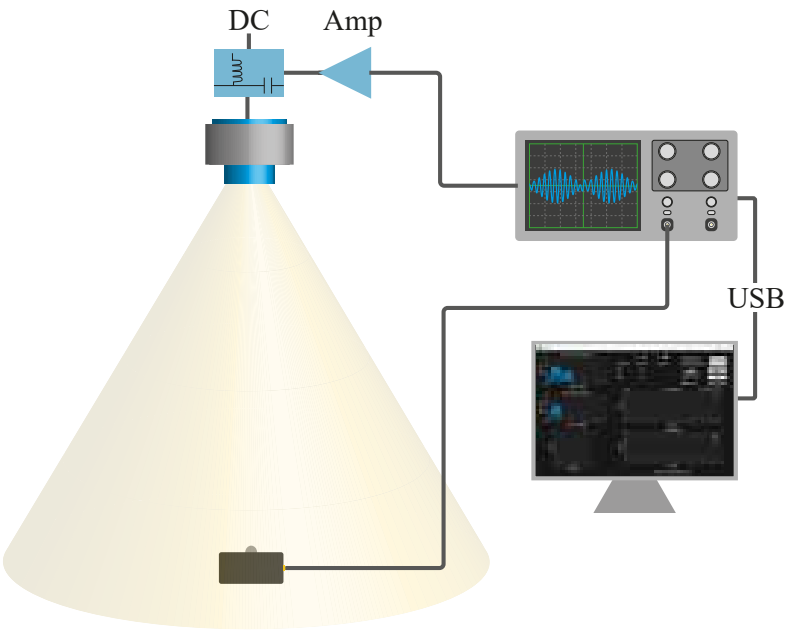

Figure 4.3. Experimental setup of the evaluated SISO system. DC: Direct Current; Amp: Amplifier.

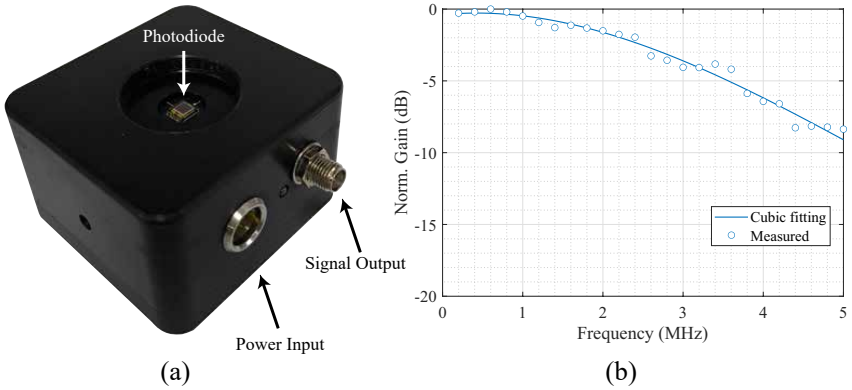

Figure 4.4. (a) Hyperion VLC receiver. (b) The link frequency response.

bias current increased, indicating that the LED did not reach its non-linear operating region.

Despite the FOV limitation for the height of 50 cm, this link shows slight saturation at the midpoint in Figure 4.7 (a), due to increased light reception from the higher AFG output. In Figure 4.7 (b), saturation is also observed along the x-axis coordinates between 0.5 and 1.5. For I_{bias} equal to 300 mA, the 50 cm link exhibits saturation across all FOV points for the same reason. Again, the system performance remains stable when the bias current is increased within the LED linear region. However, compared to $V_{\text{pp}} = 500$ mV, V_{pp} set as 1000 mV improves the overall performance across all cases. For instance, at the height of 150 cm, the EVM decreases from approximately 17% to 8% at the midpoint. Similarly, at the height of 200 cm, the EVM drops from around 25% to 13% at the midpoint. Considering performance under the 4-QAM FEC limit along the trajectory, this configuration is feasible only at 100 cm and 150 cm heights.

As expected, the performance at the height of 50 cm, shown in Figure 4.8, decreases as the saturation increases due to the higher V_{pp}. However, Figure 4.8 also indicates stable perfor-

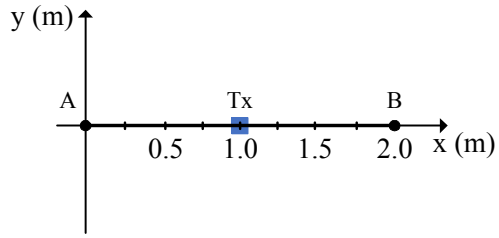

Figure 4.5. 2D schematic view of the experimental scenario.

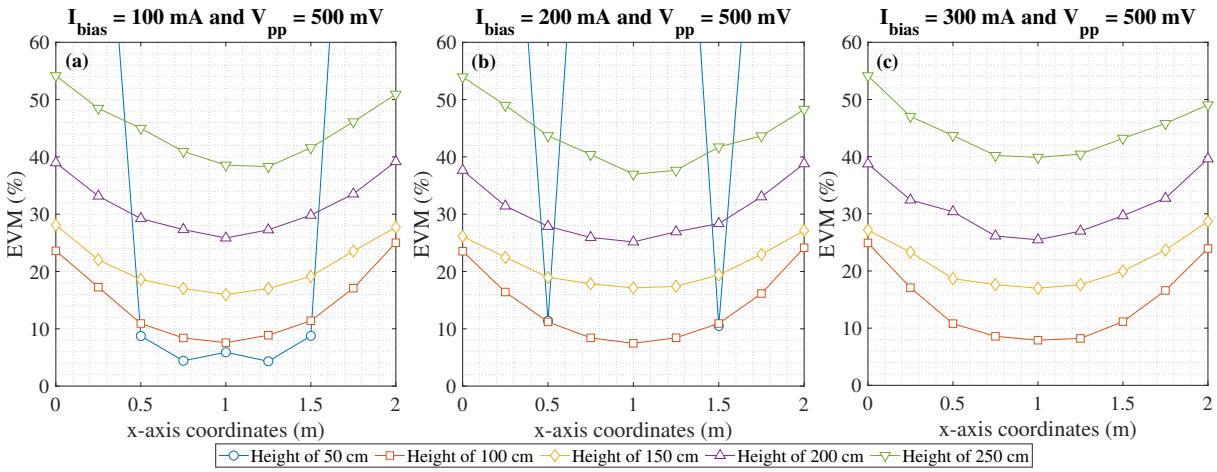

Figure 4.6. Lateral displacement performance evaluation: (a) $I_{\text{bias}} = 100$ mA and $V_{\text{pp}} = 500$ mV; (b) $I_{\text{bias}} = 200$ mA and $V_{\text{pp}} = 500$ mV; (c) $I_{\text{bias}} = 300$ mA and $V_{\text{pp}} = 500$ mV.

mance when the bias current increases. The overall performance improves for the heights of 100, 150, 200, and 250 cm, especially at longer distances. This configuration proved to be a suitable choice, delivering performance below the 4-QAM FEC limit threshold in all cases except for the 50 cm height. Compared to the previous configuration ($V_{\text{pp}} = 1000$ mV), the EVM at the midpoint for 100 cm improved from approximately 4% to 3%, while at 250 cm, EVM dropped significantly from around 20% to 10%.

Figure 4.9 depicts saturation for 50 and 100 cm links as they received more light intensity due to the $V_{\text{pp}} = 3000$ mV. Despite the saturation for 100 cm, it maintained the performance under the FEC limit along the trajectory for all configurations. However, it is not a reliable parametrization for 100 cm height. For heights of 150, 200, and 250 cm, there is a slight performance improvement along the trajectory compared to the previous configuration ($V_{\text{pp}} = 2000$ mV), where the FEC limit was also respected. Additionally, increases in bias current did not enhance the performance of non-saturated links.

As the light intensity increased with the higher $V_{\text{pp}} = 4000$ mV, the performances at the 50 cm and 100 cm link distances declined due to higher saturation, as verified in Figure 4.10. For the other heights, performance remained stable for bias currents of 200 and 300 mA. However, at a bias current of 100 mA, the performances were slightly worse than with 200 or 300 mA, as the higher AFG output (4000 mV) leads the LED to operate in the cutoff region during certain negative peaks of the transmitted signal. Additionally, compared to the $V_{\text{pp}} = 3000$ mV

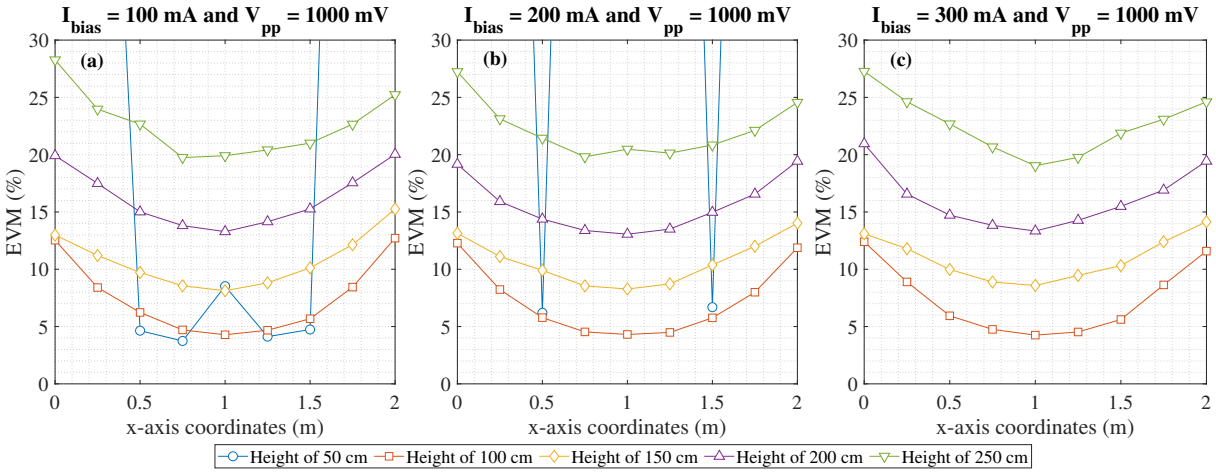

Figure 4.7. Lateral displacement performance evaluation: (a) $I_{\text{bias}} = 100$ mA and $V_{\text{pp}} = 1000$ mV; (b) $I_{\text{bias}} = 200$ mA and $V_{\text{pp}} = 1000$ mV; (c) $I_{\text{bias}} = 300$ mA and $V_{\text{pp}} = 1000$ mV.

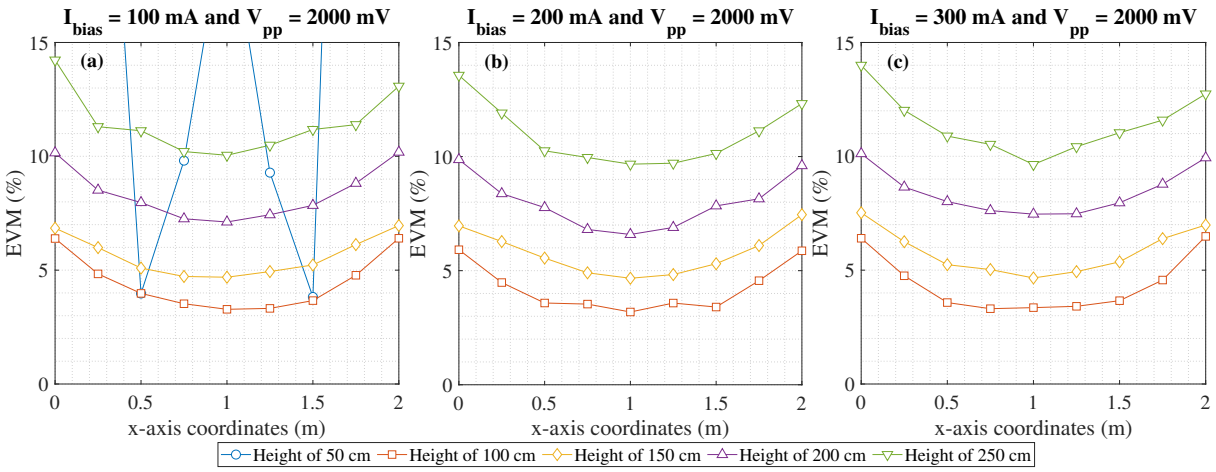

Figure 4.8. Lateral displacement performance evaluation for link distances with the following parameters: (a) $I_{\text{bias}} = 100$ mA and $V_{\text{pp}} = 2000$ mV; (b) $I_{\text{bias}} = 200$ mA and $V_{\text{pp}} = 2000$ mV; (c) $I_{\text{bias}} = 300$ mA and $V_{\text{pp}} = 2000$ mV.

configuration, the setup with $V_{\text{pp}} = 4000$ mV showed a slight overall performance improvement, with EVM decreasing from approximately 7% to 5% at a height of 250 cm.

4.4. Experimental and Simulation Matching

To develop a simulation model of our experimental setup that facilitates future testing of optimizations, modulation schemes, and other improvements, we applied the VLC modeling described in Section 2.1.1, aiming at a match between the experimental and numerical results. To fit the measured LED current-lux curve obtained at 30 cm, shown in Figure 4.2 (c), with the mathematical equation Eq. 2.1, we introduced a gain factor (β) in order to address the high

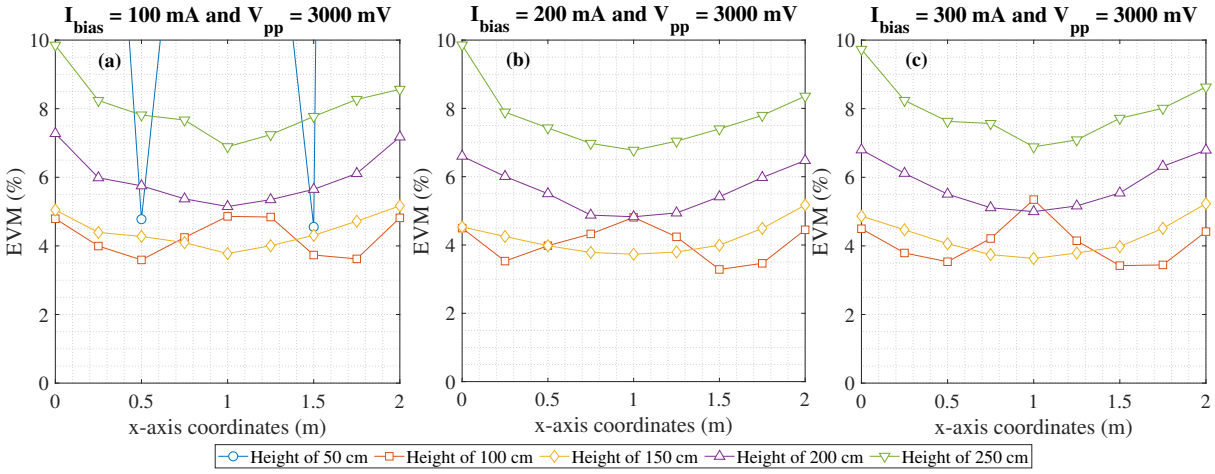

Figure 4.9. Lateral displacement performance evaluation for link distances with the following parameters: (a) $I_{\text{bias}} = 100$ mA and $V_{\text{pp}} = 3000$ mV; (b) $I_{\text{bias}} = 200$ mA and $V_{\text{pp}} = 3000$ mV; (c) $I_{\text{bias}} = 300$ mA and $V_{\text{pp}} = 3000$ mV.

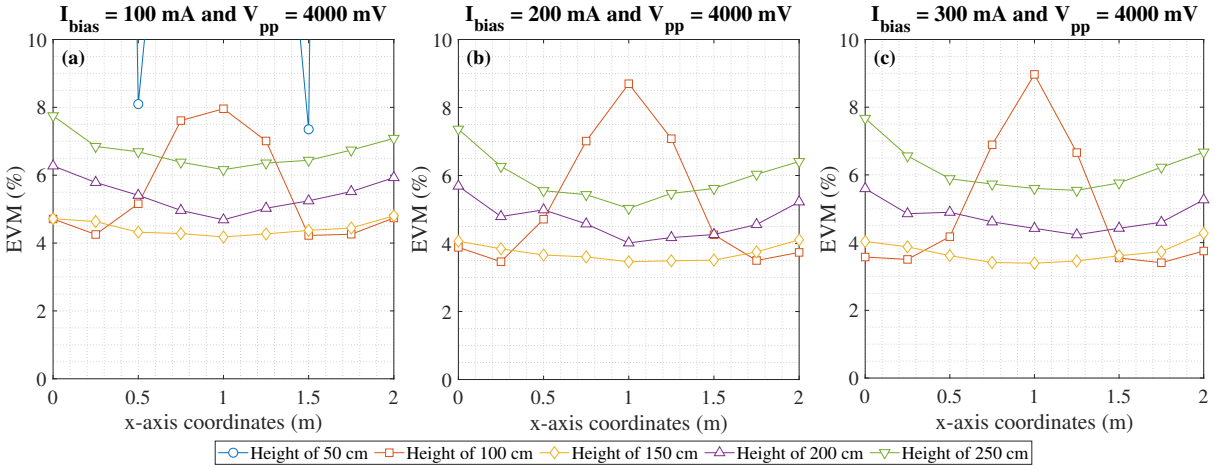

Figure 4.10. Lateral displacement performance evaluation for: (a) $I_{\text{bias}} = 100$ mA and $V_{\text{pp}} = 4000$ mV; (b) $I_{\text{bias}} = 200$ mA and $V_{\text{pp}} = 4000$ mV; (c) $I_{\text{bias}} = 300$ mA and $V_{\text{pp}} = 4000$ mV.

illuminance values in the current-lux curve. The modified equation is as follows:

$$L_{\text{out}}(t) = \beta \frac{I_{\text{in}}(t)}{\left[\zeta + \left(\frac{I_{\text{in}}(t)}{L_{\max}}\right)^{2k}\right]^{\frac{1}{2k}}}, \tag{4.1}$$

where the constants β, ζ, L_{max} and k were set to 8.444, 0.539, 3276, and 0.413, respectively. These values were defined by a curve-fitting process to approximate the set of data points by finding the most suitable parameter values. Figure 4.11 illustrates the matching for a link distance of 30 cm.

Based on the performance evaluation of the setup configurations described in Section 4.3, it can be concluded that the configuration with $I_{\text{bias}} = 100$ mA and $V_{\text{pp}} = 2000$ mV demonstrated performance below the FEC limit for all heights except 50 cm while consuming less power than the other configurations. Therefore, we selected this configuration. Moreover, to estimate the

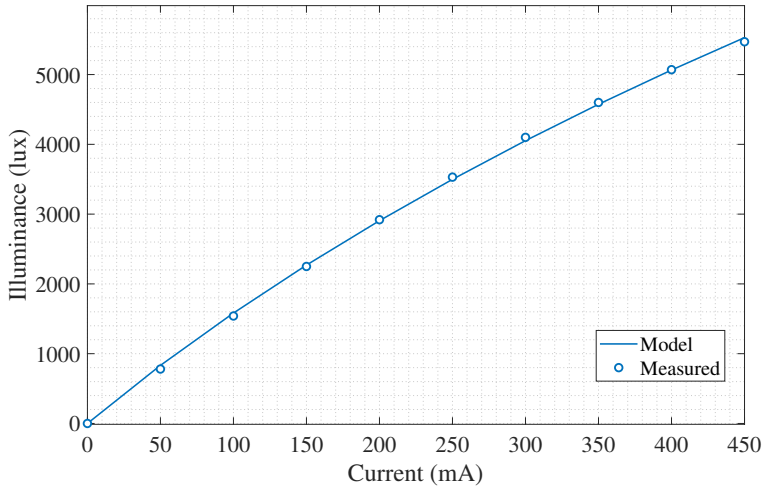

Figure 4.11. Measured current-lux curve for 30 cm and the LED model.

current provided by the communication signal, a sine wave of 1 MHz was generated in the AFG with $V_{\text{pp}} = 2000$ mV, resulting in a peak-to-peak voltage of 3.28 V across the LED, supplied by the amplifier. The current contribution of $V_{\text{led}}(t)$ was then estimated using the curve shown in Figure 4.2 (b). The simulation system's noise level was set to -86 dBm to match the performance of the simulation with that of the experimental setup. This noise level was empirically estimated by selecting the experimental EVM value at the central position for the configuration with $I_{\text{bias}} = 100$ mA, $V_{\text{pp}} = 2000$ mV, and 100 cm height, and replicating this in the simulation environment under equivalent conditions. Thereafter, the simulation noise value was manually chosen to achieve a simulation EVM similar to the experimental EVM. The OFDM parameters described in Section 4.3 were applied to evaluate the SISO and MIMO simulation scenarios. Additionally, the transmitter and receiver simulation parameters were selected from the experimental setup described in Section 4.3. These parameters are summarized in Table 4.1.

Table 4.1. System parameters.

	Parameter	Value
Transmitter	LED semi-angle half power ($\Phi_{1/2}$)	60 Degree
	LED bias current (I_{bias})	100 mA
	AFG output (V_{pp})	2000 mV
Receiver	Optical filter gain (T_{s})	1
	PD responsivity (R)	0.6 A/W
	PD area (A_{r})	2.5×10^{-5} m^2
	PD field of view (Ψ_{c})	60 Degree

4.4.1. Evaluated SISO VLC System

The SISO simulation system follows equations described in Section 2.1.1 as well as the setup characteristics illustrated in Figure 4.3 and 4.5. Performance results for the experimental and

simulation scenarios are shown in Figure 4.12. Heights of 100, 150, 200, and 250 cm achieved RMSE values of 0.22%, 0.36%, 1.09%, and 1.43%, respectively. These errors are attributed to the non-linear characteristics of communication systems, such as link frequency response, which were not implemented in the simulation for simplicity. However, as the simulation environment produced small and satisfactory errors compared with the experimental setup, the simulation model effectively replicates a real VLC system. It is also observed that RMSE increases with height, with the lowest error at 100 cm, since noise calibration was performed at this height.

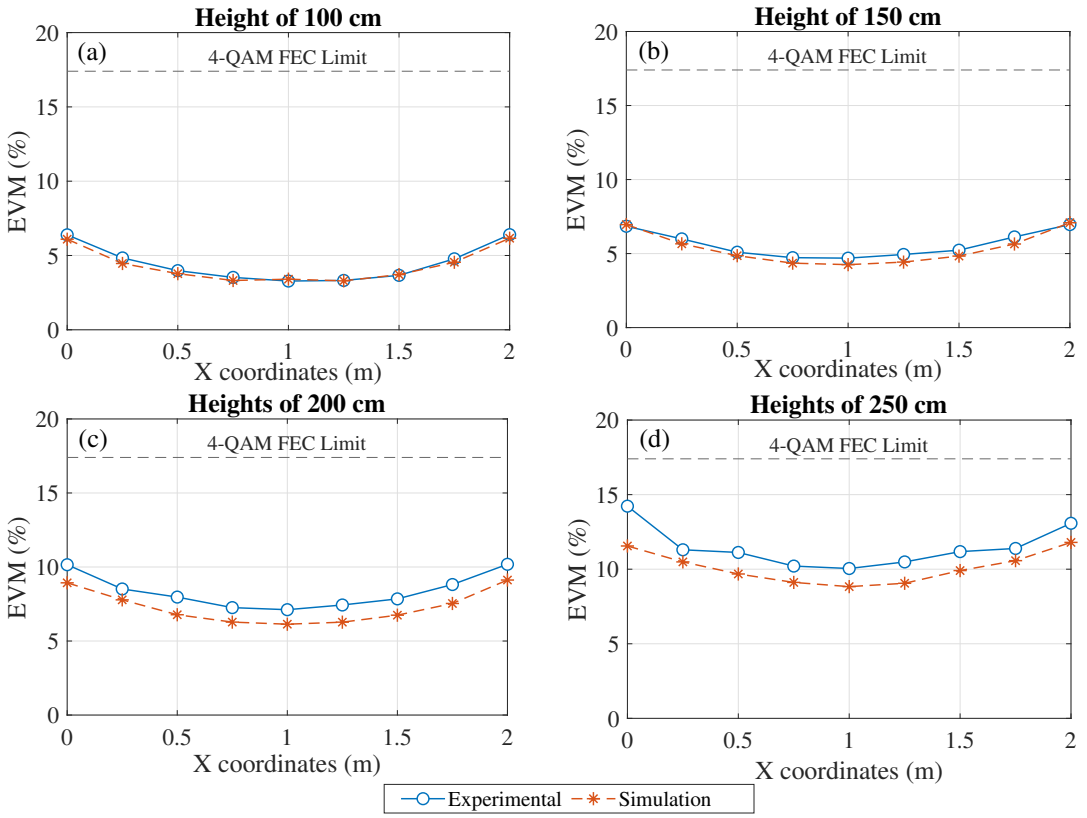

Figure 4.12. Experimental and simulation performance evaluations for the SISO systems at heights of: (a) 100, (b) 150, (c) 200, and (d) 250 cm.

4.4.2. Evaluated MISO VLC System

For the MISO system configuration, we implemented a setup with two transmitters, as illustrated in Figure 4.13 (a) and (b). The test trajectory follows the same path as in the SISO setup; however, with the transmitters positioned as shown in Figure 4.13 (c). For this scenario, we applied a frequency diversity approach, sending the same signal from both transmitters using different central frequencies. We used the same OFDM parametrization of SISO; however, setting the central frequencies equal to 0.75 and 1.75 MHz for Tx1 and Tx2, respectively. Considering the frequency response illustrated in Figure 4.4, Tx2 will experience more attenuation than Tx1. Therefore, we set a higher AFG output ($V_{\text{pp}} = 3100$ mV) for Tx2 to achieve an

equivalent performance at the midpoint ($x = 1$) with the height of 150 cm. For Tx1, the V_{pp} was set as 2000 mV as in SISO, and both transmitter's bias currents were set as 100 mA.

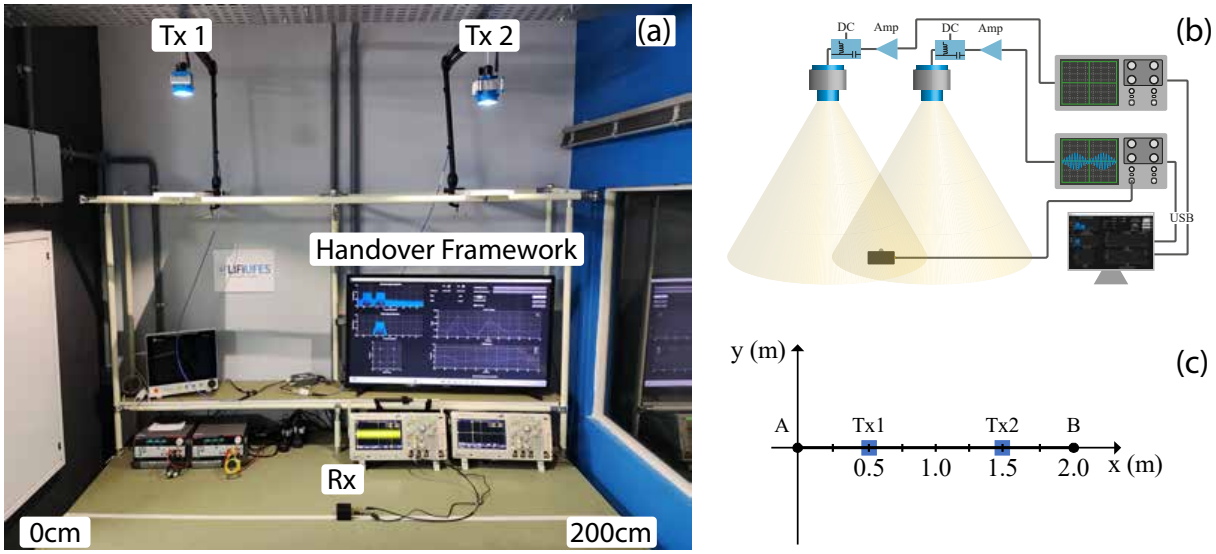

Figure 4.13. Experimental setup of the evaluated SISO system. DC: Direct Current; Amp: Amplifier. (a) setup picture; (b) configuration diagram; and (c) 2D evaluation scenario.

Figure 4.14 illustrates the performance comparisons of the MISO systems at heights of 100, 150, 200, and 250 cm. At 100 cm, the receiver experienced greater horizontal distances than in the SISO scenario, receiving poor signals in points outside the FOV that degrade the performance, resulting in RMSEs of 37.63% and 34.09% for Tx1 and Tx2, respectively, when comparing experimental with simulation results. For a height of 150 cm, where all trajectory points remained within the FOV, lower RMSEs of 1.37% and 1.65% were achieved by Tx1 and Tx2, respectively. At 200 cm, Tx1 and Tx2 presented RMSEs of 2.72% and 4.32%, and at 250 cm, they achieved RMSEs of 3.24% and 5.09%, respectively. Excepting 100 cm, the simulation demonstrated satisfactory RMSEs, particularly at 150 cm, thus supporting the model's applicability.

Compared to the SISO scenario, this setup exhibited higher RMSEs due to the receiver's increased horizontal displacement. Additionally, interference between transmitters further contributed to these RMSE values. In general, Tx2 exhibited higher EVM and RMSE than Tx1 due to its central frequency, which falls within a non-linear region of the link's frequency response (see Figure 4.4).

4.5. Conclusions

This Chapter evaluated the impact of bias current and communication signal amplitude on the performance of a SISO setup. Additionally, a simulation model matching with a SISO and MISO setup was also exploited. From the obtained results, we could conclude that, when the communication signal operates within the linear region and the receiver remains unsaturated, the

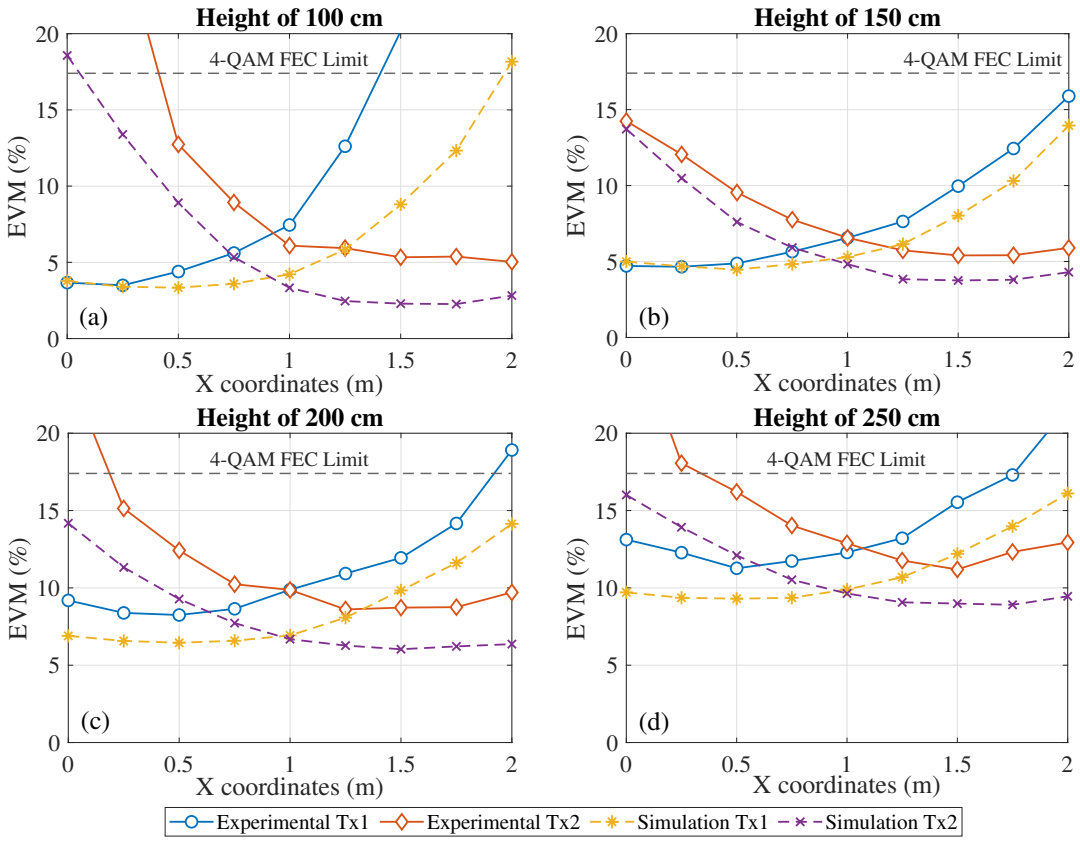

Figure 4.14. MISO performance comparison for links of: (a) 100, (b) 150, (c) 200, and (d) 250 cm.

bias current (I_{bias}) has minimal impact on system performance. However, a low bias current can lead part of the communication signal into the LED cutoff region, while a high bias current may cause receiver saturation and lead the signal to the non-linear region, degrading performance. The amplitude of the communication signal (V_{pp}) also affects saturation and linearity; however, higher amplitudes generally improve performance when the system operates unsaturated and in the linear range. Therefore, optimal performance requires jointly tuning V_{pp} and I_{bias} rather than adjusting them independently. Disregarding the height of 50 cm, the optimal EVM within the FEC limit across the trajectory was achieved with $V_{\text{pp}} = 2000$ mV and a bias current of 100, 200, or 300 mA. The bias current choice could balance energy savings (100 mA) and higher ambient illumination (300 mA).

The simulation model demonstrated satisfactory approximation with the real setup. For the SISO configuration, the RMSE of the simulation model compared to the experimental EVM was 0.22%, 0.36%, 1.09%, and 1.43% at heights of 100, 150, 200, and 250 cm, respectively. At a height of 100 cm in the MISO setup, RMSE values for Tx1 and Tx2 were higher at 37.63% and 34.09% due to partial trajectory loss outside the FOV. However, across the entire trajectory, it is possible to maintain performance under the FEC limit with at least one transmitter, highlighting the necessity of a handover mechanism. The lowest MISO RMSE values occurred at 150 cm, with Tx1 and Tx2 errors of 1.37% and 1.65%, respectively. At 200 cm and 250 cm, Tx1 had RMSEs of 2.72%, 4.32% and Tx2 achieved 3.24%, and 5.09%, respectively. These low RMSE

values affirm the simulation model's reliability, suggesting it as a robust tool for testing new algorithms, optimization techniques, modulation schemes, and educational applications.

CHAPTER 5.

AI-Driven Enhancements for Handover in Visible Light Communication Systems

5.1. Introduction

AI techniques have demonstrated considerable potential for handover improvements in VLC applications. This potential was exemplified in the studies conducted by Wu et al. [141] and Wang et al. [142], in which Reinforcement Learning (RL) was applied to optimize handovers in a hybrid, or Heterogeneous Network (HetNet), with optical and RF links, minimizing overall latency while maintaining a target throughput. Additionally, Wu et al. [141] implemented a RNN based on LSTM to predict outage events and enhance the RL algorithm's performance. More recently, the authors of [143] described a classification model used to predict the type of user's trajectory and assist a reinforcement learning model to make handover decisions that can dynamically adapt to new network conditions.

A handover scheme for HetNet was presented in [144], considering a coefficient that defines the selection preference between Light Fidelity (LiFi) and wireless fidelity WiFi. The Authors implemented a machine learning algorithm to define the coefficient based on the user's speed, the distance between the two nearest LiFi APs, the height of LiFi APs, and the number of LiFi APs per WiFi access point. Ma et al. [145] developed a neural network-based handover scheme that uses channel quality, user movement, and device orientation to classify the moment of handover between LiFi and WiFi. It is worth commenting that the above-commented works do not employ optimization algorithms adapted to specific problem requirements alongside time series ML classifiers to minimize handovers, which is one of the focuses of this thesis.

As frequent handovers can significantly impact the performance of mobile VLC links, this Chapter's contribution relies on the investigation of a Modified Genetic Algorithm (MGA) approach combining time series ML classifiers to minimize the number of handovers. The approach is based on a Digital Twin (DT) VLC system, which has been validated in our previous studies [44] and [45]. The performance of the proposed handover scheme was evaluated in a simulated environment comprising 18 APs and a single mobile receiver. Moreover, the proposed scheme increases the overall performance of the system by considering the receiver trajectories and FEC limit to minimize the number of handovers. More specifically, the contributions of this Chapter are described as follows:

- formulation of a handover optimization problem and application of a modified GA for the demanded specifications;
- application of time series ML classifiers for predicting the endpoint of the mobile receiver based on its trajectory;
- a further analysis on the impact of overlapping trajectories in endpoint forecasting;
- evaluation of the performance of the proposed handover scheme, comparing results with a power-based scheme.

The remainder of this Chapter is structured as follows. Experimental platforms are presented in Section 5.2. Section 5.3 describes the handover simulation environment applied in this Chapter. The handover optimization procedure is presented in Section 5.4. The data processing and machine learning algorithms are detailed in Section 5.5 and 5.6, respectively. The results and discussions are presented in Section 5.7. Finally, the conclusion remarks are provided in Section 5.8.

5.2. Experimental Platforms for Digital Twin and Handover Evaluations

5.2.1. The Validated VLC Digital Twin: Preliminary Results

A DT is a virtual representation of a physical entity, system, or process that is capable of combining real-time data with computer models to simulate and analyze the physical entity in a virtual environment [146]. The development of the VLC digital twin used as a basis in this work was divided into three parts, according to concepts presented in [147]: the modeling of the SISO VLC setup components, the tuning of its parameters according to manufacturer datasheet or characterizations, and the validation of the overall model according to the experiment. Accordingly, experiments in a real setup (physical asset) were conducted to provide the input data to predict performance over different configurations, as reported in [44] and [45].

Figure 4, described in [45], depicts the experimental setup used to evaluate performances. As a physical object, it allows bias current tuning to assure LED operation in the linear region of the electric-optical conversion. An AFG was employed to deliver the 5 MHz modulating electrical signals, configured according to the 5G NR recommendations [139]. The discrepancy between the performances was determined by the RMSE in order to identify an optimum noise power, i.e., the minimum value of RMSE. After the calibration, the noise power for the DT was set to $N = -165$ dBm for the minimal RMSE of 0.70% (see Figure 5.1 (a)). Further details of the experimental proof-of-concept can be found in Section II-B of [45]. Figure 5.1 shows the performance assurance between the experimental and the simulation results for various link lengths and bias currents. The simulation results were obtained with the simulator illustrated in Figure 2 of [45] implemented using Matlab. The linear optic-electrical conversion region was

considered in order to establish a simulation model of the setup denominated as digital twin in [45]. The low RMSE shown in Figure 5.1 validated the DT.

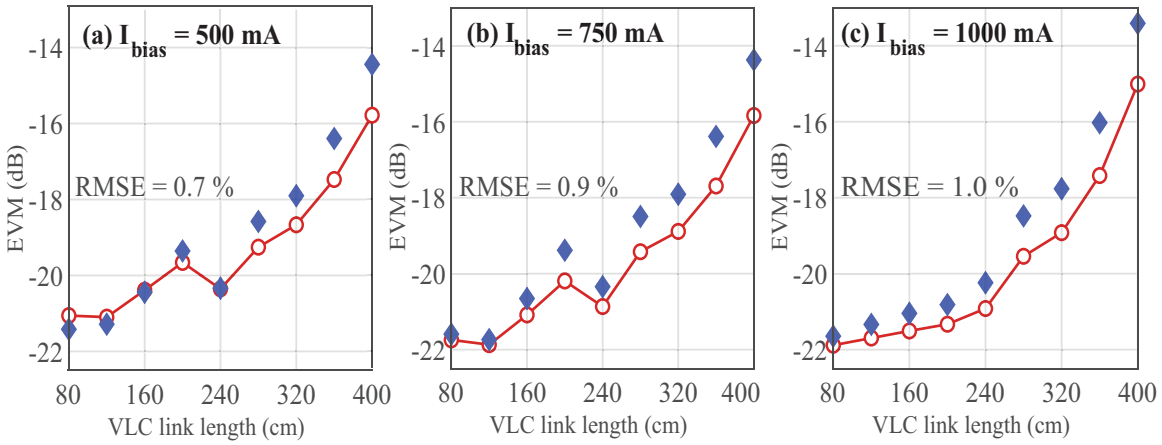

Figure 5.1. Error vector magnitude metric [1] for the experimental (blue diamonds) and simulation model (red circles).

5.2.2. Experimental Setups for Handover Validation

To demonstrate the feasibility of the handover procedure proposed in this Chapter, we designed the experimental apparatus depicted in Figure 5.2 (a) and Figure 5.3 (a). The main objective was to evaluate the performance of a handover strategy based on frequency diversity. The physical assets depicted in Figure 5.2 (a) and Figure 5.3 (a) consist of three and four VLC transmitters, respectively, positioned at a height of 1.5 m from the mobile receiver. The analog signals available at the AFG outputs were amplified and superimposed onto bias currents, aiming to provide non-negative waveforms as illustrated in Figure 5.2 (b) and Figure 5.3 (b). Each transmitter was equipped with a CREE CXA1507 white CoB LED as described in Section 4.2. With the Hyperion LiFi receiver [140], we measured the frequency responses shown in Figure 5.4 and 5.5 for both setup scenarios.

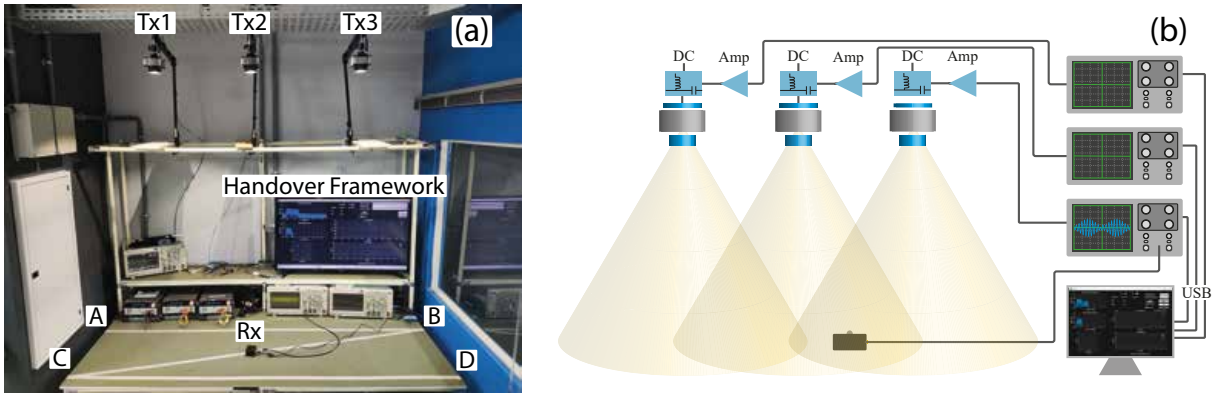

Figure 5.2. (a) Handover frequency diversity setup with three transmitters and (b) its block diagram.

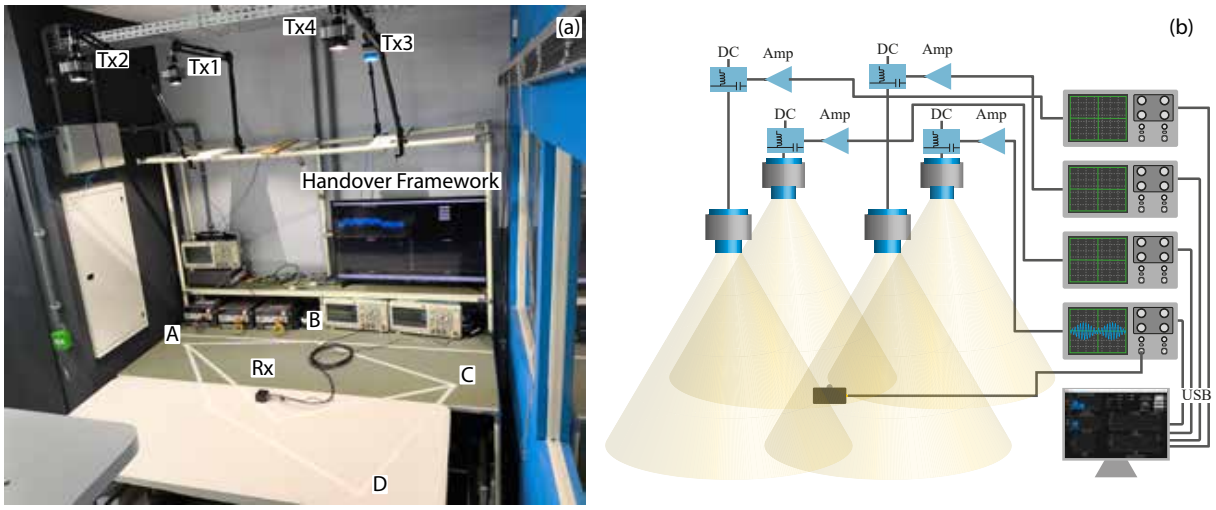

Figure 5.3. (a) Handover frequency diversity setup with four transmitters and (b) its block diagram.

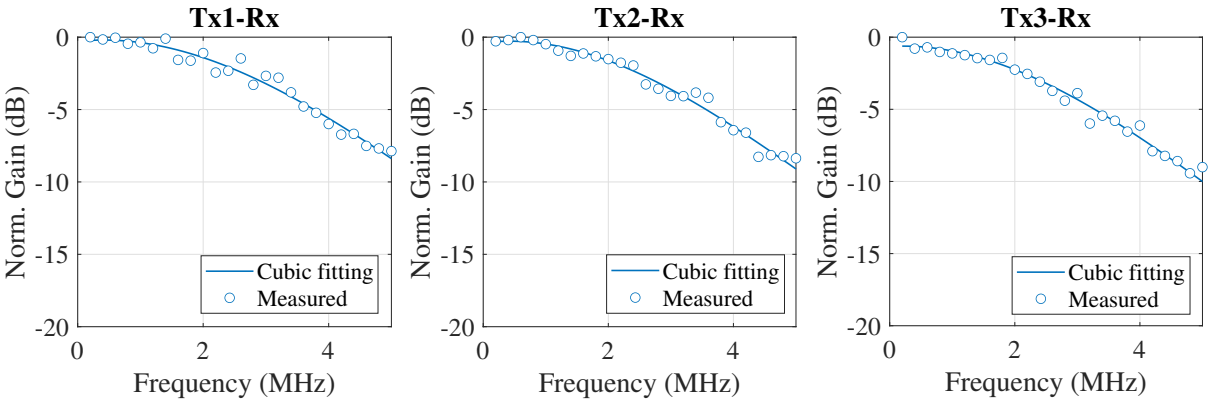

Figure 5.4. Frequency responses of the three-transmitters scenario links.

The frequency diversity was exploited by transmitting the same 5G NR signal (1 MHz of bandwidth) in central frequencies equal to 0.75, 1.50, 2.25, and 3.00 MHz for Tx1, Tx2, Tx3, and Tx4, respectively, across both scenarios. To address the increased attenuation observed in links Tx2-Rx, Tx3-Rx, and Tx4-Rx due to their respective higher central frequencies, we adjusted the output amplitude (V_{pp}) of the AFG for each link, providing additional power to the links with greater attenuation. In the three-transmitter setup, we configured I_{bias} at 100 mA for Tx1, Tx2, and Tx3, with V_{pp} values set at 0.85 V, 1.10 V, and 1.22 V, respectively. In the four-transmitter scenario, V_{pp} for Tx1, Tx2, Tx3, and Tx4 was set at 0.70 V, 1.30 V, 2.20 V, and 3.50 V, respectively. As indicated in Section 4.3, Tx4's higher V_{pp} required an increased bias current, which we set to 200 mA for all transmitters of this scenario to enable a fair comparison.

It is important to mention that these parameters were not selected to maximize performance, as a single transmitter would be enough to cover our limited physical areas without the need for handovers. Instead, the parameter values were empirically chosen to limit coverage to specific areas, creating the need for handovers within our test environment.

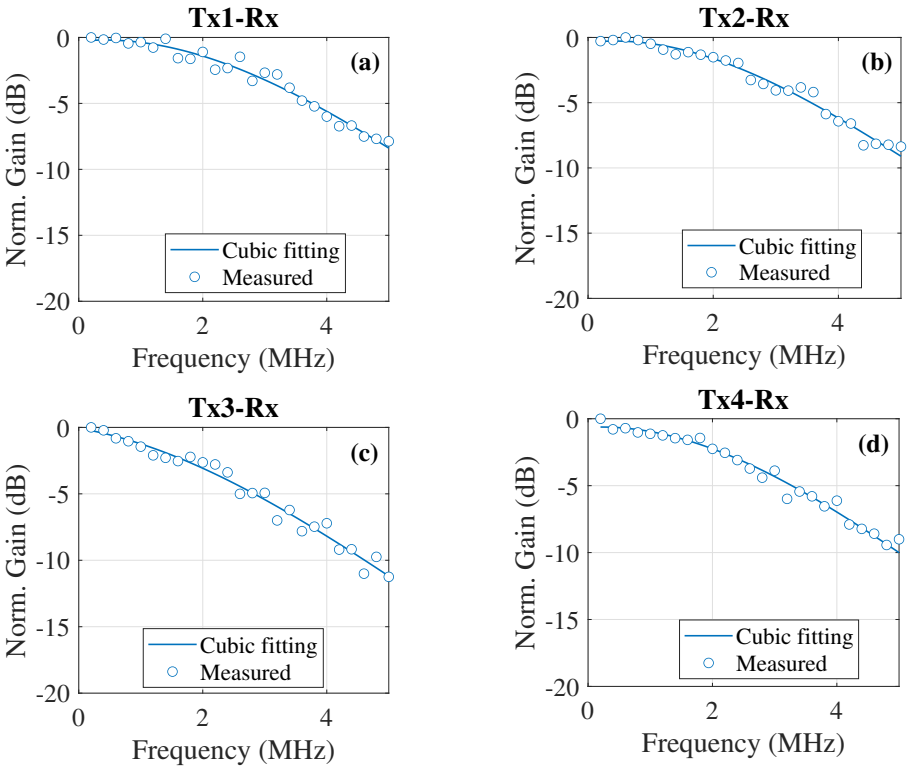

Figure 5.5. Frequency responses of the four-transmitters scenario links.

5.3. Handover Simulation Environment

In this thesis, we present an extension of the previous work, described in Section 5.2.1, from the SISO DT system to a MISO simulation system implemented using Matlab and the VLC analytical model described in Section 2.1.1. The goal of this extension is to enable the assessment of handover schemes. The new scenario was inspired by a real research laboratory where some trajectories share part of the path.

This scenario was inspired by our research laboratory illustrated in Figure 5.6, comprising 18 APs, equally spaced by 2 m, and a receiver located at a height of 2 m from the AP. Figure 5.7 depicts a 2-dimensional (2D) representation of the scenario illustrating the coverage area of the APs. Considering a height of 2 meters and a FOV $\Psi_c = 60°$, each AP has a coverage radius of approximately 2.38 meters. Additionally, the figure shows the trajectories that the receiver follows to accomplish its tasks in the scenario, which includes four Workstations (WS). As the representation of a trajectory is a spatio-temporal simulation problem, data for each trajectory was generated based on a 2D plane with a sampling rate of 75 samples per second. A summary of the system parameters can be found in Table 5.1.

Figure 5.8 presents the block diagram of the simulation setup implemented to evaluate the performance of the proposed handover scheme, where the block Control Unit executes AI algorithms to trigger the handovers. The NR signals are composed of 42 data subcarriers multiplexed by a fast Fourier transform of 128 samples, considering 4-QAM as subcarrier mapping.

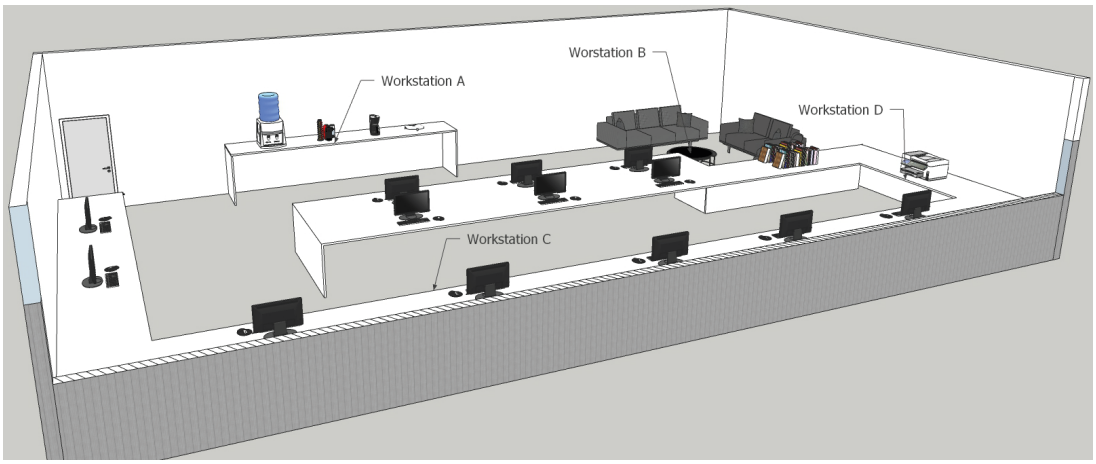

Figure 5.6. 3D model of our Research laboratory.

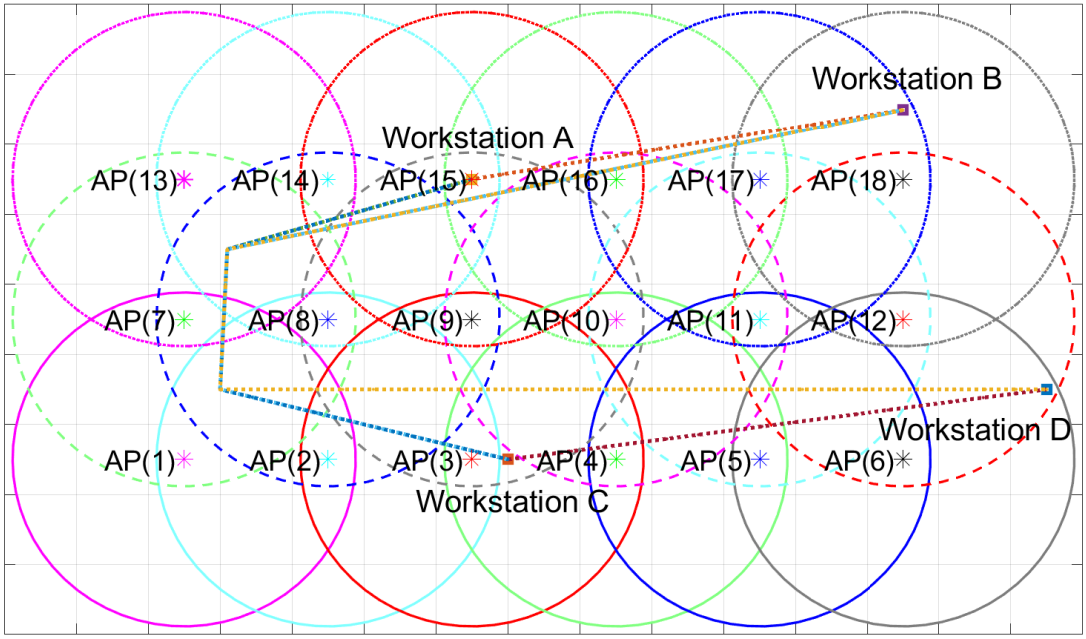

Figure 5.7. 2D simulation scenario, comprising 18 access points with their coverage, four workstations, and the trajectories between them.

Thus, for the subcarrier spacing of 15 kHz, the bandwidth (B_{W}) is approximately 2 MHz. To implement a front-end frequency domain multiplexing, the carrier frequency of each AP was spaced in 5 MHz intervals, starting from 3 MHz. Therefore, the carrier frequencies for the APs are denoted as $[f_{\mathrm{c}_1}, f_{\mathrm{c}_2}, f_{\mathrm{c}_3}, \cdots, f_{\mathrm{c}_{18}}] = [3, 8, 13, \cdots, 88]$ MHz. In order to avoid intersymbol interference, a cyclic prefix of 16 samples was added to the beginning of each NR signal. Furthermore, the experimental setup adopts a noise model based on the Signal-to-noise Ratio (SNR) methodology presented in [44], as well as the noise power level specified in Section 5.2.1.

Handover decisions based solely on power margin may cause ping-pong effects, a phenomenon where frequent handovers occur between two APs. To mitigate this effect, the Standard Handover Scheme (STD) implemented in LTE [148] can be used. The STD triggers a handover decision when the power of the target AP (P_{target}) exceeds the power of the host AP

Table 5.1. System parameters.

	Parameter	Value
Transmitter	LED semi-angle half power ($\Phi_{1/2}$)	70 Degree
	LED bias current (I_{bias})	500 mA
	Optical Modulation Index (OMI)	0.5
Receiver	Optical filter gain (T_{s})	1
	PD responsivity (R)	0.6 A/W
	PD area (A_{r})	0.0001 m^2
	PD field of view (Ψ_{c})	50 Degree
System	Number of receivers	1
	Speed of receivers	$[1, 2, 3, 4, 5]$ m/s
	Number of APs	18
	Distance between APs	2 m
	Height between an AP and the receiver	2 m

(P_{host}) for a period of Time to Trigger (TTT). The STD employs a timer that starts when $P_{\text{target}} > P_{\text{host}} + \delta_{\text{HOM}}$ is satisfied, where δ_{HOM} represents the handover power margin. The timer continues computing as long as the inequality is satisfied, otherwise, the timer is reset. Once the timer reaches TTT, the handover occurs to transfer the receiver from the host to the target AP as described in Figure 5.9. In this Chapter, we followed the parametrization described in [30], where TTT and δ_{HOM} were set to be 160 ms and 1 dB, respectively.

5.4. The Handover Optimization Procedure

5.4.1. Problem Formulation, Chromosome Representation and Fitness Function

As frequent handovers can negatively impact system connectivity, we applied a GA to minimize the number of handovers in the trajectories depicted in Figure 5.7. The GA, described in Section 2.3.1, will minimize the handovers for all trajectories, considering the EVM performances of all APs in each position of a trajectory. Afterward, considering the time consumed by the optimization process, the optimized data will be saved in a database, aiming at quick data access. Thus, knowing the current position of the receiver and its trajectory, it is possible to select, from the database, the AP it should connect.

The optimization algorithm considers one trajectory at a time, where the chromosome data structure containing the handover information, with a didactic example, is defined as follows:

$$S = \begin{pmatrix} \text{Trajectory Positions} \\ \text{AP Indexes} \end{pmatrix} = \begin{pmatrix} 1 & 50 & 68 \\ 2 & 5 & 8 \end{pmatrix}.$$

As described in Section 5.3, trajectory data is represented by a 2D discrete array of coordi-

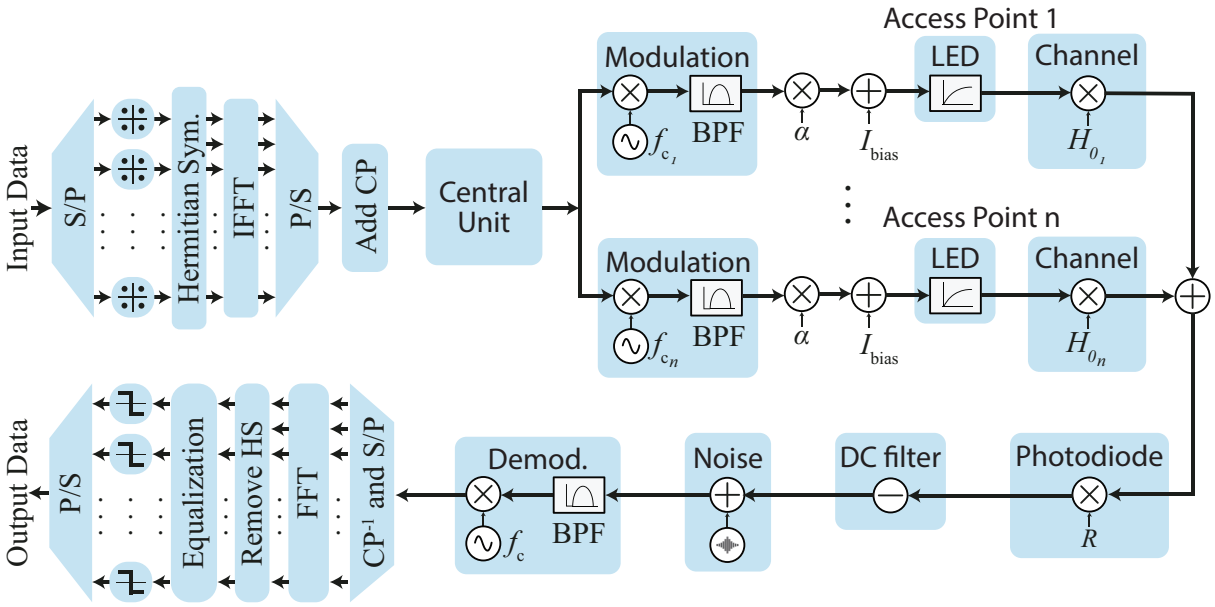

Figure 5.8. Block diagram of the OFDM-based VLC system.

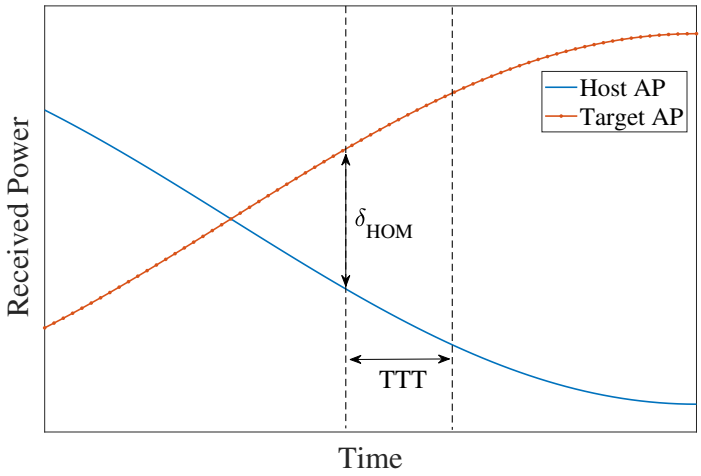

Figure 5.9. The STD handover scheme.

nate tuples, where position information can be accessed using an index. The chromosome's first row contains the indexes of the trajectory where the host connections begin, while the second row represents the AP host indexes defined in Figure 5.7. In the didactic example above, the receiver starts at position 1 of the trajectory, connecting with AP 2. At position 50, a handover occurs from AP 2 to 5, followed by another handover from AP 5 to 8 at position 68.

The chromosome's size is modeled based on the number of handovers that occur in the STD scheme. We assume that the GA cannot have more handovers than the STD, and therefore, we use a fixed-size approach to simplify the GA implementation. The example below illustrates how the GA can reduce the number of handovers in this data structure, using the optimization of the previous example S.

$$S_{\text{optimized}} = \begin{pmatrix} 1 & 64 & 78 \\ 2 & 6 & 6 \end{pmatrix}$$

Here, the receiver starts connecting with AP 2 and then changes to AP 6 at position 64. At position 78, the AP index remains the same as the previous position, which is not counted as an exchange. Thus, the GA reduced one handover in this trajectory. The total number of handovers (N_{HO}) of a chromosome along a trajectory is calculated by

$$N_{\mathrm{HO}} = \sum_{n=1}^{N-1} f(S(2,n), S(2,n+1)), \tag{5.1}$$

where S is a chromosome, N is the number of columns of S, and f is defined as:

$$f(x_1, x_2) = \begin{cases} 1, & \text{if } x_1 \neq x_2 \\ 0, & \text{if } x_1 = x_2 \end{cases} \tag{5.2}$$

In this optimization process, both the number of handovers and the system's performance are crucial factors. Therefore, to consider system performance on the fitness evaluation, a penalty factor (α_{p}) was defined to sum 1000 for each position of the trajectory where the EVM exceeds the 4-QAM FEC threshold. The penalty is represented as follows:

$$\alpha_{\mathrm{p}} = \sum_{n=1}^{M} C(EVM(n)) \times 1000, \tag{5.3}$$

where M denotes the total number of positions in the trajectory, $EVM(n)$ is the EVM at the n-th position of the trajectory, and

$$C(\mathrm{EVM}(n)) = \begin{cases} 1, & \text{if } \mathrm{EVM}(n) > 17.4\% \\ 0, & \text{otherwise.} \end{cases} \tag{5.4}$$

Therefore, the objective is to minimize the fitness function expressed by

$$FF = N_{\mathrm{HO}} + \alpha_{\mathrm{p}}. \tag{5.5}$$

Thus, a chromosome with 1 handover and 5 trajectory positions with EVMs above the FEC limit results in a fitness value of 5001, according to Eq. (5.5) and using the penalty provided by Eq. (5.3). However, a chromosome with 3 handovers and all positions with EVMs under the FEC limit will probably be selected to compose the next generation due to a fitness value equal to 3, despite the highest number of handovers.

5.4.2. Evolution Procedure of the Applied GA

The roulette wheel selection strategy was chosen for this optimization, which associates a probability of selection with the fitness level. In this case, the probability of an individual

being chosen is greater if its fitness level is smaller. Following selection, the crossover operator generates offspring by combining the genes of different individuals. The crossover operator utilized in this study is based on the single-point crossover strategy, where a crossover point is randomly chosen and the submatrices are exchanged, as shown in Figure 5.10. It is noteworthy that one of the offspring chromosomes is not sorted by trajectory position. The GA implemented in this study utilizes unsorted chromosomes to facilitate the crossover and mutation process. However, the fitness process sorts the chromosome before its evaluation to apply Eq. 5.1.

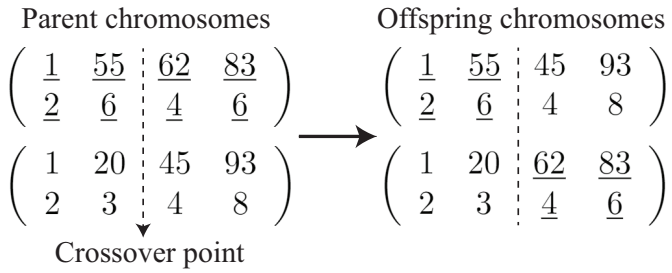

Figure 5.10. Single-point crossover strategy exemplification.

In this Chapter, the conventional GA mutation process was modified to enhance the optimization results for the problem described above. For the chromosome structure presented, the conventional mutation randomly selects one of the columns and changes its values randomly within the allowed range of each variable. In the modified mutation proposed, we also randomly choose one column and a position in the allowed range. However, the AP index is set to the value of the previous AP, which reduces the number of handovers as the AP index is repeated. The new mutation procedure is described in Algorithm 5.1, where $varMax$ and $varMin$ represent the range within which a position can be defined, MS is the mutated chromosome, and μ is the mutation rate.

Algorithm 5.1. Modified mutation procedure

Input: $S, varMax, varMin, \mu$
Output: MS
1: $colSize \leftarrow size(S)$
2: $nMutations \leftarrow ceil(colSize * \mu)$
3: $MS \leftarrow S$
4: **while** $nMutations > 0$ **do**
5: $\quad i \leftarrow randInt(2, colSize)$
6: $\quad MS(1, i) \leftarrow randInt(min, max)$
7: $\quad MS(2, i) \leftarrow MS(2, i-1)$
8: $\quad nMutation \leftarrow nMutation - 1$
9: **end while**
10: **return** MS

Due to differences with conventional GA, we denominated the proposed heuristic as a MGA. The MGA parameter settings for the population size and number of iterations were specified as 150 and 500, respectively. The mutation rate, defined as the probability that any given gene

in an individual will undergo mutation, was set to 0.02. The mutation percentage was set to 0.5, which indicates the proportion of individuals in the population subjected to mutation in each generation. Additionally, the crossover percentage, representing the proportion of the population selected for crossover operations during reproduction, was set to 0.8.

5.5. Data Description and Processing

While real-time orchestration of handover executions is crucial for supporting mobility in VLC, the previously described optimization process does not provide real-time output, incurring in significant delays that are not feasible in practical applications. However, after the training phase that needs to be done offline and only once, ML algorithms can generate predictions with minimal latency. Therefore, we propose a real-time system that combines handover data obtained from the MGA optimization with ML predictions of the receiver's next workstation in order to create handover decisions.

5.5.1. Modeling the Positioning Error

It is important to mention that, in this work, we assume the existence of a previously implemented localization system, where the positions are given by the simulation environment when the receiver moves. However, aiming at testing the robustness of the AI models, we applied errors in the receiver position following an approximation of the errors described in [2]. The authors of [2] reported a mean accuracy of 0.023 m with a 95th Percentile (P95) equal to 0.035 m. Additionally, the error described by the authors considers the Euclidean distance between real and estimated positions. However, this approach does not estimate errors for x and y individually, and it loses the direction of the error vectors. Thus, based on the paper's statistics, we create an approximation to generate random errors. First, for both x and y, we consider a normal distribution with mean (μ) equal to zero to generate positive and negative values, creating errors in all 2D directions. Moreover, the standard deviation (σ) was estimated considering that the P95 of a normal distribution is between -1.96σ and 1.96σ. Thus, we considered $1.96\sigma = 0.035$, i.e. $\sigma \approx 0.018$. The normal distribution considering $\mu = 0$ and $\sigma \approx 0.018$ are shown in Figure 5.11 (a).

Figure 5.11 (b) shows the Cumulative Distribution Function (CDF) considering Euclidean distance errors of our approximation and the CDF described in [2]. The mean, the standard deviation, and the P95 of our approximation were 0.023, 0.012, and 0.043, respectively, showing a good approximation with the results obtained in [2].

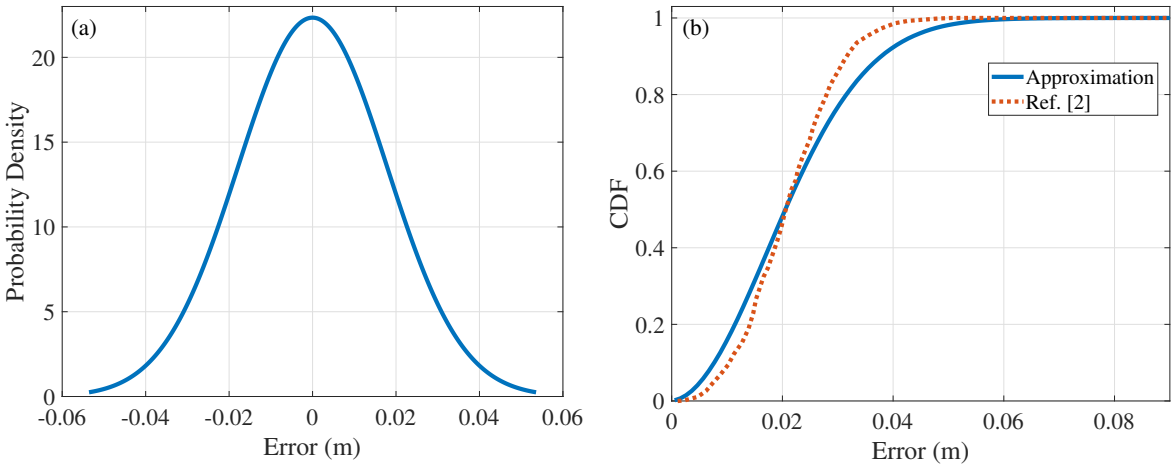

Figure 5.11. Error modeling: (a) normal distribution for our error approximation. (b) CDF of our approximation and reference [2].

5.5.2. Problem Modeling and Real-time Handover System

Data produced by the MGA optimization can inform where the handover should be done by analyzing the position of the receiver. However, it is also necessary to know which trajectory the receiver is following, as the optimization was done based on the trajectories. The departure workstation can be estimated when the receiver starts to move, however, the destination should be predicted as the handover system does not know this information in advance. To address this, we applied ML to predict the receiver's next WS based on the following inputs:

i. the last coordinates $[(x, y)_0, (x, y)_1, \cdots, (x, y)_n]$ of the receiver given by the simulation scenario;

ii. receiver's speed *;

iii. last WS, which is transformed into a binary representation by the one-hot encoder.

The first block of Figure 5.12 shows the inputs of the ML models detailed in Section 5.6. The length of the input coordinates time series is defined according to the hyperparameter optimization of each model. The model output is also one-hot encoded because the formulation was modeled as a time-series classification problem. After the employment of the ML problem, the last block uses the predicted WS, the last WS, the current position $[(x, y)_0]$, and the MGA data (MGAD) to select which AP the receiver should be connected.

In some instances, the model's prediction might be inaccurate or unrealistic for the current problem modeling. For example, if the receiver's last WS was 3 and the model predicts its next WS as 3 again. The handover system bypasses this scenario by applying the STD algorithm.

*This information can be provided by the mobile receiver in, for example, a wireless uplink.

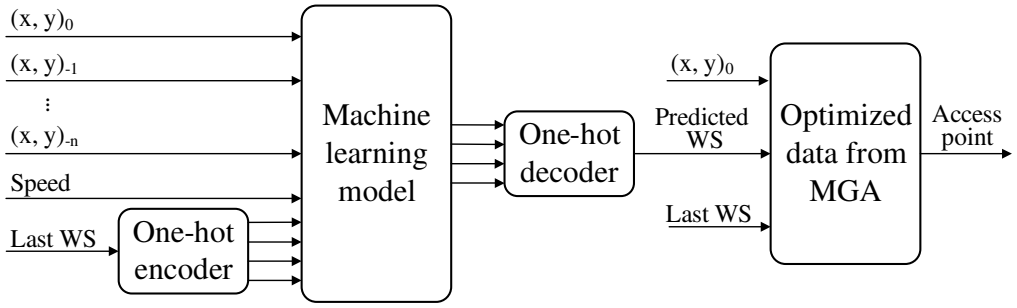

Figure 5.12. Real-time system architecture to find an access point to connect.

5.5.3. Data Processing

Following the approach described in [45], where the authors generated a dataset of 50 trajectories for a receiver within a three-workstation environment, we generated our dataset based on the four-workstation scenario depicted in Figure 5.7.

Using the transition probabilities illustrated in Figure 5.13, the receiver begins at a randomly selected workstation and transitions to the next one based on the corresponding probabilities. As an example, a receiver starting at WS C can select its next workstation with probabilities of 80%, 10%, and 10% for WS A, B, and D, respectively. This process is repeated until 100 trajectories are completed, saving the data to form a dataset. Each input feature was individually normalized to a range between zero and one.

The generated dataset, with 37201 samples, was split into three subsets: training (70%), validation (15%), and test (15%). However, due to the time-series nature of the data, the subsets were split sequentially, with the training set representing the first 70 trajectories, the validation set the next 15 trajectories, and the test set the last 15 trajectories.

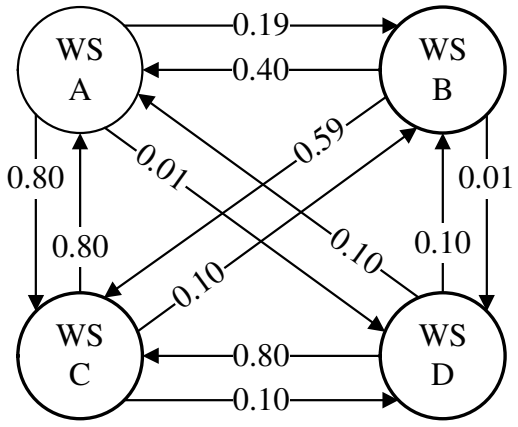

Figure 5.13. Schematic view of possible receiver workstation transitions with their probabilities. WS: Workstation.

5.6. Machine Learning Algorithms: training and hyperparameters optimization

As ML models can archive minimal latency in the predictions, we applied Decision Tree, LSTM, ANN, and TCN, which are described in Section 2.3. The Decision Tree classifier is used as a benchmark for the other models. Since hybrid neural networks can improve prediction accuracy [149], we incorporated a fully connected ANN after the output layer of LSTM and TCN models to improve their performances. Additionally, to address the classification problem, the activation function of the ANN last layer was set up with Softmax due to its proficiency in handling classification tasks.

The loss and metric functions for the models were defined as categorical cross-entropy and accuracy, respectively. Aiming at enhancements in the optimization and training time, an early stopping was configured to end the training after 10 consecutive epochs with a loss improvement lower than 0.001. Moreover, as manual hyperparameter searching is an inefficient task, we applied the Optuna framework described in Section 2.3.7 to optimize the models' hyperparameters. The framework was configured to perform 200 trials and employed the tree-structured Parzen estimator sampler algorithm. The objective was to maximize the average accuracy across the training, validation, and test datasets. The parameter ranges for the ML models optimized by Optuna are presented in Table 5.2.

5.7. Results and Discussions

5.7.1. MGA Optimization

Table 5.3[†] shows the average EVM and number of handovers for each trajectory and speed obtained after the application of STD and MGA strategies. The MGA significantly reduced the number of handovers for all evaluated trajectories, demonstrating reductions of up to 75% (D$\rightarrow$C with 1 m/s).

Analyzing the EVMs for speeds under 3 m/s, the STD demonstrated lower EVMs than MGA due to the power-based approach to trigger a handover. This approach provides a better SNR, increasing the EVM along the trajectory at the cost of increases in the number of handovers. In contrast, as the MGA considers positioning to trigger a handover, it reduces the number of handovers by skipping unnecessary handovers. Despite the fact that the MGA approach increases the EVMs, the algorithm kept the performance under the FEC limit.

When the receiver's speed increased above 3 m/s, the STD average EVMs increased. This occurred because the TTT parameter is static and does not follow the receiver with a high speed, which requires the handover decisions to be made more quickly. This effect did not occur with

[†]A correction to Table III from our publication [150] has been applied in Table 5.3. Specifically, the number of handovers in both strategies was decreased by one due to a calculation error.

Table 5.2. Hyperparameter ranges for the ML models

Model	Hyperparameter	Range
Decision Tree	Time-series input length	3 to 15
	Max. depth of the tree	[10, 20, ..., 100] or None
	Max. Features	'log2' or 'sqrt'
	Min. n. of samples to split	[2, 5, 10]
	Min. n. of samples to leaf	[1, 2, 4]
LSTM-ANN	Number of LSTM layers	2 to 10
	Number of LSTM cells	[8, 16, 32, 64, 128, 256]
	Batch size	[32, 64, 128]
	Dropout	[0.05, 0.10, ..., 0.25, 0.30]
	Time-series input length	3 to 15
	Activation function	Sigmoid, Tanh
	Optimizer	Adam, SGD, RMSprop
	Number of Dense layers	1 to 5
	Number of Dense neurons	[16, 32, 64, 128, 256]
	Maximum training epoch	50
TCN-ANN	Kernel Size	1 to 8
	Number of filters	[16, 32, 64, 128]
	Dilations	[1, 2, 4, 8, 16, 32, 64, 128]
	Batch size	[32, 64, 128]
	Dropout	[0.05, 0.10, ..., 0.25, 0.30]
	Time-series input length	[4, 8, 16, 32, 64]
	Activation function	Sigmoid, Tanh
	Optimizer	Adam, SGD, RMSprop
	Number of Dense layers	1 to 5
	Number of Dense neurons	[16, 32, 64, 128, 256]
	Maximum training epoch	50

Table 5.3. Results for MGA and STD.

Traj.	1 m/s				2 m/s				3 m/s				4 m/s				5 m/s			
	EVM (%)		N. of Hand.		EVM (%)		N. of Hand.		EVM (%)		N. of Hand.		EVM (%)		N. of Hand.		EVM (%)		N. of Hand.	
	STD	MGA	STD	MGA	STD	MGA	STD	MGA	STD	MGA	STD	MGA	STD	MGA	STD	MGA	STD	MGA	STD	MGA
C→D	**1.41**	1.61	3	**1**	**1.48**	1.55	3	**1**	**1.51**	1.54	3	**1**	**1.60**	1.83	3	**1**	**1.69**	1.83	3	**1**
C→B	**3.16**	4.17	7	**3**	**3.44**	4.71	7	**3**	**3.62**	4.49	7	**4**	**3.66**	4.43	7	**3**	**3.76**	4.10	6	**3**
C→A	**2.67**	3.65	4	**2**	**2.82**	3.95	4	**2**	**2.89**	3.76	4	**2**	4.73	**4.10**	5	**2**	9.23	**3.49**	4	**2**
D→C	**1.32**	1.53	4	**1**	**1.40**	1.52	3	**1**	**1.41**	1.54	3	**1**	1.58	**1.55**	3	**1**	1.69	**1.61**	3	**1**
D→B	**3.21**	3.96	10	**6**	**3.08**	4.41	10	**4**	**3.81**	3.84	10	**5**	**3.09**	4.03	10	**6**	**3.80**	3.88	9	**6**
D→A	**2.95**	3.21	7	**3**	**2.61**	3.61	7	**4**	**3.46**	3.59	7	**3**	**2.46**	4.09	7	**3**	3.38	**3.21**	6	**3**
B→C	**3.27**	4.30	8	**4**	**3.63**	4.67	8	**5**	**3.90**	4.16	8	**4**	**3.93**	4.37	8	**3**	7.79	**4.39**	8	**3**
B→D	**3.00**	4.22	11	**6**	**2.96**	4.43	11	**4**	**3.56**	3.99	11	**6**	**3.20**	3.60	11	**5**	5.21	**3.67**	11	**8**
B→A	**3.95**	4.96	3	**1**	**4.47**	5.28	3	**1**	**4.78**	5.03	3	**1**	4.89	**4.81**	3	**1**	5.00	**4.67**	2	**1**
A→C	**2.84**	3.73	5	**2**	**3.13**	3.96	5	**2**	**3.32**	4.08	5	**2**	**3.33**	4.12	5	**2**	7.49	**3.88**	5	**3**
A→D	**2.66**	2.68	8	**5**	**2.44**	4.17	8	**4**	3.25	**3.13**	8	**5**	**2.61**	2.86	8	**4**	4.99	**3.24**	8	**4**
A→B	**3.94**	4.95	3	**1**	**4.41**	5.28	3	**1**	**4.77**	5.28	3	**1**	**4.83**	5.13	3	**1**	4.97	**4.69**	2	**1**

Values highlighted in bold show the best values comparing STD and MGA.

the MGA strategy, as it considers spatial references for the handover decisions. Figure 5.14 shows the results for the trajectory C→A, highlighting this effect, with the STD average EVM growing from 2.67 to 9.23%. This occurred because the handover decisions took a long time to be triggered and the receiver crosses areas with low SNR or even outside the FOV, where the system tries to recover data from the noisy signal. For MGA, the EVMs are almost constant along the trajectory.

Figure 5.14 also shows that using MGA, a large reduction in the number of handovers was obtained. The MGA significantly decreases the total number of handovers in all trajectories and speeds. In some cases, the decrement was around 66.66% (from 3 to 1 handovers), as shown in the C→D. The average EVMs for STD are predominantly slightly lower than the EVMs for MGA. However, the EVMs are below the FEC limit as this threshold was set as one of the optimization constraints.

5.7.2. Model Optimization, Training, and Test

Table 5.4 shows the optimal hyperparameters obtained after the Optuna optimization on the ML models. Figure 5.15 shows the training and validation accuracy scores reached using the optimal hyperparameters of the LSTM-ANN and the TCN-ANN. The convergent nature of these curves suggests that the models were successfully trained without overfitting.

The accuracy and loss scores for the models are presented in Table 5.5. The Decision Tree showed the best accuracy score for the training dataset, while LSTM-ANN achieved the best scores for the validation and test datasets. In general, the Decision Tree results present great results for accuracy, however, the losses for validation and test dataset were high, indicating a certain level of instability in the model. On the other hand, LSTM-ANN and TCN-ANN demonstrated more consistent and lower losses, indicating greater stability of these models. However, they showed accuracy below 90% for the training dataset and over 96% for the test dataset. This discrepancy can be attributed to the relatively small size of the test dataset, which can be composed of trajectories where the models have good performances, leading to high accuracies. More details will be addressed in Section 5.7.3.

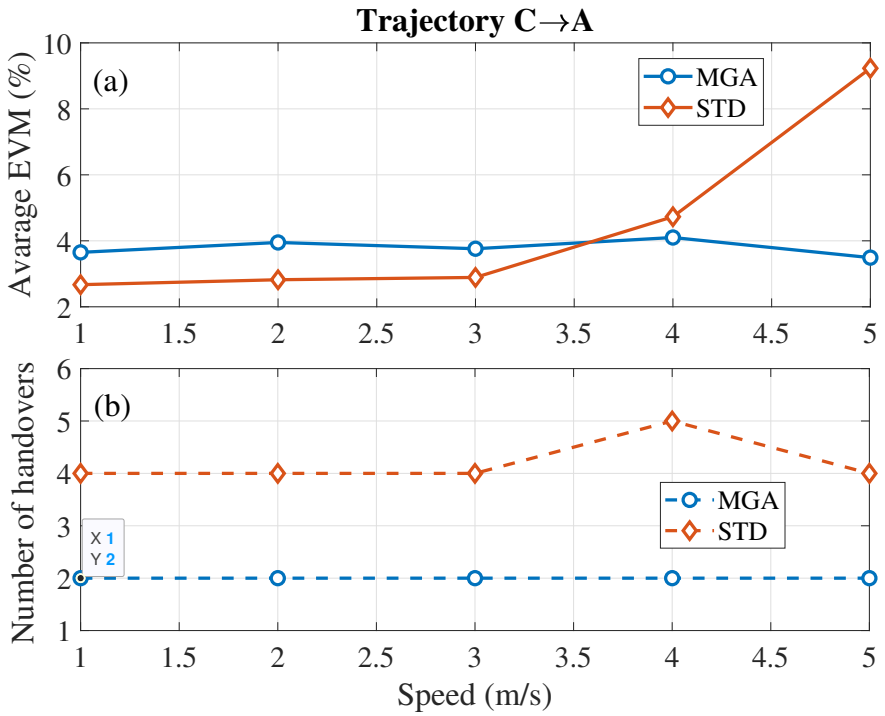

Figure 5.14. MGA and STD handover results for trajectory C→A: (a) the average EVM and (b) the total number of handovers for each speed.

Considering a scenario in which errors are considered in the positions of the test dataset, according to the model described in Section 5.5.1, the LSTM-ANN and TCN-ANN models show great robustness against errors, even though the models were trained with an error-free dataset. In contrast, the errors impacted the Decision Tree model, showing a higher loss and lower accuracy.

Table 5.6 presents the cumulative number of handovers across the test dataset for each strategy. Due to its accuracy, the LSTM-ANN outperformed the other models, achieving the most favorable outcome with 42 handovers. This is represented by a reduction of 42.47%, when compared to the STD. The Decision Tree and the TCN-ANN models also demonstrated significant improvements, showing reductions of 24.66% and 31.51%, respectively. Although the ML models with MGAD led to slightly higher average EVMs, there is no significant impact on the system's performance since all EVMs are below the FEC limit. However, the standard deviation of STD was higher than those provided by the ML models, mainly due to its limitation in handling different speeds (see Figure 5.14). Compared to the error-free dataset, the test dataset with error increases the number of handovers in 2 and 4 units when the LSTM-ANN and TCN-ANN are used, respectively, confirming the robustness of both models. In its turn, the Decision Tree increases the handovers by 73 units. Thus, the LSTM-ANN and TCN-ANN decreased the handovers by 39.73% and 26.03%, respectively, when compared to STD. In contrast, the Decision Tree increases the handovers by 75.34%, demonstrating its unfeasibility.

To further investigate the EVMs across the test dataset, Figure 5.16 illustrates the CDF for

Table 5.4. Hyperparameter chosen by Optuna for the ML models

Model	Hyperparameter	Value
Decision Tree	Time-series input length	14
	Max. depth of the tree	10
	Max. features	log2
	Min. n. of samples to split	5
	Min. n. of samples to leaf	2
LSTM-ANN	Number of LSTM layers	4
	LSTM cells of each layer	64, 64, 32, 128
	Batch size	32
	Dropout	0.05
	Time-series input length	14
	Activation function	Sigmoid
	Optimizer	RMSprop
	Number of dense layers	1
	Neurons of each dense layer	4
TCN-ANN	Kernel Size	6
	Number of filters	64
	Dilations	$[1, 2]$
	Batch size	64
	Dropout	0.15
	Time-series input length	32
	Activation function	Tanh
	Optimizer	SGD
	Number of dense layers	3
	Neurons of each dense layer	16, 16, 4

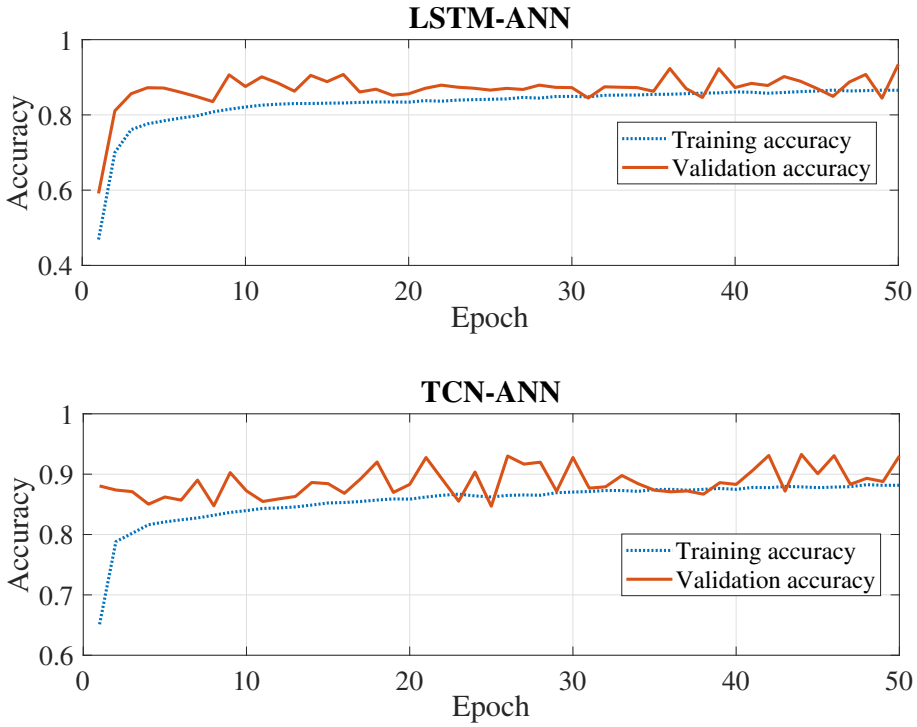

Figure 5.15. The accuracy obtained in the training and validation of the optimized LSTM-ANN and TCN-ANN models.

Decision Tree, LSTM-ANN, and TCN, considering the test dataset with error. The LSTM-ANN + MGAD and TCN + MGAD strategies maintained 100% of the EVM values below 10%, respecting the FEC limit. In contrast, the STD and Decision Tree strategies achieved 99.8% of EVM values below 10%, showing other EVMs of about 140%. This demonstrates that the strategies lead the receiver to experience regions outside of the FOV where the system tried to retrieve data from noisy signals.

Table 5.7 shows the computational resources used by ML models running in a laptop with an Intel Core i7 8th Gen processor and 16 GB of Random Access Memory (RAM). It shows that the memory usage of the ML models is compatible with modern hardware computers. Furthermore, although a significant amount of time is necessary to train all models, once this process is done, the processing time to generate a prediction is extremely low, showing that, with the exception of the Decision Tree (due to the huge amount of handovers), the application of the other proposed ML models is feasible in real-life scenarios.

5.7.3. Further Investigation on Accuracy

The difference between the accuracy of the datasets shown in Table 5.5 led us to further investigations. Table 5.8 shows the dataset distribution and the scores of the first occurrence of each trajectory in the error-free dataset. Fortuitously, the test dataset was composed of trajectories with high accuracy scores, which explains the differences in accuracy of the datasets for LSTM-ANN and TCN-ANN. Furthermore, the trajectory D→B does not appear in the train-

Table 5.5. Loss and accuracy results.

Model	Dataset	Loss		Accuracy	
Decision Tree	Training	0.0919	-	0.9507	-
	Validation	2.2513	-	0.9267	-
	Test	1.7830	3.2610*	0.9519	0.9115*
LSTM-ANN	Training	0.2679	-	0.8869	-
	Validation	0.3513	-	0.9342	-
	Test	0.2414	0.2467*	0.9883	0.9856*
TCN-ANN	Training	0.2746	-	0.8826	-
	Validation	0.3411	-	0.9301	-
	Test	0.2368	0.2431*	0.9661	0.9590*

* Results obtained by adding errors to the coordinates.

Table 5.6. Handover results for the test dataset.

	Handovers		Average EVM (%)	
STD	73	-	3.27 ± 4.68	-
Decision Tree + MGAD	55	128*	4.05 ± 1.72	4.19 ± 5.11*
LSTM-ANN + MGAD	42	44*	4.07 ± 1.73	4.08 ± 1.73*
TCN-ANN + MGAD	50	54*	4.09 ± 1.74	4.09 ± 1.75*

* Results obtained by adding errors to the coordinates.

ing dataset, appearing only in the validation dataset. Thus, the validation dataset achieved low scores, highlighting the difficulty of models generalization.

As can be seen in Table 5.5, the Decision Tree model presented significant variation in the loss scores of the datasets. This can be explained by trajectories with extremely high losses, as demonstrated by the trajectory D→B shown in Table 5.8. Thus, we conjecture that trajectories in other speed cases present high losses as well, contributing to the Decision Tree model loss variation.

It can be observed from Figure 5.7 that some trajectories share some paths, leading to ambiguities in the training process because there are cases where the same inputs provide different outputs. For example, consider a scenario in Figure 5.7 where the receiver departs from WS A towards WS C. During the transition between AP(7) and AP(8), the model inputs are the same as the scenario in which the receiver leaves WS A and goes to WS D. Thus, considering

Table 5.7. ML Memory usage and prediction time.

	Mem. Usage	Time per Prediction
Decision Tree	345.5 MiB	0.47 μs
LSTM-ANN	390.7 MiB	60.22 μs
TCN-ANN	393.1 MiB	72.04 μs

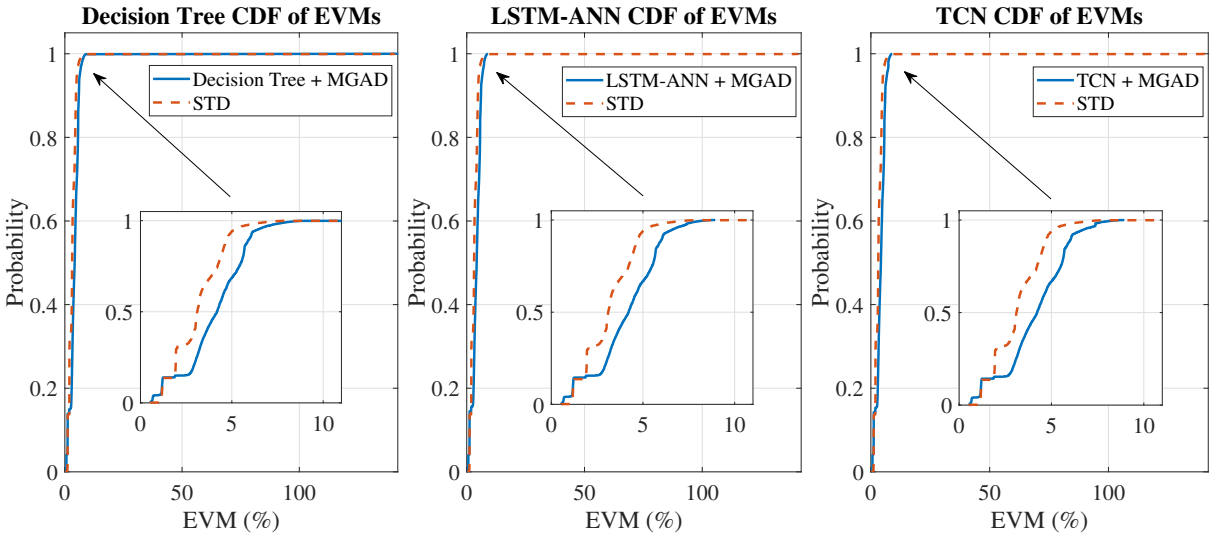

Figure 5.16. EVM CDFs of the test dataset for AI models and STD strategies.

these inputs, sometimes the model will be trained with WS C as output and sometimes it will be trained with WS D as output, bringing ambiguity to the training process. To investigate the impact of this issue, a new non-realistic scenario removing overlapping trajectories was created, as illustrated in Figure 5.17. Considering this new scenario, a new dataset was generated and segmented as described in Section 5.5. The models' training and optimization remained the same as detailed in Section 5.6.

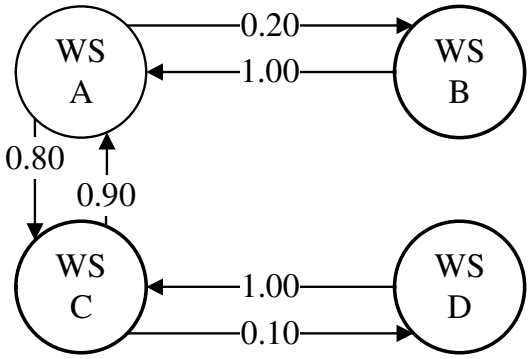

Figure 5.17. Schematic view of receiver workstation transitions with their probabilities for a non-overlapping scenario. WS: Workstation.

The results shown in Table 5.9 were obtained after the application of the AI-based models considered in this work. The impressive $\approx$ 99 % of accuracy and low loss scores across all instances were achieved. Additionally, the models demonstrate robust consistency, as evidenced by the marginal variations in the scores across different datasets. Therefore, even though we simplified the scenario by removing overlapping trajectories, the results strongly indicate that the ambiguous dataset impacted the models' training, leaving a research gap in study tools dealing with overlapping trajectories.

Table 5.8. Trajectories scores and dataset distribution.

Trajectory	Decision Tree		LSTM-ANN		TCN-ANN		Quantity of Trajectory		
	Loss	Acc.	Loss	Acc.	Loss	Acc.	Training	Validation	Test
C→D	0.000*	1.000*	0.002*	1.000*	0.003*	1.000*	5	1	0
C→B	0.701*	0.640*	1.507*	0.335*	1.667*	0.409*	4	1	0
C→A	0.094*	1.000*	0.107*	1.000*	0.057*	1.000*	22	5	7
D→C	0.000•	1.000•	0.006•	1.000•	0.002•	1.000•	4	0	0
D→B	30.763*	0.135*	3.505*	0.256*	3.115*	0.264*	0	1	0
D→A	0.000*	1.000*	0.721*	0.710*	0.662*	0.570*	1	0	0
B→C	0.000*	1.000*	0.043*	1.000*	0.012*	1.000*	5	2	2
B→D	-	-	-	-	-	-	0	0	0
B→A	0.000◇	1.000◇	1.013◇	0.335◇	1.112◇	0.361◇	3	0	0
A→C	0.00*	1.00*	0.014*	1.000*	0.004*	1.000*	22	5	4
A→D	-	-	-	-	-	-	0	0	0
A→B	0.000•	1.000•	0.324•	1.000•	0.202•	0.985•	4	0	2

receiver's speeds: *5 m/s, •2 m/s, and ◇1 m/s

Table 5.9. Loss and accuracy results for the non-overlapping dataset.

Model	Dataset	Loss	Accuracy
Decision Tree	Training	0.0013	0.9992
	Validation	0.0005	1.0000
	Test	0.0134	0.9988
LSTM-ANN	Training	0.0354	0.9872
	Validation	0.0056	0.9980
	Test	0.0278	0.9900
TCN-ANN	Training	0.0241	0.9901
	Validation	0.0071	0.9972
	Test	0.0171	0.9932

5.7.4. Experimental Evaluations

5.7.4.1. Three-transmitter scenario

Considering that the proposed LSTM-ANN + MGAD handover strategy achieved the best performance in the simulations, we evaluated its application in the experimental setup depicted in Figure 5.2. Thus, we have chosen an experimental scenario in which four WS and six trajectories are considered, as shown in Figure 5.18 (a). The dataset was generated as described in Section 5.5, however, considering the new trajectories and the probabilities described in Figure 5.18 (b). Due to the processing time limitation of our setup, we did not consider the receiver speed.

After the Optuna optimization, the LSTM-ANN model for the experimental scenario was configured with 32 and 256 cells in its layers. The three layers of the ANN were set with 16,

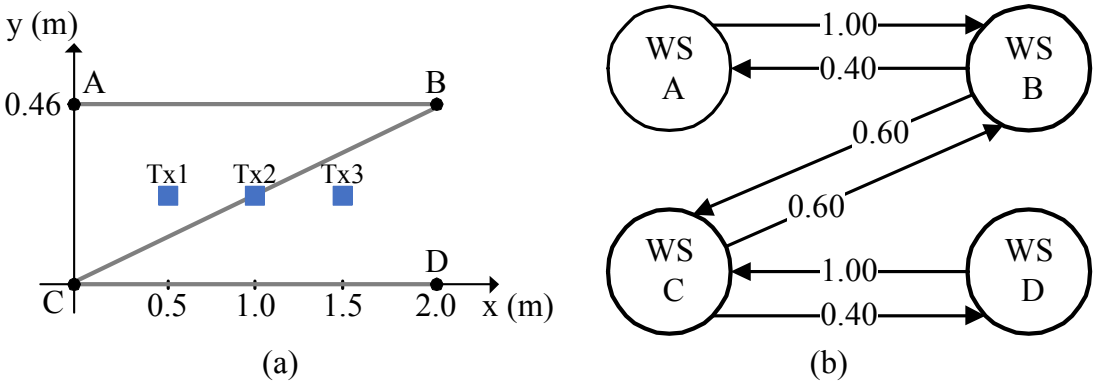

Figure 5.18. (a) Schematic view of the experimental scenario, workstations and trajectories. (b) Workstation transitions with their probabilities.

128, and 4 neurons each. The time-series input length, batch size, and dropout were defined as 11, 32, and 0.3, respectively, while the activation function and optimizer were defined as Tanh and Adam, respectively. The LSTM-ANN model achieved accuracies of 91.60%, 94.35%, and 96.77% for training, validation, and test datasets, respectively, while the losses were 0.15, 0.13 and 0.11. The hyperparameters are summarized in Table 5.10. Although the datasets do not have intersections in the trajectories, the accuracy and loss were impacted by the small number of samples per trajectory (9 samples). This means that one wrong prediction decreases the overall accuracy of the trajectory in 11.11% (1/9).

The LSTM-ANN + MGAD model achieved 15 handovers, whereas the STD model performed 28 exchanges on the test dataset, indicating a 46.43% reduction in handovers. The LSTM-ANN + MGAD model also exhibited a slightly higher average EVM of $13.32 \pm 1.18\%$, compared to $12.93 \pm 0.85\%$ for the STD strategy. Nevertheless, LSTM-ANN + MGAD and STD performances remained under the FEC limit across all trajectories in the test dataset, as demonstrated by the CDF curves in 5.19 where 100% of the EVMs were under 16.75% and 13.55%, respectively. To emphasize this, Figure 5.20 shows the performance measured along trajectory C→B, highlighting where the handovers occurred for both strategies. Notably, the LSTM-ANN + MGAD strategy skipped the connection with Tx2 as it held the connection with Tx1 until the moment at which Tx3 reached a better condition (see the spectrum depicted inset Figure 5.20) to trigger the handover, thus decreasing one handover when compared to STD. By skipping Tx2, the proposed model increased the EVM around the handover point. However, this strategy successfully maintained the EVM under the FEC limit across the trajectory, as can be seen by the scatterplots shown in the inset of Figure 5.20.

5.7.4.2. Four-transmitter scenario

Aiming to evaluate the performance of the proposed LSTM-ANN + MGAD handover strategy in a larger scenario with more trajectories, the proposal was applied to the four-transmitter scenario illustrated in Figure 5.3. This scenario included four workstations and ten trajectories,

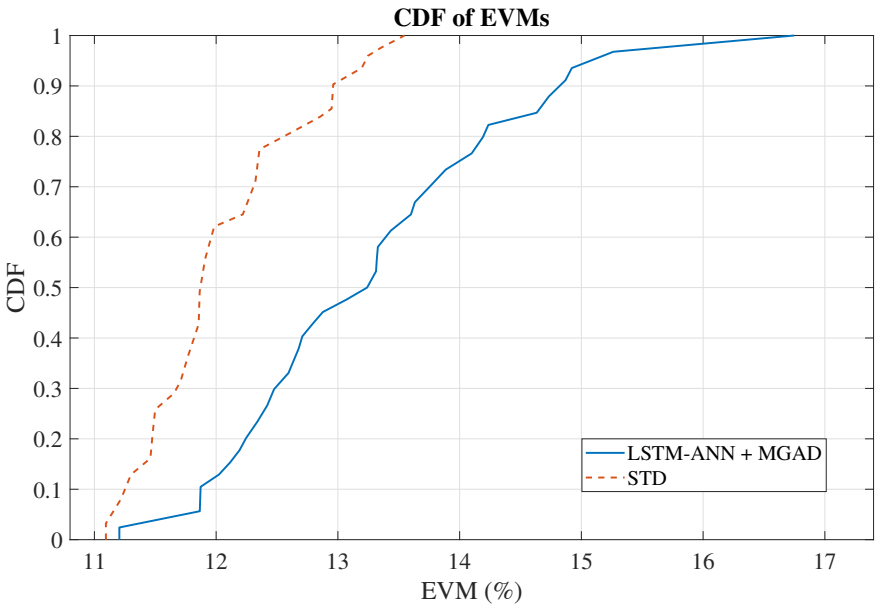

Figure 5.19. EVM CDF of the test dataset for LSTM + MGAD and STD strategies in the three Txs scenario.

as shown in Figure 5.21 (a). For evaluation purposes, a new dataset was generated based on these trajectories and their transition probabilities outlined in Figure 5.21 (b). As in the three-transmitter scenario, the dataset generation followed the process described in Section 5.5. The receiver speed was not considered due to the processing time limitations of our setup.

In the same way, the LSTM-ANN hyperparameters were optimized by Optuna, resulting in an architecture with two LSTM layers and one ANN layer. The LSTM layers were configured with 256 and 32 cells, respectively, while the ANN output layer included 4 neurons. The input length for the time series, batch size, and dropout rate were set to 10, 64, and 0.05, respectively. The Tanh activation function and the Adam optimizer were also applied. The LSTM-ANN model achieved accuracies of 93.49%, 97.64%, and 91.18% for the training, validation, and test datasets, respectively, with corresponding losses of 0.17, 0.10, and 0.31. A summary of the hyperparameters is provided in Table 5.10.

The STD handover strategy resulted in 22 handovers for the test dataset, whereas LSTM-ANN + MGAD achieved 12 handovers, representing a 45.45% reduction. Similar to the three-transmitter scenario, LSTM-ANN + MGAD presented a slightly higher average EVM of $12.30\pm 1.42\%$ compared to the STD EVM of $12.06 \pm 0.93\%$, as it prioritized reducing handovers. Nonetheless, the CDF curves of the test dataset EVMs, shown in Figure 5.22, reveal that both STD and LSTM-ANN + MGAD achieved 100% of the EVMs under 14.63% and 16.59%, respectively. Both strategies performed entirely within the 4-QAM FEC limit, highlighting the potential of the LSTM-ANN + MGAD approach.

The reduction in handovers was primarily observed in trajectories where the highest received power fluctuated between transmitters, resulting in a higher number of handovers with the STD

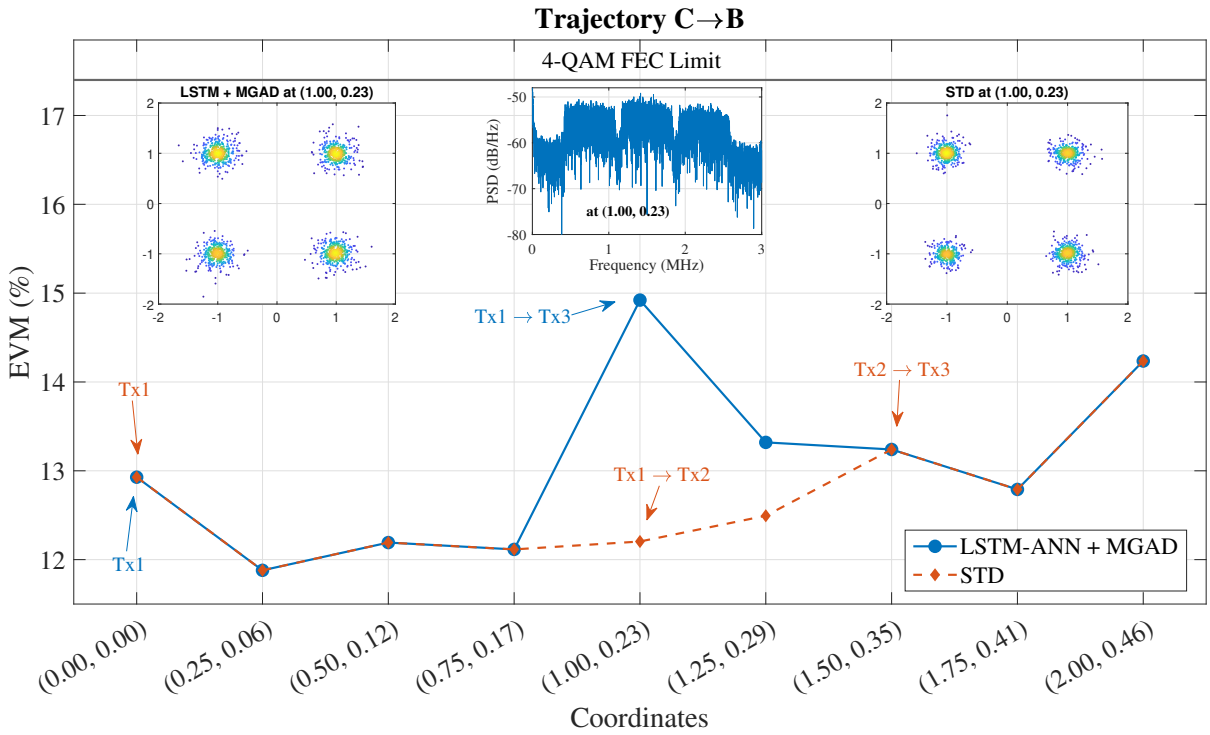

Figure 5.20. Trajectory C→B performance evaluation where each EVM shows the mean value of 10 measurements.

strategy. In contrast, The LSTM-ANN + MGAD maintains the connection, aiming to reduce the handovers while preserving EVM performance under the FEC limit. This behavior is illustrated in Figure 5.23, where both strategies began trajectory A→C connected to Tx1. The STD performed 3 exchanges following the strongest signal, while the LSTM-ANN + MGAD waited until Tx4 achieved a stable performance to do only one exchange from Tx1 to Tx4. In some cases, such as trajectory B→C shown in Figure 5.24, the LSTM-ANN + MGAD achieved the same number of handovers as STD where both strategies initiated connected to Tx3 and maintained it throughout the trajectory, as it was the optimal solution.

Table 5.10. LSTM model hyperparameters optimized by Optuna for the scenarios with three and four transmitters.

Model	Hyperparameter	Three Txs	Four Txs
LSTM-ANN	Number of LSTM layers	2	2
	LSTM cells of each layer	32, 256	256, 32
	Batch size	32	64
	Dropout	0.3	0.05
	Time-series input length	11	10
	Activation function	Tanh	Tanh
	Optimizer	Adam	Adam
	Number of dense layers	3	1
	Neurons of each dense layer	16, 126, 4	4

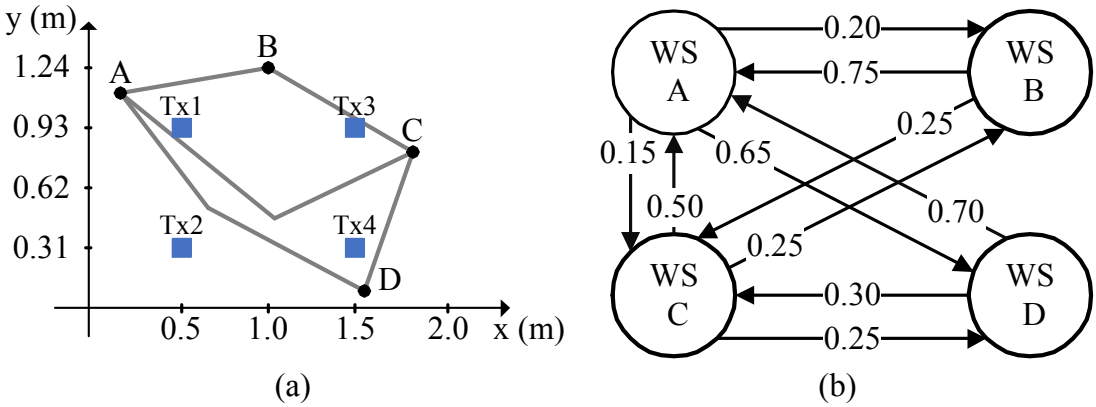

Figure 5.21. (a) Schematic view of the experimental scenario with four transmitters, workstations, and trajectories. (b) Workstation transitions with their probabilities.

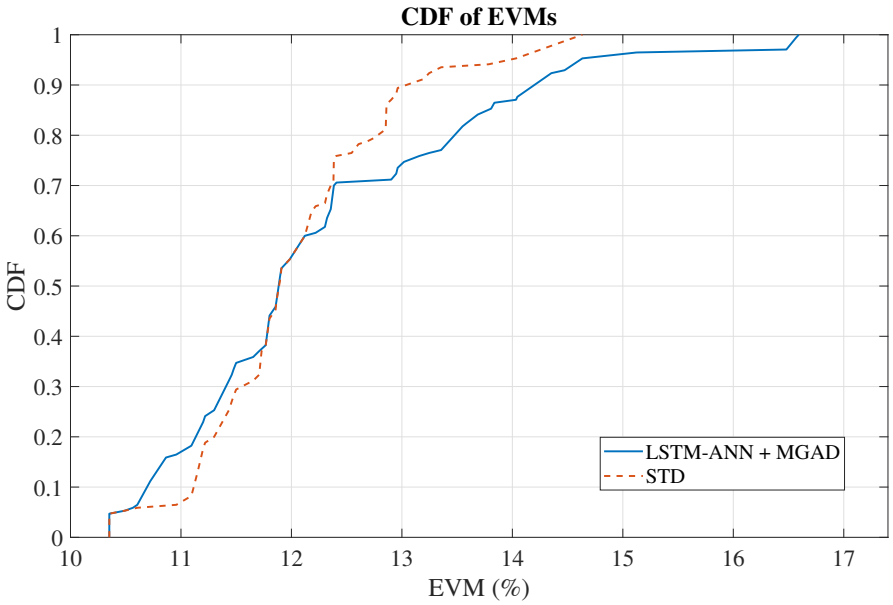

Figure 5.22. EVM CDF of the test dataset for LSTM + MGAD and STD strategies in the four-transmitter scenario.

5.8. Conclusions

A real-time handover scheme using optimization and machine learning was proposed to minimize the number of handovers of a digital twin-based VLC system. The proposed handover scheme considers trajectory information to optimize handover moments by applying a modified genetic algorithm. Additionally, ML models were implemented to predict the receiver's next destination. Thereafter, the real-time VLC system integrates the optimized handover data, predicted trajectory, and receiver's current position to trigger handovers, ensuring efficient and effective communication.

The MGA optimization provided reductions in the total number of handovers for all evaluated trajectories, showing a reduction of up to 75%, when compared to the power-based STD. The performance of the STD was notably impacted when the receiver's speed increased. This

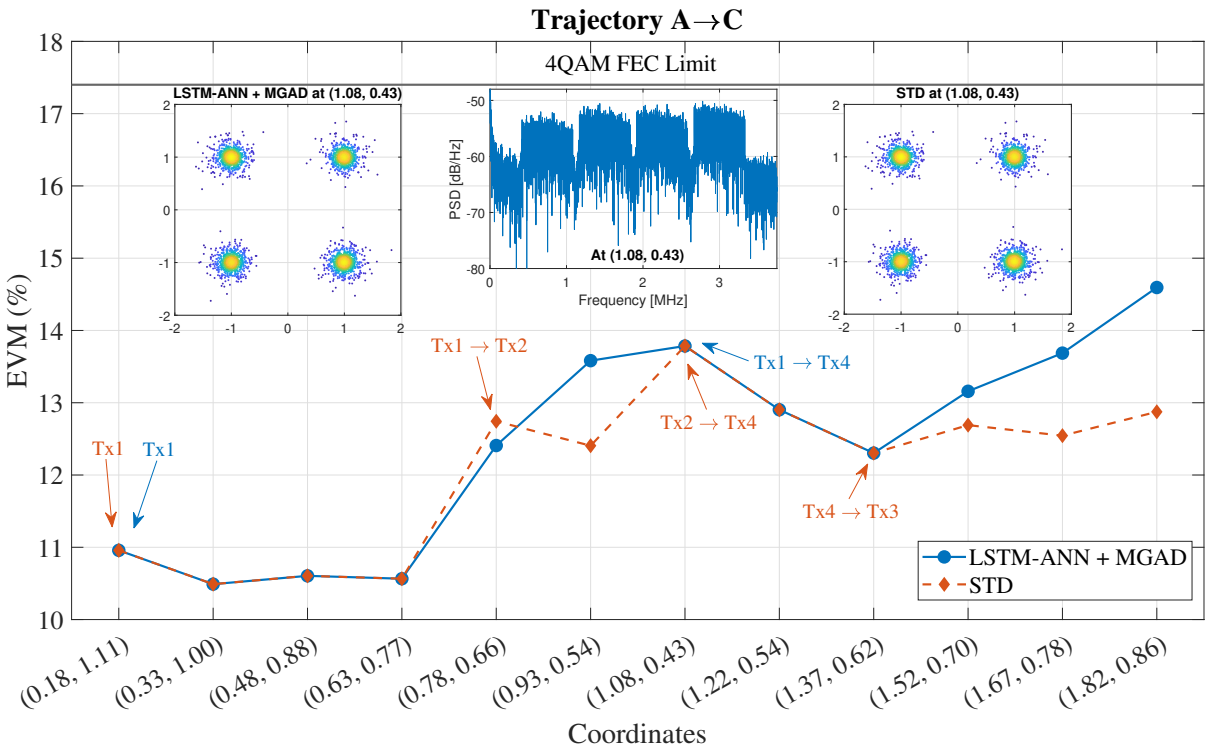

Figure 5.23. Trajectory A→C performance evaluation where each EVM shows the mean value of 20 measurements.

drawback was addressed by the MGA-based scheme due to the usage of spatial references in the handover decisions. Moreover, Decision Tree, LSTM-ANN, and TCN-ANN were applied to the real-time VLC system using the optimized handover data. Compared to STD, these AI-based models achieved a handover reduction of 24.66%, 42.47%, and 31.51% for the positioning error-free test dataset, respectively. Adding errors to the coordinates of the test dataset, the LSTM-ANN and TCN-ANN decrease the number of handovers by 39.73% and 26.03%, showing the robustness of the models. However, the Decision Tree increases the handovers by 75.34%, demonstrating the non-applicability of the model. The experimental results demonstrated that the LSTM-ANN with MGA data strategy proposed in this Chapter achieved a handover reduction of 46.43% and 45.45% for three txs and four txs scenarios, respectively, by skipping unnecessary exchanges. Thus, the handover schemes using LSTM-ANN and MGA data demonstrated a solid ability to minimize the number of handovers and to improve the overall system performance, even considering errors in the positioning system.

The fact that some trajectories shared part of the path, which is common in real-world applications, considerably impacts the models' training. These shared parts created ambiguity in the dataset where the same inputs have different outputs. When generating a dataset from a new scenario considering only non-overlapping trajectories, the accuracy score of the training dataset increases from around 88% to 99%, addressing the impact of overlapping trajectories on the score. Nevertheless, future research should investigate new ML architectures and other models to deal with ambiguous datasets caused by non-overlapping trajectories. A larger dataset

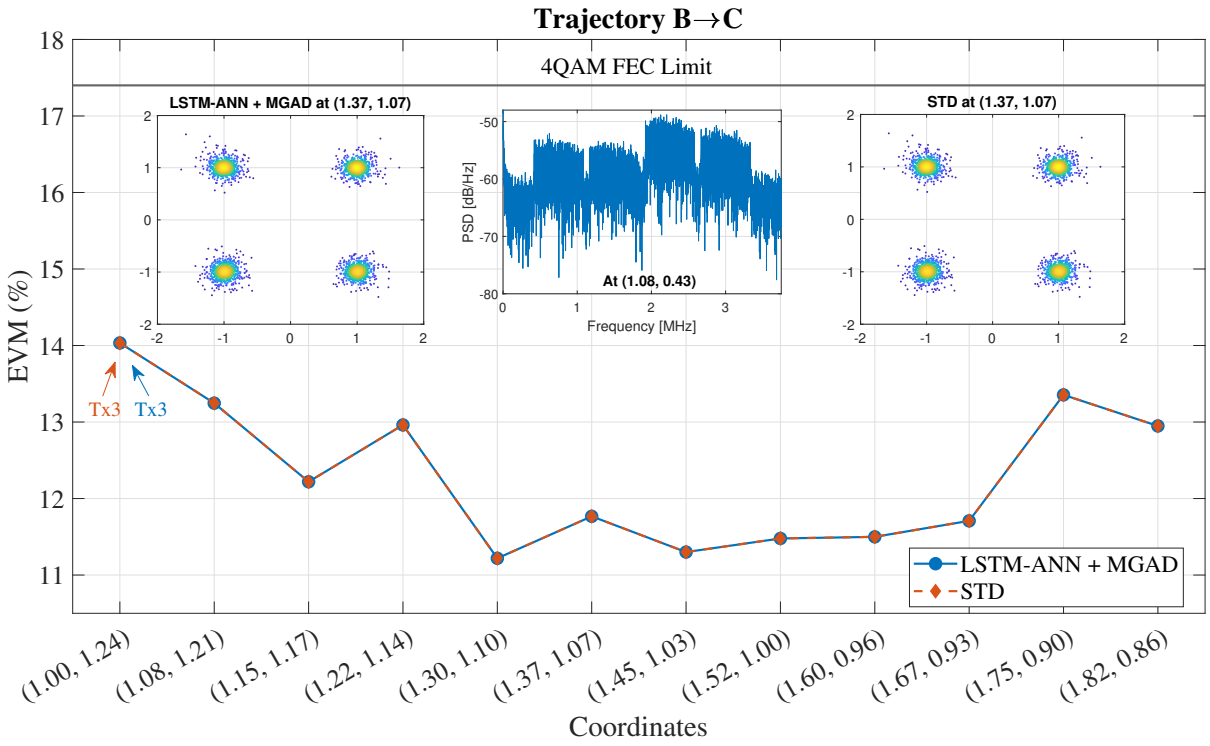

Figure 5.24. Trajectory B→C performance evaluation for the four-transmitter scenario where each EVM shows the mean value of 20 measurements.

should also be considered to provide more homogeneity in the sets. An experimental proof-of-concept of the 2D MISO simulation scenario exploited in this Chapter is part of our near-future work. In fact, we are currently designing an experimental setup in which we should evaluate the above-mentioned models' training impact. Furthermore, the physical twin implementation of the proposed scenario should be considered, taking into account a MIMO VLC scenario.

CHAPTER 6.

AI-Driven Enhancements for Handover in MIMO-based Visible Light Communication

6.1. Introduction

AI-based approaches have also demonstrated potential for MIMO VLC systems [151, 152]. In this Chapter, we extend the previously discussed handover strategies to a MIMO-VLC environment with 18 access points and two receivers. The MGA algorithm is applied to minimize the number of handovers along the trajectories, as frequent handovers can severely degrade the performance of VLC systems. Additionally, the LSTM-ANN model is employed to predict the next workstation for each receiver simultaneously, based on their respective trajectory information. The LSTM-ANN + MGA approach achieved a handover reduction of 44.70% and 48.61% for Rx1 and Rx2, respectively, when compared to the power-based STD strategy.

The remainder of this Chapter is organized as follows. Section 6.2 describes the real-time MIMO Handover System and its architecture. The LSTM-ANN training and hyperparameters optimizations are detailed in Section 6.3. The results and discussions are presented in Section 6.4. Finally, the conclusions are provided in Section 6.5.

6.2. Description of the Real-time MIMO System

Following the same approach described in Chapter 5, we implemented a MIMO handover system considering 18 APs and two receivers. The same AP distribution, WS, and trajectories defined in Figure 5.7 were applied. In this implementation, each receiver is allowed to follow its trajectory independently of the other. To enable simultaneous access for both receivers, we developed a simulation using an OFDM-based system, where each AP provides a separate channel for each receiver, as illustrated in Figure 6.1.

Figure 6.1 also illustrates the NR signals generated as in Section 5.3, which are composed of 42 data subcarriers multiplexed by a 128-point fast Fourier transform, considering 4-QAM as subcarrier mapping and cyclic prefix of 16 samples. The subcarrier spacing is defined as 15 kHz, while a lower bandwidth of 1 MHz is assigned since each AP transmits data to two receivers. Consequently, the carrier frequencies of the APs are spaced 4 MHz apart, starting at 2 MHz for Rx1 and 4 MHz for Rx2. The carrier frequencies for the APs are de-

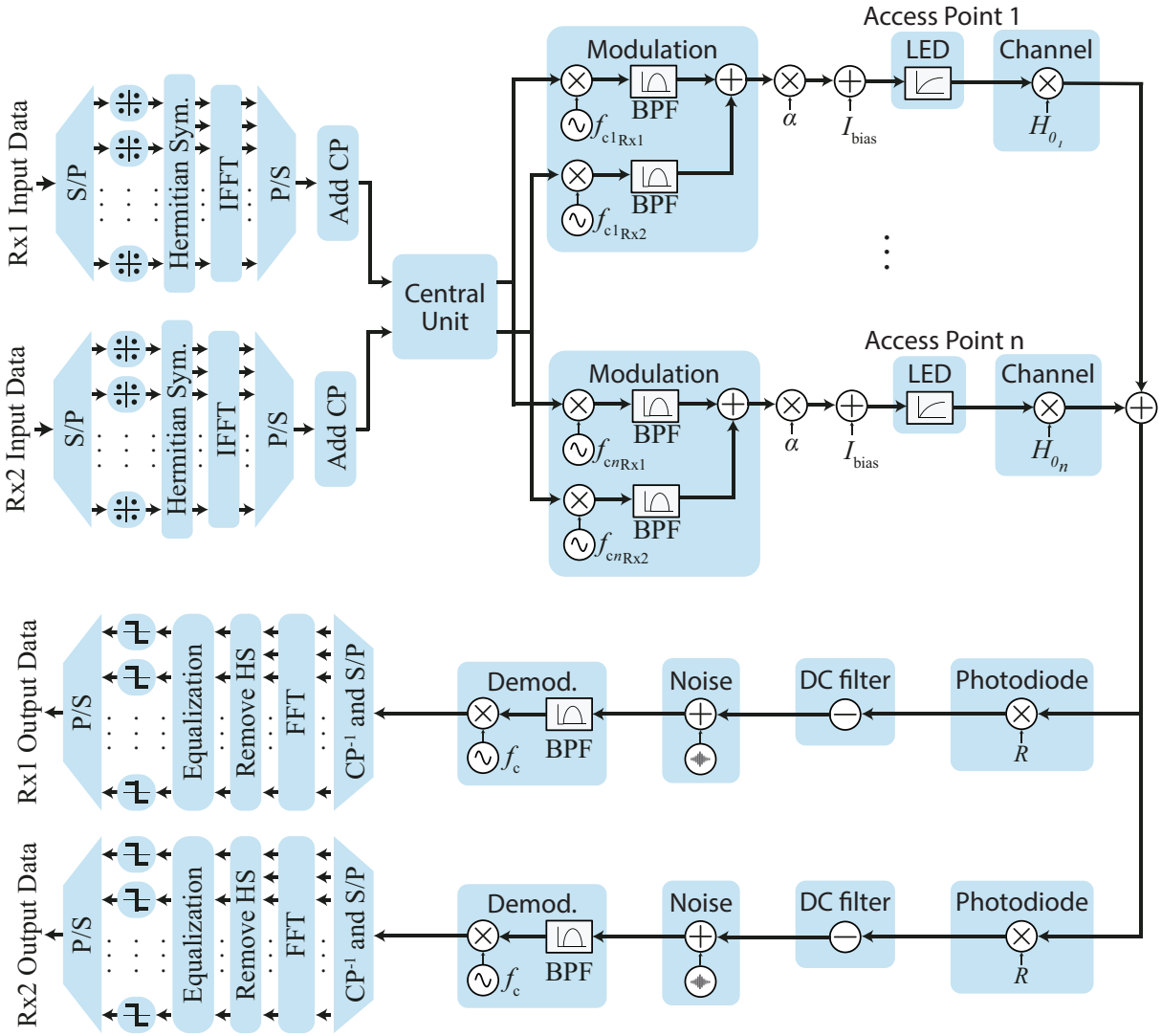

Figure 6.1. Block diagram of the OFDM-based MIMO VLC system STD.

noted as $[f_{\mathrm{c1}_{Rx1}}, f_{\mathrm{c2}_{Rx1}}, \ldots, f_{\mathrm{c18}_{Rx1}}] = [2, 6, \ldots, 70]$ MHz and $[f_{\mathrm{c1}_{Rx2}}, f_{\mathrm{c2}_{Rx2}}, \ldots, f_{\mathrm{c18}_{Rx2}}] = [4, 8, \ldots, 72]$ MHz.

To address this issue, we set the model inputs with both receivers' information to predict the receivers' next WSs simultaneously. Despite the fact that a different model can be applied to each receiver, we test this architecture to test the AI model's robustness.

We applied the handover optimization using the MGA algorithm described in Section 5.4 for this MIMO system. With the optimized handover data, it is necessary to know which trajectories the receivers are following, as the optimization was done based on the environment trajectories. To address this issue, we set the model inputs with both receivers' information to predict the receivers' next WSs simultaneously. Even though a different model could be applied to each receiver to predict the next WSs separately, one of the goals was to test the robustness of the AI model. Therefore, the inputs are defined as follows:

i. the last coordinates $[(x_{Rx1}, y_{Rx1})_0, (x_{Rx1}, y_{Rx1})_1, \cdots, (x_{Rx1}, y_{Rx1})_n]$ of Rx1 given by the

simulation scenario;

ii. the last coordinates $[(x_{Rx2}, y_{Rx2})_0, (x_{Rx2}, y_{Rx2})_1, \cdots, (x_{Rx2}, y_{Rx2})_n]$ of Rx2 from the simulation;

iii. Rx1 speed;

iv. Rx2 speed;

v. Rx1 last WS;

vi. Rx2 last WS.

Figure 6.2 illustrates a block diagram of the MIMO handover system where the inputs for the ML model are highlighted in the first block. The length of the input time-series of coordinates is determined by the Optuna hyperparameter optimization (See Section 2.3.7). The model outputs describe two WSs, representing a multi-label classification task. These outputs are decoded into two independent one-hot encoded representations: the first four outputs indicate the predicted WS for Rx1, while the last four represent the predicted WS for Rx2. Following the execution of the ML model, the final block combines the predicted WS, the last WS, the current position $[(x, y)_0]$, and the MGAD of each receiver to define the optimal AP for each receiver to connect to.

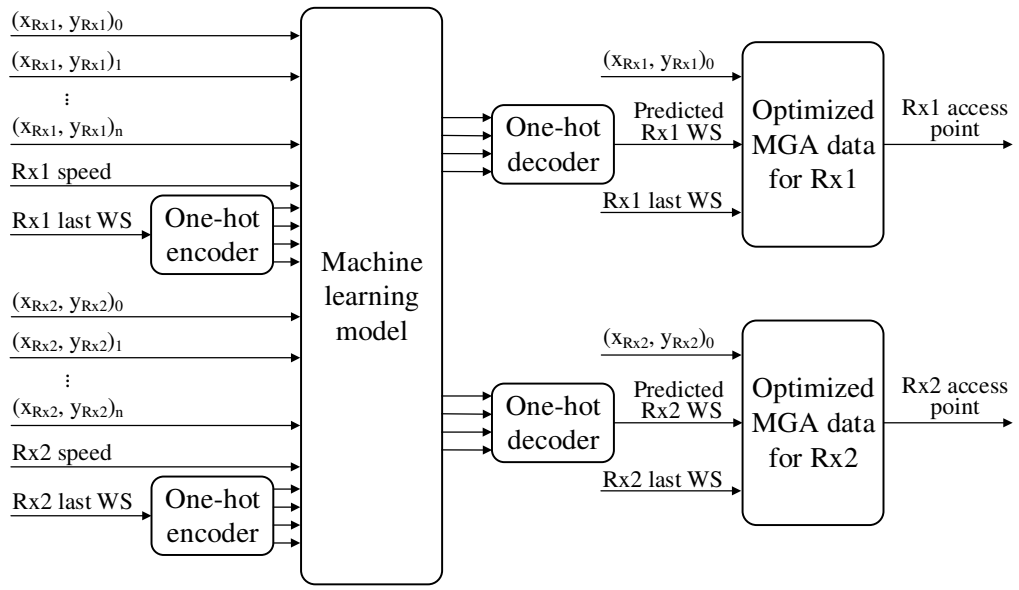

Figure 6.2. Real-time MIMO system architecture to find access points to connect.

The model's predictions may be inaccurate or unsuitable for the problem being addressed. For example, if the receiver's previous WS was A and the model predicts the same WS for the subsequent state, this outcome may not be realistic. To handle such situations, the handover system employs the STD algorithm to override the prediction.

6.3. LSTM-ANN: training and hyperparameters optimization

Since the LSTM-ANN model achieved the best performance in the MISO system described in Chapter 5, it was selected for the MIMO scenario as well. The architecture shown in Figure 6.2 represents a classification problem involving the prediction of two workstations simultaneously, thus implementing a multi-label classifier [153]. Unlike the multi-class classifier architecture described in Figure 5.12, which classifies only one workstation, the multi-label architecture requires the activation function of ANN last layer different from Softmax that ensures that the sum of the outputs equal to one (See Section 2.3.3). Therefore, the ANN last layer was configured with Sigmoid.

The dataset used to train the LSTM-ANN model was generated as described in Section 5.5.3, based on the probabilities illustrated in Figure 5.13. It consists of a total of 200 trajectories, considering 100 trajectories per receiver. The dataset was partitioned into three subsets: 70% for training, 15% for validation, and 15% for testing. The loss and metric functions for the models were set as categorical cross-entropy and accuracy, respectively. To improve optimization and reduce training time, an early stopping mechanism was implemented to terminate training after 10 consecutive epochs with a loss improvement below 0.001. The Optuna framework described in Section 2.3.7 was employed to optimize the LSTM-ANN hyperparameters with 200 trials using the tree-structured Parzen estimator sampler algorithm. The goal was to maximize the average accuracy across the training, validation, and test datasets. The parameter ranges for the LSTM-ANN optimized by Optuna are summarized in Table 6.1.

Table 6.1. Hyperparameter ranges for the LSTM-ANN model

Model	Hyperparameter	Range
LSTM-ANN	Number of LSTM layers	2 to 20
	Number of LSTM cells	$[8, 16, 32, 64, 128, 256, 512]$
	Batch size	$[32, 64, 128]$
	Dropout	$[0.05, 0.10, ..., 0.25, 0.30]$
	Time-series input length	3 to 15
	Activation function	Sigmoid, Tanh
	Optimizer	Adam, SGD, RMSprop
	Number of Dense layers	1 to 10
	Number of Dense neurons	$[16, 32, 64, 128, 256, 512]$
	Maximum training epoch	50

6.4. Results and Discussions

6.4.1. MGA Optimization

Table 6.2 presents the average EVM and number of handovers for the trajectories when applying the STD and MGA strategies for the Rx1. The MGA effectively minimized the number of handovers across all tested scenarios, for example, achieving reductions of up to 75% (D$\rightarrow$C

Table 6.2. MGA and STD Results for Rx1.

Traj.	1 m/s				2 m/s				3 m/s				4 m/s				5 m/s			
	EVM (%)		N. of Hand.		EVM (%)		N. of Hand.		EVM (%)		N. of Hand.		EVM (%)		N. of Hand.		EVM (%)		N. of Hand.	
	STD	MGA	STD	MGA	STD	MGA	STD	MGA	STD	MGA	STD	MGA	STD	MGA	STD	MGA	STD	MGA	STD	MGA
C→D	**1.48**	1.72	3	**1**	**1.56**	1.76	3	**1**	**1.58**	1.87	3	**1**	1.68	**1.61**	3	**1**	1.78	**1.70**	3	**1**
C→B	**3.32**	4.45	7	**3**	**3.60**	4.98	7	**3**	**3.80**	4.38	7	**4**	**3.84**	4.41	7	**3**	**3.95**	4.38	6	**3**
C→A	**2.80**	3.80	4	**2**	**2.95**	3.51	4	**2**	**3.03**	3.99	4	**2**	4.88	**3.61**	5	**2**	9.39	**3.91**	4	**2**
D→C	**1.38**	1.62	4	**1**	**1.47**	1.92	3	**1**	**1.48**	1.68	3	**1**	**1.66**	1.86	3	**1**	1.78	**1.66**	3	**1**
D→B	**3.37**	5.72	10	**5**	**3.22**	4.12	10	**5**	**3.99**	4.64	10	**4**	**3.23**	4.74	10	**4**	3.97	**3.81**	9	**5**
D→A	**3.09**	3.91	7	**4**	**2.74**	4.37	7	**4**	**3.64**	4.26	7	**4**	**2.58**	4.39	7	**4**	3.51	**3.33**	6	**3**
B→C	**3.43**	4.64	8	**5**	**3.82**	4.56	8	**4**	**4.08**	5.52	8	**3**	**4.14**	4.48	8	**3**	8.00	**4.75**	8	**3**
B→D	**3.15**	4.17	11	**6**	**3.11**	4.38	11	**5**	**3.75**	4.04	11	**6**	**3.36**	4.58	11	**5**	5.39	**4.11**	11	**5**
B→A	**4.15**	5.23	3	**1**	**4.68**	5.55	3	**1**	**5.01**	5.51	3	**1**	**5.11**	5.32	3	**1**	5.25	**5.14**	2	**1**
A→C	**2.98**	3.95	5	**2**	**3.29**	3.88	5	**2**	**3.49**	3.99	5	**2**	**3.48**	4.28	5	**2**	7.63	**4.27**	5	**2**
A→D	2.80	**2.78**	8	**4**	**2.56**	2.92	8	**4**	**3.42**	3.57	8	**3**	**2.75**	4.30	8	**3**	5.11	**3.92**	8	**4**
A→B	**4.14**	5.19	3	**1**	**4.63**	5.72	3	**1**	**5.00**	5.53	3	**1**	**5.08**	5.50	3	**1**	5.24	**5.06**	2	**1**

Values highlighted in bold show the best values comparing STD and MGA.

at 1 m/s). For speeds below 3 m/s, the STD yielded lower EVMs due to its power-based handover triggering, which improves performance at the cost of more frequent handovers. As the MGA uses positioning-based handover triggers, it eliminates unnecessary handovers, reducing their occurrence and maintaining EVM levels below the FEC threshold while slightly increasing the average EVM.

As expected, and according to the results discussed in Chapter 5, when the receiver's speed exceeded 3 m/s, the STD experienced a significant increase in average EVM, as its static TTT parameter did not adapt to higher speeds, delaying handover decisions. This delay caused the receiver to cross regions with poor SNR or outside the FOV, where the system tried to recover data from noisy signals. In contrast, the MGA strategy, which bases handover decisions on spatial references, maintained more consistent EVM values across the trajectory. Figure 6.3 illustrates this effect for the C→A trajectory, where the average STD EVM increased from 2.80% to 9.39%, while MGA kept EVMs nearly constant.

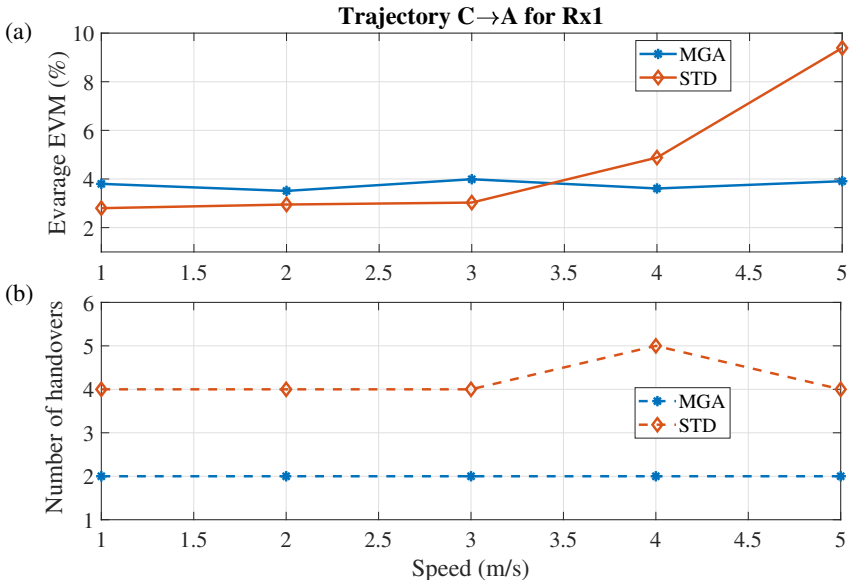

Figure 6.3. Rx1 MGA and STD handover results for trajectory C→A: (a) the average EVM and (b) the total number of handovers for each speed.

Table 6.3. MGA and STD Results for Rx2.

Traj.	1 m/s				2 m/s				3 m/s				4 m/s				5 m/s			
	EVM (%)		N. of Hand.		EVM (%)		N. of Hand.		EVM (%)		N. of Hand.		EVM (%)		N. of Hand.		EVM (%)		N. of Hand.	
	STD	MGA	STD	MGA	STD	MGA	STD	MGA	STD	MGA	STD	MGA	STD	MGA	STD	MGA	STD	MGA	STD	MGA
C→D	**1.47**	1.60	3	**1**	**1.56**	1.71	3	**1**	**1.58**	1.62	3	**1**	**1.68**	1.87	3	**1**	**1.78**	1.87	3	**1**
C→B	**3.31**	4.53	7	**3**	**3.60**	4.56	7	**4**	**3.79**	7.00	7	**4**	**3.84**	4.62	7	**3**	**3.96**	4.51	6	**3**
C→A	**2.80**	3.96	4	**2**	**2.95**	4.38	4	**2**	**3.03**	4.72	4	**2**	4.89	**4.46**	5	**2**	9.39	**4.07**	4	**2**
D→C	**1.38**	1.61	4	**1**	**1.48**	1.65	3	**1**	**1.48**	1.59	3	**1**	**1.66**	1.87	3	**1**	**1.78**	1.85	3	**1**
D→B	**3.37**	3.99	10	**6**	**3.22**	4.03	10	**6**	**4.00**	4.01	10	**6**	**3.25**	4.36	10	**5**	**3.98**	4.55	9	**4**
D→A	**3.09**	3.38	7	**4**	**2.74**	4.36	7	**3**	**3.63**	4.43	7	**4**	**2.59**	3.86	7	**4**	**3.52**	3.62	6	**4**
B→C	**3.43**	4.36	8	**3**	**3.81**	4.89	8	**3**	**4.09**	4.33	8	**5**	**4.14**	4.61	8	**3**	8.00	**4.61**	8	**3**
B→D	**3.14**	4.13	11	**5**	**3.11**	4.06	11	**4**	**3.74**	4.05	11	**4**	**3.37**	4.72	11	**4**	5.38	**4.04**	11	**6**
B→A	**4.15**	5.12	3	**1**	**4.70**	5.52	3	**1**	**5.03**	5.25	3	**1**	**5.15**	5.58	3	**1**	5.27	**5.21**	2	**1**
A→C	**2.99**	4.09	5	**2**	**3.29**	4.27	5	**2**	**3.49**	4.54	5	**2**	**3.50**	4.06	5	**2**	7.63	**3.82**	5	**2**
A→D	**2.80**	3.52	8	**3**	**2.55**	3.69	8	**4**	**3.42**	3.82	8	**4**	**2.75**	3.20	8	**4**	5.11	**3.36**	8	**4**
A→B	**4.14**	5.15	3	**1**	**4.62**	5.53	3	**1**	**5.00**	5.60	3	**1**	**5.08**	5.39	3	**1**	5.23	**5.15**	2	**1**

Values highlighted in bold show the best values comparing STD and MGA.

The average EVM and the number of handovers using STD and MGA strategies for Rx2 are described in Table 6.3. As expected, the MGA significantly reduced unnecessary handovers, achieving up to 75% fewer handovers (e.g., C→D at 1 m/s), while maintaining EVM values below the FEC limit. For speeds under 3 m/s, the STD produced lower EVMs due to its power-based triggering while increasing handovers. Again, at speeds exceeding 3m/s, STD triggered delayed handovers due to its static TTT parameter, leading to higher EVM values. In contrast, regardless of speed, the MGA maintained a stable EVMs. Figure 6.4 the results for C→A trajectory, where STD EVM rose from 2.80% to 9.39% while MGA remained consistent.

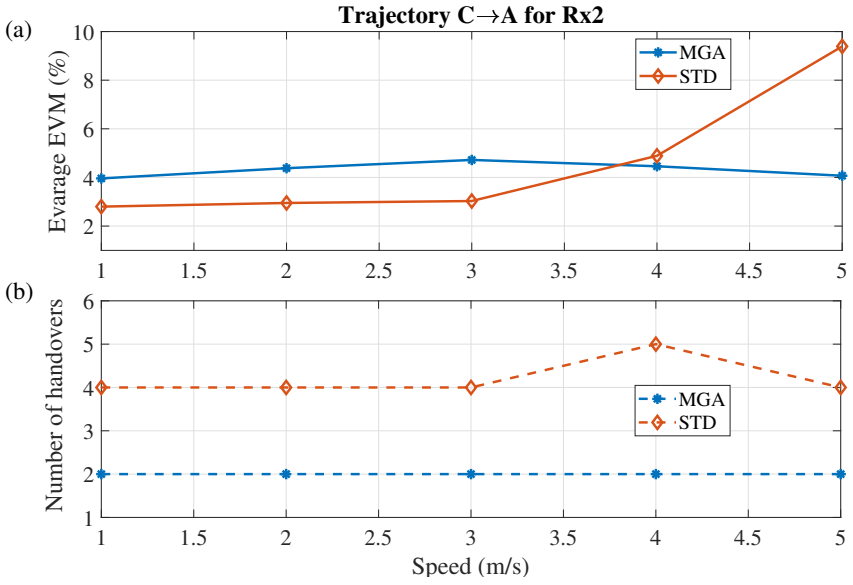

Figure 6.4. Rx2 MGA and STD handover results for trajectory C→A: (a) the average EVM and (b) the total number of handovers for each speed.

6.4.2. Model Optimization, Training, and Test

Table 6.4 presents the optimal hyperparameters obtained through Optuna optimization for the ML models. Figure 6.5 illustrates the training and validation accuracy achieved with the optimized hyperparameters of the LSTM-ANN. The convergence of these curves indicates ef-

fective training of the models without evidence of overfitting. Additionally, Table 6.5 presents the accuracy and loss metrics, highlighting the model's satisfactory scores.

Table 6.4. LSTM-ANN optimized Hyperparameters by Optuna

Model	Hyperparameter	Value
LSTM-ANN	Number of LSTM layers	6
	LSTM cells of each layer	512, 32, 16, 8, 32, 64
	Batch size	64
	Dropout	0.25
	Time-series input length	8
	Activation function	Tanh
	Optimizer	Adam
	Number of dense layers	5
	Neurons of each dense layer	512, 32, 128, 32, 8

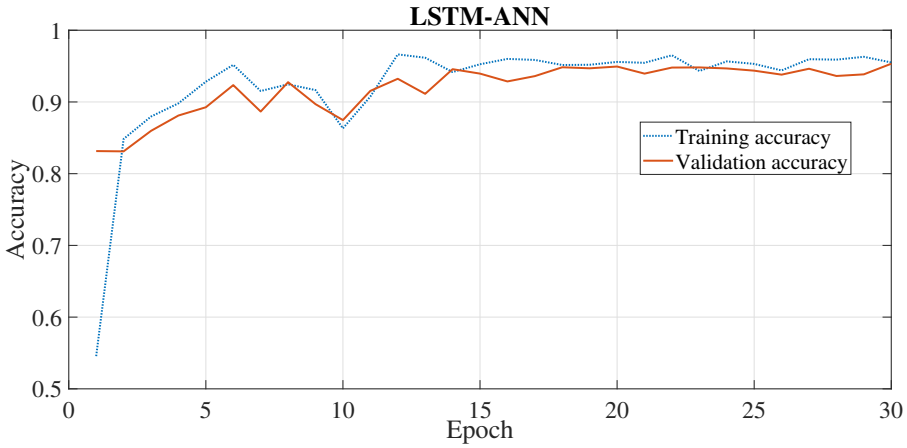

Figure 6.5. The accuracy obtained in the training and validation of the optimized LSTM-ANN model.

Table 6.5. Loss and accuracy results.

Model	Dataset	Loss	Accuracy
LSTM-ANN	Training	0.1979	0.9627
	Validation	0.2399	0.9467
	Test	0.2668	0.9321

The cumulative number of handovers across the test dataset for Rx1 and Rx2 is presented in Table 6.6. The STD achieved 85 and 72 handovers for Rx1 and Rx2, respectively. The LSTM-ANN demonstrated significant improvements, showing 47 and 37 handovers for Rx1 and Rx2, respectively. These results represent a reduction of 44.70% and 48.61% for Rx1 and Rx2. The average EVM across all cases demonstrated feasible performance, as the values remained below the FEC limit. However, the STD strategy exhibited significant variability, indicating values far from the average. To analyze this behavior, Figure 6.6 shows the CDF curves of the test dataset EVMs for both receivers, comparing the STD and LSTM-ANN + MGAD strategies. For both

receivers, the LSTM-ANN + MGAD strategy ensured that 100% of the EVMs were below approximately 10%, respecting the FEC limit. On the other hand, the STD strategy achieved 99.5% of EVM values below 9% for both receivers; however, it also reached outliers with EVM values of up to about 140%. This highlights that the system attempted to recover data from noise, particularly in regions outside the FOV.

Table 6.6. Handover results for the test dataset.

	Handovers		**Average EVM (%)**	
	Rx1	**Rx2**	**Rx1**	**Rx2**
STD	85	72	3.95 ± 9.28	4.13 ± 11.39
LSTM-ANN + MGAD	47	37	3.97 ± 1.97	4.15 ± 1.85

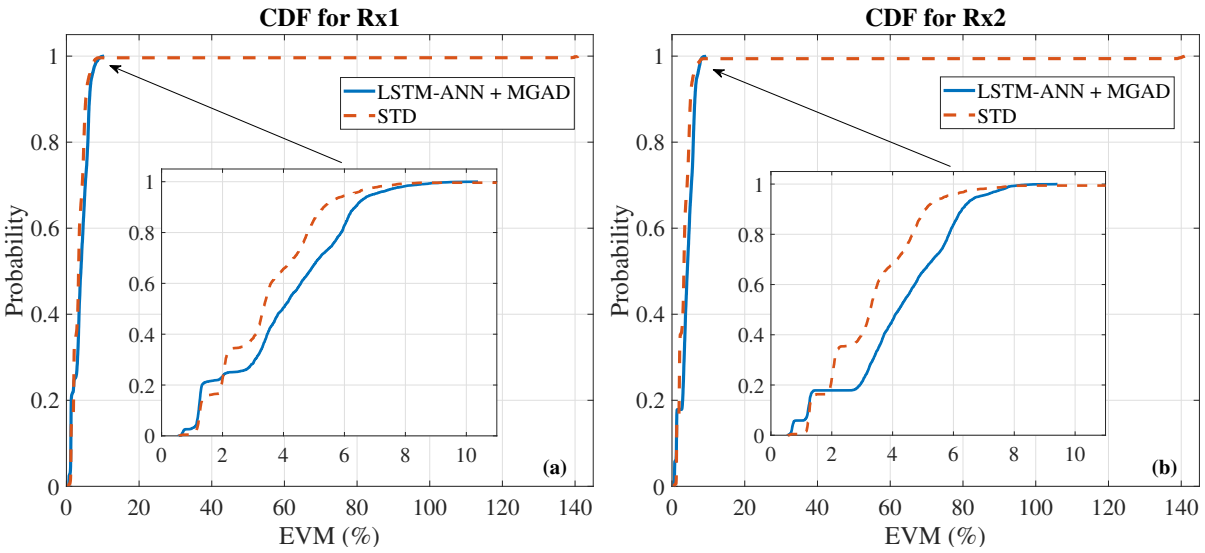

Figure 6.6. EVM CDF of the test dataset for (a) Rx1 and (b) Rx2

6.5. Conclusions

This Chapter proposed a real-time handover strategy using optimization and machine learning to minimize handovers of a MIMO VLC system with 18 access points and two receivers. This approach considers trajectory information to minimize the handovers by applying a modified genetic algorithm. Moreover, the LSTM-ANN model was implemented to predict the next destinations of both receivers simultaneously. Thereafter, the real-time VLC system combines the optimized handover data, predicted trajectories, and the receivers' current position to trigger handovers, ensuring efficient communication.

The total number of handovers across all tested trajectories was effectively decreased by the MGA optimization, achieving reductions of up to 75% compared to the power-based STD approach. As expected, the performance of the STD method was significantly affected by higher

receiver speeds. In contrast, the MGA-based strategy overcame this limitation by incorporating spatial references into its handover decision process. Furthermore, the LSTM-ANN strategy achieved handover reductions of 44.70% and 48.61% for Rx1 and Rx2, respectively, when compared to STD. In addition to minimizing handovers, the LSTM-ANN maintained all EVM values across the test dataset under 10% for both receivers, maintaining the performance below the FEC limit. This demonstrates its robust ability to minimize the number of handovers while maintaining satisfactory performance. In contrast, the STD approach presented high EVM values in certain parts of the test dataset, particularly in regions outside the FOV, where the system attempted to recover data from noise.

CHAPTER 7.
Conclusions and Future Directions

7.1. Final Remarks

In this thesis, we investigated the PAPR reduction technique based on constant-envelope OFDM signals to enhance VLC links. By employing CE-OFDM modulation, the system demonstrated tolerance to noises and nonlinearities introduced by LEDs and, as a consequence, provides power efficiency and transmission distance enlargements. The study investigated how the phase modulation index affects performance, revealing its dependency on the modulation levels of the subcarriers. A performance comparison between VLC systems with and without constant-envelope signals was conducted based on measured variations of the error vector magnitude. Experimental results indicated that the CE-OFDM based system outperformed the conventional OFDM, particularly under high bias current conditions where the LED operates in its nonlinear regime.

The signals with a PAPR of 3 dB provided power efficiency, resulting in consistent EVM improvements across nearly all evaluated link lengths. At short link lengths, where signal saturation is predominant at the receiver, EVM improved by 52.6% when applying CE-OFDM with 4-QAM as the modulation scheme. At longer distances, EVM improvements of about 54% and 43% were still observed with 4-QAM at 8 m and 16-QAM at 6 m, respectively, mainly due to the tolerance to nonlinearity assured by constant-envelope signals.

Additionally, this thesis evaluated the impact of bias current and communication signal amplitude on the performance of a SISO setup. Also, the accuracy of a VLC analytical model with SISO and MISO experimental setups was exploited. The results demonstrated that the bias current (I_{bias}) has minimal impact on system performance if the communication signal operates within the linear region and the receiver remains unsaturated. The amplitude of the communication signal (V_{pp}) affected saturation and drove it into a nonlinearity region. Meanwhile, higher amplitudes improve performance when the system operates unsaturated and in the linear region. Disregarding the height of 50 cm, the optimal EVM across the trajectory was achieved with $V_{\text{pp}} = 2000$ mV and a bias current of 100, 200, or 300 mA.

The results from the simulation model demonstrated satisfactory approximation with the real-world setup. The SISO simulation model achieved an RMSE of 0.22%, 0.36%, 1.09%, and 1.43% at heights of 100, 150, 200, and 250 cm, respectively, when compared to the experimental setup. For the MISO configuration at the height of 100 cm, RMSE values for Tx1 and Tx2

were higher at 37.63% and 34.09% due to partial trajectory loss outside the FOV due to the experimental setup limitations. The lowest MISO RMSE values occurred at 150 cm, with Tx1 and Tx2 errors of 1.37% and 1.65%, respectively. At distances of 200 cm and 250 cm, the RMSEs for Tx1 were 2.72% and 4.32%, while for Tx2 they were 3.24% and 5.09%, respectively. These results confirm the reliability of the simulation model, making it a robust tool for evaluating new algorithms, optimization strategies, modulation techniques, and for use in educational contexts.

Moreover, this thesis proposed a real-time handover scheme using optimization and machine learning to minimize the number of handovers of a digital twin-based VLC system. A modified genetic algorithm was proposed to optimize handovers using trajectory information. ML models were implemented to estimate the receiver's next destination. The real-time VLC system integrates the optimized handover data, predicted trajectory, and receiver's current position to trigger handovers, maintaining communication performance.

The MGA optimization significantly reduced the total number of handovers across all tested trajectories, achieving up to a 75% reduction compared to the power-based STD. While STD performance declined with higher receiver speeds, the MGA-based approach effectively addressed this issue by incorporating spatial references into handover decisions. Moreover, Decision Tree, LSTM-ANN, and TCN-ANN were applied to the real-time VLC system using the optimized handover data. For the error-free positioning test dataset, these models reduced handovers by 24.66%, 42.47%, and 31.51%, respectively, compared to STD. When positional errors were introduced, LSTM-ANN and TCN-ANN maintained robust performance, reducing handovers by 39.73% and 26.03%, while the Decision Tree model increased handovers by 75.34%, proving to be inadequate for such scenario. Experimental results highlighted that the LSTM-ANN combined with MGA data reduced handovers by 46.43% and 45.45% in MISO scenarios with three and four transmitters, respectively, by skipping unnecessary exchanges. Therefore, the LSTM-ANN with MGA demonstrated strong potential to minimize handovers and enhance system performance, even in the presence of positional inaccuracies.

The same LSTM-ANN with MGA approach was applied to a MIMO VLC system with 18 access points and two receivers. In this new scenario, the LSTM-ANN model was trained using data from both receivers simultaneously to predict their next destinations. For this MIMO scenario, the MGA optimization effectively reduced handovers across all tested trajectories by up to 75% compared to the STD method. Additionally, the LSTM-ANN + MGA strategy reduced handovers by 44.70% and 48.61% for Rx1 and Rx2, respectively. It maintained all the EVM values below 10% in the test data, demonstrating a robust approach. In contrast, the STD method showed high EVM values in certain parts of the test dataset where it tried to recover data from regions outside the FOV.

7.2. Hypotheses Discussions

H.1 - By setting CE-OFDM as the modulation scheme of a VLC system, it is possible to increase the reach of the communication link compared with conventional OFDM.

The constant-envelope property of CE-OFDM waveforms significantly reduces the PAPR, enabling more efficient operation of the LED within its nonlinear regime. The reduced PAPR minimizes signal clipping and distortion typically induced by LED nonlinearities, particularly under high bias current conditions. Furthermore, the low PAPR also helps to avoid saturating the receiver. Consequently, the CE-OFDM system achieves low EVM and enhanced signal fidelity over extended link distances. Experimental results demonstrated that CE-OFDM increased the VLC link distance by up to around 3 meters, considering the FEC limit. Therefore, we conclude that it is possible to increase the reach of the VLC links with CE-OFDM.

H.2 - The bias current does not impact system performance if it is set at a level that prevents the communication signal from driving the LED into a non-linear or cutoff region.

The bias current level defines the LED's operating point around which the communication signal is centered. As long as neither the bias current nor the signal amplitude drives the LED into its nonlinear, cutoff regions, or causes receiver saturation, variations in the bias current do not significantly affect the EVM performance of a VLC system. Experimental results validated this hypothesis by demonstrating consistent system performance across a range of bias currents, as long as the signal amplitude was appropriately constrained to avoid nonlinear behavior.

H.3 - Considering a MISO VLC system, AI models can predict the following endpoint of a receiver based on its trajectory and positioning to minimize handovers while maintaining EVM performance under the FEC limit.

By considering temporal and spatial features extracted from the receiver's movement, AI architectures such as LSTM-ANN and TCN-ANN can learn mobility patterns and forecast future positions with high accuracy. When integrated with an optimized handover strategy, such as MGA, these predictive models enable smart handover decisions, minimizing unnecessary handovers. Experimental results confirm that this approach significantly reduces handover occurrences while preserving EVM values below the FEC limit, even in the presence of positional errors, thereby ensuring reliable communication and enhanced link stability in indoor VLC environments.

H.4 - AI models can simultaneously predict the following endpoint of multiple receivers based on their trajectory and positioning, optimizing handover efficiency and ensuring EVM performances within the FEC threshold.

Sequence-based models such as LSTM-ANN are trained using joint trajectory datasets from multiple receivers to capture both individual movement patterns. When integrated with an optimization strategy like the MGA, the AI-driven prediction enables coordinated handover decisions that reduce unnecessary handovers. Experimental results demonstrate that this multi-receiver predictive framework significantly decreases the number of handovers while keeping EVM values below the FEC limit, confirming its effectiveness in supporting scalable and robust mobility management in VLC environments.

7.3. Recommendations for Future Research

The following topics describe the future directions for this thesis:

- develop parameters optimization such as optical and phase modulation indexes of CE-OFDM signals, LED bias current, and amplitude of the modulating signals using metaheuristic algorithms, aiming to improve power consumption, spectral efficiency, link reach, and handover;
- compare MGA handover optimization with conventional GA and other metaheuristics such as Particle Swarm Optimization, Differential Evolution, and Grey Wolf Optimizer.
- investigate new ML architectures and alternative models to deal with ambiguous datasets caused by overlapping trajectories;
- conduct experimental evaluations of the proposed handover scheme in a dense MISO scenario, replicating the conditions simulated in this thesis;
- implement a proof-of-concept for the proposed handover scheme in a MIMO VLC system;
- train ML models using the optimized handover data to enable direct prediction of the most suitable access point for the receiver to connect;
- investigate ML approaches to address access point failures and adapt to new trajectories.

References

[1] R. Schmogrow, B. Nebendahl, M. Winter, A. Josten, D. Hillerkuss, S. Koenig, J. Meyer, M. Dreschmann, M. Huebner, C. Koos *et al.*, "Error vector magnitude as a performance measure for advanced modulation formats," *IEEE Photonics Technology Letters*, vol. 24, no. 1, pp. 61–63, 2011. [Cited on pages xvi, 28, and 53]

[2] R. Amsters, D. Holm, J. Joly, E. Demeester, N. Stevens, and P. Slaets, "Visible light positioning using bayesian filters," *Journal of Lightwave Technology*, vol. 38, no. 21, pp. 5925–5936, 2020. [Cited on pages xvii, 61, and 62]

[3] K. Lee, S. Donnelly, and G. Phillips, "2020 us lighting market characterization," Guidehouse, Inc., Washington, DC (United States), Tech. Rep., 2024. [Cited on page 1]

[4] P. M. Research, "Led lighting market share, size, trends, industry analysis report, by product (led lamps, led fixtures); by application; by end-user; by region; segment forecast, 2024-2032," Polaris Market Research, Tech. Rep., 2024. [Cited on page 1]

[5] A. Mahmood, L. Beltramelli, S. Fakhrul Abedin, S. Zeb, N. I. Mowla, S. A. Hassan, E. Sisinni, and M. Gidlund, "Industrial iot in 5g-and-beyond networks: Vision, architecture, and design trends," *IEEE Transactions on Industrial Informatics*, vol. 18, no. 6, pp. 4122–4137, 2022. [Cited on page 1]

[6] W. Haerick and M. Gupta, "5G and the factories of the future," *5G-PPP White Paper*, 2015. [Cited on page 1]

[7] M. Jabbar and M. Rahman, "Radio frequency interference of electric motors and associated controls," *IEEE Transactions on Industry Applications*, vol. 27, no. 1, pp. 27–31, 1991. [Cited on page 1]

[8] L. Grobe, A. Paraskevopoulos, J. Hilt, D. Schulz, F. Lassak, F. Hartlieb, C. Kottke, V. Jungnickel, and K.-D. Langer, "High-speed visible light communication systems," *IEEE Communications Magazine*, vol. 51, no. 12, pp. 60–66, 2013. [Cited on page 1]

[9] H. Haas, L. Yin, C. Chen, S. Videv, D. Parol, E. Poves, H. Alshaer, and M. S. Islim, "Introduction to indoor networking concepts and challenges in lifi," *Journal of Optical Communications and Networking*, vol. 12, no. 2, pp. A190–A203, 2020. [Cited on page 1]

[10] A. Paraskevopoulos, J. Vučić, S. Voß, R. Swoboda, and K. Langer, "Optical wireless communication systems in the mb/s to gb/s range, suitable for industrial applications," *IEEE/ASME Transactions on Mechatronics*, vol. 15, no. 4, pp. 541–547, 2010. [Cited on

page 1]

[11] S. Rajagopal, R. D. Roberts, and S.-K. Lim, "Ieee 802.15. 7 visible light communication: modulation schemes and dimming support," *IEEE Communications Magazine*, vol. 50, no. 3, 2012. [Cited on page 1]

[12] C. Ribeiro Barbio Corrêa, K. A. Mekonnen, F. Huijskens, T. Koonen, and E. Tangdiongga, "Passive ofe multi-gbps vlc transmission using pof as a feeder line," *Microwave and Optical Technology Letters*, vol. n/a, no. n/a, 2022. [Cited on page 1]

[13] M. Serror, S. Hack, M. Henze, M. Schuba, and K. Wehrle, "Challenges and opportunities in securing the industrial internet of things," *IEEE Transactions on Industrial Informatics*, vol. 17, no. 5, pp. 2985–2996, 2021. [Cited on page 1]

[14] G. Blinowski, "Security of visible light communication systems—a survey," *Physical Communication*, vol. 34, pp. 246–260, 2019. [Cited on page 1]

[15] S. Aboagye, A. Ibrahim, T. M. N. Ngatched, and O. A. Dobre, "Vlc in future heterogeneous networks: Energy– and spectral–efficiency optimization," in *ICC 2020 - 2020 IEEE International Conference on Communications (ICC)*, 2020, pp. 1–7. [Cited on page 1]

[16] B. Lin, X. Tang, Z. Ghassemlooy, X. Fang, C. Lin, Y. Li, and S. Zhang, "Experimental demonstration of ofdm/oqam transmission for visible light communications," *IEEE Photonics Journal*, vol. 8, no. 5, pp. 1–10, 2016. [Cited on page 1]

[17] D. Schulz, V. Jungnickel, C. Alexakis, M. Schlosser, J. Hilt, A. Paraskevopoulos, L. Grobe, P. Farkas, and R. Freund, "Robust optical wireless link for the backhaul and fronthaul of small radio cells," *Journal of Lightwave Technology*, vol. 34, no. 6, pp. 1523–1532, 2016. [Cited on page 1]

[18] G. Cossu, W. Ali, R. Corsini, and E. Ciaramella, "Gigabit-class optical wireless communication system at indoor distances (1.5 – 4 m)," *Opt. Express*, vol. 23, no. 12, pp. 15 700–15 705, 2015. [Cited on page 1]

[19] F. T. Monteiro, W. S. Costa, J. L. Neves, D. M. Silva, H. R. Rocha, E. O. Salles, and J. A. Silva, "Experimental evaluation of pulse shaping based 5g multicarrier modulation formats in visible light communication systems," *Optics Communications*, vol. 457, p. 124693, 2020. [Cited on pages 1 and 34]

[20] W.-W. Hu, "Papr reduction in dco-ofdm visible light communication systems using optimized odd and even sequences combination," *IEEE Photonics Journal*, vol. 11, no. 1, pp. 1–15, 2019. [Cited on page 1]

[21] H. Elgala, R. Mesleh, and H. Haas, "A study of led nonlinearity effects on optical wireless transmission using ofdm," in *2009 IFIP International Conference on Wireless and Optical Communications Networks*, 2009, pp. 1–5. [Cited on page 1]

[22] Z. Yu, R. J. Baxley, and G. T. Zhou, "Iterative clipping for papr reduction in visible light ofdm communications," in *2014 IEEE Military Communications Conference*, 2014, pp. 1681–1686. [Cited on pages 1, 27, 28, and 29]

[23] W. Hu and D. Lee, "Papr reduction for visible light communication systems without side information," *IEEE Photonics Journal*, vol. 9, no. 3, pp. 1–11, 2017. [Cited on pages 1 and 27]

[24] Z. Li and C. Zhang, "An improved fd-dfe structure for downlink vlc systems based on sc-fdma," *IEEE Communications Letters*, vol. 22, no. 4, pp. 736–739, 2018. [Cited on pages 1 and 27]

[25] J. A. L. Silva, A. V. T. Cartaxo, and M. E. V. Segatto, "A papr reduction technique based on a constant envelope ofdm approach for fiber nonlinearity mitigation in optical direct-detection systems," *IEEE/OSA Journal of Optical Communications and Networking*, vol. 4, no. 4, pp. 296–303, April 2012. [Cited on pages 2, 18, 27, and 30]

[26] H. R. de O. Rocha, V. O. C. Dias, E. d. V. Pereira, R. B. Nunes, M. E. V. Segatto, and J. A. L. Silva, "Increasing the spectral efficiency of ddo-ce-ofdm systems by multi-objective optimization," *Journal of Lightwave Technology*, vol. 37, no. 9, pp. 2155–2162, 2019. [Cited on pages 2, 27, 30, and 33]

[27] R. B. Nunes, H. R. de O. Rocha, M. E. Segatto, and J. A. Silva, "Experimental validation of a constant-envelope ofdm system for optical direct-detection," *Optical Fiber Technology*, vol. 20, no. 3, pp. 303 – 307, 2014. [Cited on pages 2, 27, and 33]

[28] A. Vavoulas, H. G. Sandalidis, T. A. Tsiftsis, and N. Vaiopoulos, "Coverage aspects of indoor vlc networks," *Journal of Lightwave Technology*, vol. 33, no. 23, pp. 4915–4921, 2015. [Cited on page 2]

[29] M. S. Demir, F. Miramirkhani, and M. Uysal, "Handover in vlc networks with coordinated multipoint transmission," in *2017 IEEE International Black Sea Conference on Communications and Networking (BlackSeaCom)*, 2017, pp. 1–5. [Cited on page 2]

[30] X. Wu and H. Haas, "Handover skipping for lifi," *IEEE Access*, vol. 7, pp. 38 369–38 378, 2019. [Cited on pages 2 and 57]

[31] E. A. Jarchlo, E. Eso, H. Doroud, A. Zubow, F. Dressler, Z. Ghassemlooy, B. Siessegger, and G. Caire, "Fdla: A novel frequency diversity and link aggregation solution for handover in an indoor vehicular vlc network," *IEEE Transactions on Network and Service Management*, vol. 18, no. 3, pp. 3556–3566, 2021. [Cited on page 2]

[32] M. W. Eltokhey, M. A. Khalighi, Z. Ghassemlooy, and V. Jungnickel, "Handover-aware scheduling for small-and large-scale vlc networks," *IEEE Transactions on Network and Service Management*, pp. 1–1, 2023. [Cited on page 2]

[33] H. A. F. Camporez, W. S. Costa, J. A. L. Silva, H. R. O. Rocha, and M. E. V. Segatto,

"Performance evaluation of a soft handover framework applied to vlc systems," in *2021 SBMO/IEEE MTT-S International Microwave and Optoelectronics Conference (IMOC)*, 2021, pp. 1–3. [Cited on pages 2 and 39]

[34] F. Wang, Z. Wang, C. Qian, L. Dai, and Z. Yang, "Efficient vertical handover scheme for heterogeneous vlc-rf systems," *J. Opt. Commun. Netw.*, vol. 7, no. 12, pp. 1172–1180, Dec 2015. [Cited on page 2]

[35] Q. Hu, C. Gan, X. Liu, G. Gong, and Y. Zhu, "Dynamic handover cost modeling in hybrid vlc/rf networks," *Ad Hoc Networks*, vol. 146, p. 103174, 2023. [Cited on page 2]

[36] E. Alizadeh Jarchlo, E. Eso, H. Doroud, B. Siessegger, Z. Ghassemlooy, G. Caire, and F. Dressler, "Li-wi: An upper layer hybrid vlc-wifi network handover solution," *Ad Hoc Networks*, vol. 124, p. 102705, 2022. [Cited on page 2]

[37] J. Shi, W. Niu, Y. Ha, Z. Xu, Z. Li, S. Yu, and N. Chi, "Ai-enabled intelligent visible light communications: Challenges, progress, and future," *Photonics*, vol. 9, no. 8, 2022. [Cited on page 2]

[38] R. S. Peres, X. Jia, J. Lee, K. Sun, A. W. Colombo, and J. Barata, "Industrial artificial intelligence in industry 4.0 - systematic review, challenges and outlook," *IEEE Access*, vol. 8, pp. 220 121–220 139, 2020. [Cited on page 2]

[39] D. Cote, "Using machine learning in communication networks [invited]," *Journal of Optical Communications and Networking*, vol. 10, no. 10, pp. D100–D109, 2018. [Cited on page 2]

[40] E. d. V. Pereira, H. R. d. O. Rocha, R. B. Nunes, M. E. V. Segatto, and J. A. L. Silva, "Impact of optical power in the guard-band reduction of an optimized ddo-ofdm system," *Journal of Lightwave Technology*, vol. 33, no. 23, pp. 4717–4725, 2015. [Cited on page 2]

[41] W. Costa, H. Camporez, M. Pontes, M. Segatto, H. Rocha, J. Silva, M. Hinrichs, A. Paraskevopoulos, V. Jungnickel, and R. Freund, "Increasing the power and spectral efficiencies of an ofdm-based vlc system through multi-objective optimization," *J. Opt. Soc. Am. A*, vol. 40, no. 6, pp. 1268–1275, Jun 2023. [Cited on page 2]

[42] B. Lin, Q. Lai, Z. Ghassemlooy, and X. Tang, "A machine learning based signal demodulator in noma-vlc," *Journal of Lightwave Technology*, vol. 39, no. 10, pp. 3081–3087, 2021. [Cited on page 2]

[43] W. S. Costa, J. L. Samatelo, H. R. Rocha, M. E. Segatto, and J. A. Silva, "Direct equalization with convolutional neural networks in ofdm based vlc systems," in *2019 IEEE Latin-American Conference on Communications (LATINCOM)*, 2019, pp. 1–6. [Cited on page 3]

[44] W. Costa, H. Camporez, M. Segatto, H. Rocha, and J. Silva, "Towards ai-enhanced vlc

systems," in *Optical Fiber Communication Conference (OFC) 2022*. Optica Publishing Group, 2022, p. W3I.7. [Cited on pages 3, 28, 29, 39, 51, 52, and 56]

[45] W. Costa, H. Camporez, M. Hinrichs, H. Rocha, M. Pontes, M. Segatto, A. Paraskevopoulos, V. Jungnickel, R. Freund, and J. Silva, "Toward ai-enhanced vlc systems for industrial applications," *Journal of Lightwave Technology*, vol. 41, no. 4, pp. 1064–1076, 2023. [Cited on pages 3, 9, 51, 52, 53, and 63]

[46] Z. Ghassemlooy, L. Alves, S. Zvanovec, and M. Khalighi, *Visible Light Communications: Theory and Applications*. CRC-Taylor & Francis Group, 2017. [Cited on pages 9 and 30]

[47] A. G. Bell, W. Adams, null Tyndall, and W. Preece, "Discussion on "the photophone and the conversion of radiant energy into sound"," *Journal of the Society of Telegraph Engineers*, vol. 9, pp. 375–383, 1880. [Cited on page 9]

[48] I.-C. Lu, C.-H. Yeh, D.-Z. Hsu, and C.-W. Chow, "Utilization of 1-ghz vcsel for 11.1-gbps ofdm vlc wireless communication," *IEEE Photonics Journal*, vol. 8, no. 3, pp. 1–6, 2016. [Cited on page 9]

[49] J. Hu, F. Hu, J. Jia, G. Li, J. Shi, J. Zhang, Z. Li, N. Chi, S. Yu, and C. Shen, "46.4 gbps visible light communication system utilizing a compact tricolor laser transmitter," *Opt. Express*, vol. 30, no. 3, pp. 4365–4373, Jan 2022. [Cited on page 9]

[50] H. A. Camporez, Y. S. Pimassoni, W. S. Costa, M. E. Segatto, J. A. Silva, and H. R. Rocha, "Remote control in smartphone-based visible light communications," in *2021 Third South American Colloquium on Visible Light Communications (SACVLC)*, 2021, pp. 01–06. [Cited on page 9]

[51] Y. H. Kim, W. A. Cahyadi, and Y. H. Chung, "Experimental demonstration of vlc-based vehicle-to-vehicle communications under fog conditions," *IEEE Photonics Journal*, vol. 7, no. 6, pp. 1–9, 2015. [Cited on page 9]

[52] M. Meucci, M. Seminara, T. Nawaz, S. Caputo, L. Mucchi, and J. Catani, "Bidirectional vehicle-to-vehicle communication system based on vlc: Outdoor tests and performance analysis," *IEEE Transactions on Intelligent Transportation Systems*, vol. 23, no. 8, pp. 11 465–11 475, 2022. [Cited on page 9]

[53] K. M. V. D. Zwaag, M. P. Marinho, W. D. S. Costa, F. De Assis Souza Dos Santos, T. F. Bastos-Filho, H. R. O. Rocha, M. E. V. Segatto, and J. A. L. Silva, "A manchester-ook visible light communication system for patient monitoring in intensive care units," *IEEE Access*, vol. 9, pp. 104 217–104 226, 2021. [Cited on page 9]

[54] B. Donmez, R. Mitra, and F. Miramirkhani, "Channel modeling and characterization for vlc-based medical body sensor networks: Trends and challenges," *IEEE Access*, vol. 9, pp. 153 401–153 419, 2021. [Cited on page 9]

[55] V. Jungnickel, P. W. Berenguer, S. M. Mana, M. Hinrichs, S. M. Kouhini, K. L. Bober, and C. Kottke, "Lifi for industrial wireless applications," in *2020 Optical Fiber Communications Conference and Exhibition (OFC)*, 2020, pp. 1–3. [Cited on page 9]

[56] J. P. M. G. Linnartz, C. R. B. Corrêa, T. E. B. Cunha, E. Tangdiongga, T. Koonen, X. Deng, M. Wendt, A. A. Abbo, P. J. Stobbelaar, P. Polak, M. Müller, D. Behnke, M. Martínez, S. Vicent, T. Metin, M. Emmelmann, S. M. Kouhini, K. L. Bober, C. Kottke, and V. Jungnickel, "Eliot: enhancing lifi for next-generation internet of things," *EURASIP Journal on Wireless Communications and Networking*, vol. 2022, no. 1, p. 89, Sep 2022. [Online]. Available: https://doi.org/10.1186/s13638-022-02168-6 [Cited on page 9]

[57] V. N. Saxena, J. Gupta, and V. K. Dwivedi, "Secured end-to-end fso-vlc-based iot network with randomly positioned vlc: Known and unknown csi," *IEEE Internet of Things Journal*, vol. 10, no. 2, pp. 1347–1357, 2023. [Cited on page 9]

[58] S. Kumar and N. Sharma, "Emerging military applications of free space optical communication technology: A detailed review," *Journal of Physics: Conference Series*, vol. 2161, no. 1, p. 012011, jan 2022. [Online]. Available: https://dx.doi.org/10.1088/1742-6596/2161/1/012011 [Cited on page 9]

[59] S. Ucar, S. Coleri Ergen, O. Ozkasap, D. Tsonev, and H. Burchardt, "Secvlc: Secure visible light communication for military vehicular networks," in *Proceedings of the 14th ACM International Symposium on Mobility Management and Wireless Access*, ser. MobiWac '16. New York, NY, USA: Association for Computing Machinery, 2016, p. 123–129. [Online]. Available: https://doi.org/10.1145/2989250.2989259 [Cited on page 9]

[60] M. F. Ali, D. N. K. Jayakody, and Y. Li, "Recent trends in underwater visible light communication (uvlc) systems," *IEEE Access*, vol. 10, pp. 22 169–22 225, 2022. [Cited on page 9]

[61] M. F. Ali, D. N. K. Jayakody, S. Garg, G. Kaddoum, and M. S. Hossain, "Dual-hop mixed fso-vlc underwater wireless communication link," *IEEE Transactions on Network and Service Management*, vol. 19, no. 3, pp. 3105–3120, 2022. [Cited on page 9]

[62] Z. Wang, Q. Wang, W. Huang, and Z. Xu, *Visible light communications: modulation and signal processing*. John Wiley & Sons, 2017. [Cited on pages 10 and 12]

[63] P. A. Hoeher, *Visible light communications: theoretical and practical foundations*. Carl Hanser Verlag GmbH Co KG, 2019. [Cited on page 10]

[64] H. Elgala, R. Mesleh, and H. Haas, "An led model for intensity-modulated optical communication systems," *IEEE Photonics Technology Letters*, vol. 22, no. 11, pp. 835–837, 2010. [Cited on page 10]

[65] L. N. Binh, *Optical fiber communication systems with MATLAB and Simulink*

models, 2nd ed., ser. Optics and photonics. CRC Press, 2015. [Online]. Available: https://cir.nii.ac.jp/crid/1130000795413113088 [Cited on page 10]

[66] E. F. Schubert, *Light-Emitting Diodes*, 2nd ed. Cambridge University Press, 2006. [Cited on page 11]

[67] G. Z. P. W. R. Sujan, *Optical wireless communications: system and channel modelling with Matlab*. CRC press, 2019. [Cited on page 11]

[68] T. Komine, S. Haruyama, and M. Nakagawa, "A study of shadowing on indoor visible-light wireless communication utilizing plural white LED lightings," *Wireless Personal Communications*, vol. 34, no. 1, pp. 211–225, 2005. [Cited on page 12]

[69] P. Lou, H. Zhang, X. Zhang, M. Yao, and Z. Xu, "Fundamental analysis for indoor visible light positioning system," in *2012 1st IEEE International Conference on Communications in China Workshops (ICCC)*, 2012, pp. 59–63. [Cited on page 12]

[70] M. L. Doelz, E. T. Heald, and D. L. Martin, "Binary data transmission techniques for linear systems," *Proceedings of the IRE*, vol. 45, no. 5, pp. 656–661, 1957. [Cited on page 12]

[71] R. W. Chang, "Synthesis of band-limited orthogonal signals for multichannel data transmission," *Bell System Technical Journal*, vol. 45, no. 10, pp. 1775–1796, 1966. [Cited on page 12]

[72] B. Saltzberg, "Performance of an efficient parallel data transmission system," *IEEE Transactions on Communication Technology*, vol. 15, no. 6, pp. 805–811, 1967. [Cited on page 12]

[73] S. Weinstein and P. Ebert, "Data transmission by frequency-division multiplexing using the discrete fourier transform," *IEEE Transactions on Communication Technology*, vol. 19, no. 5, pp. 628–634, 1971. [Cited on page 12]

[74] A. Peled and A. Ruiz, "Frequency domain data transmission using reduced computational complexity algorithms," in *ICASSP '80. IEEE International Conference on Acoustics, Speech, and Signal Processing*, vol. 5, 1980, pp. 964–967. [Cited on page 12]

[75] B. Hirosaki, "An analysis of automatic equalizers for orthogonally multiplexed qam systems," *IEEE Transactions on Communications*, vol. 28, no. 1, pp. 73–83, 1980. [Cited on page 12]

[76] ——, "An orthogonally multiplexed qam system using the discrete fourier transform," *IEEE Transactions on Communications*, vol. 29, no. 7, pp. 982–989, 1981. [Cited on page 12]

[77] T. Komine, S. Haruyama, and M. Nakagawa, "Performance evaluation of narrowband ofdm on integrated system of power line communication and visible light wireless communication," in *2006 1st International Symposium on Wireless Pervasive Computing*,

2006, pp. 6 pp.–6. [Cited on page 12]

[78] S. Ahmadi, *An Overview of 3GPP Long-Term Evolution Radio Access Network*. Boston, MA: Springer US, 2009, pp. 431–465. [Cited on page 12]

[79] A. A. Zaidi, R. Baldemair, V. Moles-Cases, N. He, K. Werner, and A. Cedergren, "Ofdm numerology design for 5g new radio to support iot, embb, and mbsfn," *IEEE Communications Standards Magazine*, vol. 2, no. 2, pp. 78–83, 2018. [Cited on page 12]

[80] K. Jia and L. Hao, "Modeling of multipath channel and performance analysis of mimo-dco-ofdm system in visible light communications," *Chinese Journal of Electronics*, vol. 28, no. 3, pp. 630–639, 2019. [Cited on page 12]

[81] Y. G. Li and G. L. Stuber, *Orthogonal frequency division multiplexing for wireless communications*. Springer Science & Business Media, 2006. [Cited on page 12]

[82] J. A. L. Silva, "Transmissão de sinais ofdm com envelope constante em sistemas ópticos imdd," PhD thesis, Universidade Federal do Espírito Santo, Vitória, ES, August 2011. [Cited on pages 13 and 15]

[83] E. L. Pinto and C. P. de Albuquerque, "A técnica de transmissão ofdm," *Revista Científica*, vol. 1516, p. 2338, 2002. [Cited on page 13]

[84] J. Proakis and M. Salehi, *Digital Communications*, 5th ed. Boston: McGraw-Hill, 2007. [Cited on page 14]

[85] H. Rohling, *OFDM: concepts for future communication systems*. Springer Science & Business Media, 2011. [Cited on page 16]

[86] V. Kishore, V. S. Prasad, and V. V. Mani, "A blind timing synchronization algorithm for dco-ofdm vlc systems," *IEEE Photonics Technology Letters*, vol. 32, no. 17, pp. 1121–1124, 2020. [Cited on page 17]

[87] H. T. Alrakah, T. Z. Gutema, S. Sinanovic, and W. O. Popoola, "Papr reduction in dco-ofdm based wdm vlc," *Journal of Lightwave Technology*, vol. 40, no. 19, pp. 6359–6365, 2022. [Cited on page 17]

[88] S. Ma, R. Yang, X. Deng, X. Ling, X. Zhang, F. Zhou, S. Li, and D. W. Kwan Ng, "Spectral and energy efficiency of aco-ofdm in visible light communication systems," *IEEE Transactions on Wireless Communications*, vol. 21, no. 4, pp. 2147–2161, 2022. [Cited on page 17]

[89] N. Fernando, Y. Hong, and E. Viterbo, "Flip-ofdm for unipolar communication systems," *IEEE Transactions on Communications*, vol. 60, no. 12, pp. 3726–3733, 2012. [Cited on page 17]

[90] F. Yang, Y. Sun, and J. Gao, "Adaptive laco-ofdm with variable layer for visible light communication," *IEEE Photonics Journal*, vol. 9, no. 6, pp. 1–8, 2017. [Cited on page 17]

[91] S. C. Thompson, A. U. Ahmed, J. G. Proakis, J. R. Zeidler, and M. J. Geile, "Constant envelope ofdm," *IEEE Transactions on Communications*, vol. 56, no. 8, pp. 1300–1312, August 2008. [Cited on pages 17, 19, 30, and 33]

[92] W. Costa, H. Camporez, M. Pontes, M. Segatto, H. Rocha, J. Silva, M. Hinrichs, A. Paraskevopoulos, V. Jungnickel, and R. Freund, "Increasing the led bias point of an OFDM-based vlc system through multi-objective optimization," in *2021 SBMO/IEEE MTT-S International Microwave and Optoelectronics Conference (IMOC)*. IEEE, 2021, pp. 1–3. [Cited on page 17]

[93] K. M. vd Zwaag, J. L. C. Neves, H. R. O. Rocha, M. E. V. Segatto, and J. A. L. Silva, "Increasing vlc nonlinearity tolerance by ce-ofdm," in *Latin America Optics and Photonics Conference*. Optica Publishing Group, 2018, p. W3D.3. [Cited on pages 17 and 34]

[94] R. B. Nunes, H. R. de O Rocha, D. A. A. Mello, F. D. Simões, M. E. V. Segatto, and J. A. L. Silva, "Transmission of ce-ofdm signals over mmf links using directly modulated 850-nm vcsels," *IEEE Photonics Technology Letters*, vol. 27, no. 3, pp. 315–318, Feb 2015. [Cited on page 17]

[95] B. Lathi, *Modern digital and analog communication systems*. Oxford university press, 2010. [Cited on page 18]

[96] R. A. Shafik, M. S. Rahman, A. R. Islam, and N. S. Ashraf, "On the error vector magnitude as a performance metric and comparative analysis," in *2006 International Conference on Emerging Technologies*, 2006, pp. 27–31. [Cited on page 18]

[97] Z. Yu, R. J. Baxley, and G. T. Zhou, "Evm and achievable data rate analysis of clipped ofdm signals in visible light communication," *EURASIP Journal on Wireless Communications and Networking*, vol. 2012, no. 1, p. 321, Oct 2012. [Cited on page 18]

[98] F. Sandoval, G. Poitau, and F. Gagnon, "Hybrid peak-to-average power ratio reduction techniques: Review and performance comparison," *IEEE Access*, vol. 5, pp. 27 145–27 161, 2017. [Cited on page 19]

[99] S. Thompson, J. Proakis, and J. Zeidler, "The effectiveness of signal clipping for papr and total degradation reduction in ofdm systems," in *GLOBECOM '05. IEEE Global Telecommunications Conference, 2005.*, vol. 5, 2005, pp. 5 pp.–2811. [Cited on page 19]

[100] C. Santos, V. Oliari, H. Rocha, M. Pontes, M. Segatto, C. Okonkwo, A. Alvarado, and J. Silva, "Experimental demonstration of constant-envelope ofdm to reduce intermodulation impairments and increase robustness against fiber nonlinearities," *Journal of Lightwave Technology*, vol. 40, no. 15, pp. 4983–4989, 2022. [Cited on page 19]

[101] J. H. Holland, "Genetic algorithms," *Scientific American*, vol. 267, no. 1, pp. 66–73, 1992. [Cited on page 19]

[102] S. Katoch, S. S. Chauhan, and V. Kumar, "A review on genetic algorithm: past, present,

and future," *Multimedia Tools and Applications*, vol. 80, no. 5, pp. 8091–8126, Feb 2021. [Cited on page 19]

[103] M. Gendreau, J.-Y. Potvin *et al.*, *Handbook of metaheuristics*. Springer, 2010, vol. 2. [Cited on page 19]

[104] Y.-Y. Song and Y. Lu, "Decision tree methods: applications for classification and prediction," *Shanghai Arch Psychiatry*, vol. 27, no. 2, pp. 130–135, Apr. 2015. [Cited on page 20]

[105] S. Shalev-Shwartz and S. Ben-David, *Decision Trees*. Cambridge University Press, 2014, p. 212–218. [Cited on page 20]

[106] S. Haykin, *Neural Networks: A Comprehensive Foundation 2Nd Ed.* Prentice-Hall Of India Pvt. Limited, 1999. [Cited on pages 21 and 23]

[107] A. D. Rasamoelina, F. Adjailia, and P. Sinčák, "A review of activation function for artificial neural network," in *2020 IEEE 18th World Symposium on Applied Machine Intelligence and Informatics (SAMI)*, 2020, pp. 281–286. [Cited on page 22]

[108] X. Liang, X. Wang, Z. Lei, S. Liao, and S. Z. Li, "Soft-margin softmax for deep classification," in *Neural Information Processing*, D. Liu, S. Xie, Y. Li, D. Zhao, and E.-S. M. El-Alfy, Eds. Cham: Springer International Publishing, 2017, pp. 413–421. [Cited on page 22]

[109] F. Rosenblatt, "The perceptron: A probabilistic model for information storage and organization in the brain." US, pp. 386–408, 1958. [Cited on page 23]

[110] N. Srivastava, G. Hinton, A. Krizhevsky, I. Sutskever, and R. Salakhutdinov, "Dropout: A simple way to prevent neural networks from overfitting," *Journal of Machine Learning Research*, vol. 15, no. 56, pp. 1929–1958, 2014. [Online]. Available: http://jmlr.org/papers/v15/srivastava14a.html [Cited on page 23]

[111] D. Mahajan, R. Girshick, V. Ramanathan, K. He, M. Paluri, Y. Li, A. Bharambe, and L. van der Maaten, "Exploring the limits of weakly supervised pretraining," in *Proceedings of the European Conference on Computer Vision (ECCV)*, September 2018. [Cited on page 24]

[112] S. M. Al-Selwi, M. F. Hassan, S. J. Abdulkadir, A. Muneer, E. H. Sumiea, A. Alqushaibi, and M. G. Ragab, "Rnn-lstm: From applications to modeling techniques and beyond—systematic review," *Journal of King Saud University - Computer and Information Sciences*, vol. 36, no. 5, p. 102068, 2024. [Cited on page 24]

[113] S. Hochreiter and J. Schmidhuber, "Long short-term memory," *Neural Comput.*, vol. 9, no. 8, p. 1735–1780, nov 1997. [Cited on page 24]

[114] P. Lara-Benítez, M. Carranza-García, and J. C. Riquelme, "An experimental review on deep learning architectures for time series forecasting," *International Journal of Neural*

Systems, vol. 31, no. 03, p. 2130001, 2021. [Cited on page 24]

[115] N. Kalchbrenner, E. Grefenstette, and P. Blunsom, "A convolutional neural network for modelling sentences," *CoRR*, vol. abs/1404.2188, 2014. [Cited on page 25]

[116] C. Lea, R. Vidal, A. Reiter, and G. D. Hager, "Temporal convolutional networks: A unified approach to action segmentation," in *Computer Vision – ECCV 2016 Workshops*, G. Hua and H. Jégou, Eds. Cham: Springer International Publishing, 2016, pp. 47–54. [Cited on page 25]

[117] S. Bai, J. Z. Kolter, and V. Koltun, "An empirical evaluation of generic convolutional and recurrent networks for sequence modeling," *CoRR*, vol. abs/1803.01271, 2018. [Cited on page 25]

[118] T. Akiba, S. Sano, T. Yanase, T. Ohta, and M. Koyama, "Optuna: A next-generation hyperparameter optimization framework," in *Proceedings of the 25th ACM SIGKDD International Conference on Knowledge Discovery and Data Mining*, 2019. [Cited on page 26]

[119] J. A. L. Silva, T. Alves, A. Cartaxo, and M. E. V. Segatto, "Experimental demonstration of a direct-detection constant envelope ofdm system," in *Advanced Photonics & Renewable Energy*. Optica Publishing Group, 2010, p. SPThB2. [Cited on page 27]

[120] E. Xie, R. Bian, X. He, M. S. Islim, C. Chen, J. J. D. McKendry, E. Gu, H. Haas, and M. D. Dawson, "Over 10 gbps vlc for long-distance applications using a gan-based series-biased micro-led array," *IEEE Photonics Technology Letters*, vol. 32, no. 9, pp. 499–502, 2020. [Cited on pages 28 and 29]

[121] X. Liu, P. Tian, Z. Wei, S. Yi, Y. Huang, X. Zhou, Z.-J. Qiu, L. Hu, Z. Fang, C. Cong, L. Zheng, and R. Liu, "Gbps long-distance real-time visible light communications using a high-bandwidth gan-based micro-led," *IEEE Photonics Journal*, vol. 9, no. 6, pp. 1–9, 2017. [Cited on pages 28 and 29]

[122] B. Fahs, A. J. Chowdhury, and M. M. Hella, "A 12-m 2.5-gb/s lighting compatible integrated receiver for ook visible light communication links," *Journal of Lightwave Technology*, vol. 34, no. 16, pp. 3768–3775, 2016. [Cited on pages 28 and 29]

[123] R. Bian, I. Tavakkolnia, and H. Haas, "15.73 gb/s visible light communication with off-the-shelf leds," *Journal of Lightwave Technology*, vol. 37, no. 10, pp. 2418–2424, 2019. [Cited on pages 28 and 29]

[124] K. Werfli, P. Chvojka, Z. Ghassemlooy, N. B. Hassan, S. Zvanovec, A. Burton, P. A. Haigh, and M. R. Bhatnagar, "Experimental demonstration of high-speed 4 × 4 imaging multi-cap mimo visible light communications," *Journal of Lightwave Technology*, vol. 36, no. 10, pp. 1944–1951, 2018. [Cited on pages 28 and 29]

[125] D.-H. Chen, Y.-J. Cheng, Y.-W. Chen, J.-H. Yan, and K.-M. Feng, "Phosphor-based led

visible light communication system bandwidth enhancement employing mc-cdma," in *2017 Optical Fiber Communications Conference and Exhibition (OFC)*, 2017, pp. 1–3. [Cited on pages 28 and 29]

[126] T. zhang, Z. Ghassemlooy, C. Ma, and S. Guo, "Papr reduction scheme for aco-ofdm based visible light communication systems," *Optics Communications*, vol. 383, pp. 75–80, 2017. [Cited on pages 28 and 29]

[127] J. Zhang, C. Guo, L. Liu, S. He, and X. Hong, "Demonstration of a visible light communication system based on filter bank spread ofdm/oqam," in *2017 Asia Communications and Photonics Conference (ACP)*, 2017, pp. 1–3. [Cited on pages 28 and 29]

[128] M. Shi, F. Wang, M. Zhang, Z. Wang, and N. Chi, "Papr reduction of 2.0gbit/s dft-s ofdm modulated visible light communication system based on interleaved sub-banding technique," in *2017 IEEE International Conference on Communications Workshops (ICC Workshops)*, 2017, pp. 337–342. [Cited on pages 28 and 29]

[129] S. P. Valluri, V. Kishore, and V. M. Vakamulla, "A new selective mapping scheme for visible light systems," *IEEE Access*, vol. 8, pp. 18 087–18 096, 2020. [Cited on pages 28 and 29]

[130] H. Lu, Y. Hong, L.-K. Chen, and J. Wang, "Experimental investigation on impacts of papr reduction schemes in ofdm-based vlc systems," in *2017 Opto-Electronics and Communications Conference (OECC) and Photonics Global Conference (PGC)*, 2017, pp. 1–3. [Cited on pages 28 and 29]

[131] A. U. Ahmed and J. R. Zeidler, "Novel low-complexity receivers for constant envelope ofdm," *IEEE Transactions on Signal Processing*, vol. 63, no. 17, pp. 4572–4582, 2015. [Cited on page 30]

[132] K. M. vd Zwaag, J. L. Neves, H. R. Rocha, M. E. Segatto, and J. A. Silva, "Adaptation to the leds flicker requirement in visible light communication systems through ce-ofdm signals," *Optics Communications*, vol. 441, pp. 14 – 20, 2019. [Cited on page 30]

[133] J. Andrews, A. Ghosh, and R. Muhamed, *Fundamentals of WiMAX: Understanding Broadband Wireless Networking*. USA: Prentice Hall Press, 2011. [Cited on page 31]

[134] *DS061 LUXEON Rebel ES Product Datasheet*, Lumileds, Apr. 2016, rev. 3. [Online]. Available: http://www.lumileds.com/uploads/17/DS61-pdf [Cited on page 34]

[135] A. C. F. Peterle, W. Costa, H. Camporez, M. Segatto, H. Rocha, and J. A. L. Silva, "Comparing the performance of ofdm and ocdm-based visible light communications: Numerical and experimental analysis," *Journal of Microwaves, Optoelectronics and Electromagnetic Applications*, vol. 22, no. 1, p. 196–207, Mar 2023. [Online]. Available: https://doi.org/10.1590/2179-10742023v22i1270869 [Cited on page 39]

[136] P. Sharda, G. S. Reddy, M. R. Bhatnagar, and Z. Ghassemlooy, "A comprehensive mod-

eling of vehicle-to-vehicle based vlc system under practical considerations, an investigation of performance, and diversity property," *IEEE Transactions on Communications*, vol. 70, no. 5, pp. 3320–3332, 2022. [Cited on page 39]

[137] W. Costa, H. Camporez, M. Pontes, M. Segatto, H. Rocha, J. Silva, M. H. nrichs, A. Paraskevopoulos, V. Jungnickel, and R. Freund, "Increasing the power and spectral efficiencies of an ofdm-based vlc system through multi-objective optimization," *J. Opt. Soc. Am. A*, vol. 40, no. 6, pp. 1268–1275, Jun 2023. [Cited on page 39]

[138] C. He and W. Ali, "Advances in visible light communication," *Photonics*, vol. 10, no. 11, 2023. [Online]. Available: https://www.mdpi.com/2304-6732/10/11/1277 [Cited on page 39]

[139] M. Kottkamp, A. Pandey, D. Raddino, A. Roessler, R. Stuhlfauth, and R. und Schwarz, *5G New Radio: Fundamentals, Procedures, Testing Aspects*. Rohde & Schwarz GmbH & Company KG, 2019. [Cited on pages 39 and 52]

[140] H. Technologies. Lifi receiver. Accessed: 2024-05-21. [Online]. Available: https://www.hyperiontechs.com/product/lifi-receiver [Cited on pages 40 and 53]

[141] Z.-Y. Wu, M. Ismail, E. Serpedin, and J. Wang, "Data-driven link assignment with qos guarantee in mobile rf-optical hetnet of things," *IEEE Internet of Things Journal*, vol. 7, no. 6, pp. 5088–5102, 2020. [Cited on page 51]

[142] L. Wang, D. Han, M. Zhang, D. Wang, and Z. Zhang, "Deep reinforcement learning-based adaptive handover mechanism for vlc in a hybrid 6g network architecture," *IEEE Access*, vol. 9, pp. 87 241–87 250, 2021. [Cited on page 51]

[143] D. Frometa Fonseca, B. Genoves Guzman, G. Luca Martena, R. Bian, H. Haas, and D. Giustiniano, "Prediction-model-assisted reinforcement learning algorithm for handover decision-making in hybrid lifi and wifi networks," *Journal of Optical Communications and Networking*, vol. 16, no. 2, pp. 159–170, 2024. [Cited on page 51]

[144] X. Wu and D. C. O'Brien, "A novel machine learning-based handover scheme for hybrid lifi and wifi networks," in *2020 IEEE Globecom Workshops (GC Wkshps*, 2020, pp. 1–5. [Cited on page 51]

[145] G. Ma, R. Parthiban, and N. Karmakar, "An artificial neural network-based handover scheme for hybrid lifi networks," *IEEE Access*, vol. 10, pp. 130 350–130 358, 2022. [Cited on page 51]

[146] F. Tao, H. Zhang, A. Liu, and A. Y. C. Nee, "Digital twin in industry: State-of-the-art," *IEEE Transactions on Industrial Informatics*, vol. 15, no. 4, pp. 2405–2415, 2019. [Cited on page 52]

[147] L. Wright and S. Davidson, "How to tell the difference between a model and a digital twin," *Advanced Modeling and Simulation in Engineering Sciences*, vol. 7, no. 1, pp.

1–13, 2020. [Cited on page 52]

[148] 3GPP, "LTE; Evolved universal terrestrial radio access (E-UTRA); Radio resource control (RCC); Protocol specification (Release 13)," 3GPP, Technical Specification (TS) 36.331, 2016, version 13.0.0. [Cited on page 56]

[149] M. Kowsher, A. Tahabilder, M. Z. Islam Sanjid, N. J. Prottasha, M. S. Uddin, M. A. Hossain, and M. A. Kader Jilani, "Lstm-ann & bilstm-ann: Hybrid deep learning models for enhanced classification accuracy," *Procedia Computer Science*, vol. 193, pp. 131–140, 2021, 10th International Young Scientists Conference in Computational Science, YSC2021, 28 June – 2 July, 2021. [Cited on page 64]

[150] H. Camporez, W. Costa, M. Segatto, J. Silva, J. K. Deters, H. Wörtche, and H. Rocha, "Ai-driven enhancements for handover in visible light communication systems," *Journal of Lightwave Technology*, pp. 1–12, 2024. [Cited on page 64]

[151] M. A. S. Sejan, M. H. Rahman, M. A. Aziz, D.-S. Kim, Y.-H. You, and H.-K. Song, "A comprehensive survey on mimo visible light communication: Current research, machine learning and future trends," *Sensors*, vol. 23, no. 2, 2023. [Cited on page 79]

[152] F. Dong and D. O'Brien, "High-speed adaptive mimo-vlc system with neural network," *Journal of Lightwave Technology*, vol. 40, no. 16, pp. 5530–5540, 2022. [Cited on page 79]

[153] M.-L. Zhang and Z.-H. Zhou, "A review on multi-label learning algorithms," *IEEE Transactions on Knowledge and Data Engineering*, vol. 26, no. 8, pp. 1819–1837, 2014. [Cited on page 82]